MODELLING AND SIMULATION OF INDUCTION MOTORS FOR VARIABLE SPEED DRIVES, WITH SPECIAL REFERENCE TO DEEP BAR AND SATURATION EFFECTS.

Warren Levy

A thesis submitted to the Faculty of Engineering, University of the Witwatersrand, Johannesburg, in fulfillment of the requirements for the Degree of Doctor of Philosophy.

Johannesburg, 1990.

DECLARATION

I declare that this thesis is my own unaided work. It is being submitted for the Degree of Doctor of Philosophy to the University of the Witwatersrand, Johannesburg. It has not been submitted before for any degree or examination in any other University.

W. Levy
31/7/1990

FOREWORD

Variable speed motors are achieved by varying the voltage of a DC machine or by varying the frequency of an AC machine, the former method being the simpler of the two. DC motors have the major disadvantage of brushes and commutators which require regular downtime for maintenance, a fact already recognised by Tesla [1] in 1888. Thus the AC motor, in particular the induction motor, is of a more rugged design and does not suffer from the commutator problem of its DC counterpart. Recent advances in the technology of the power electronics used to supply a variable frequency to the motor has allowed the induction motor to be a viable alternative to the DC motor in variable speed applications.

Problems have been encountered in industry when an inverter is injudiciously selected to be combined with a motor. Such problems were highlighted by difficulties being experienced with some 400 kW inverter drives. The inverters had been bought from one supplier and the motors from another. When this system was coupled together, there was excessive heating in the motors and the overall plant was only able to operate well below its capacity, incurring a substantial weekly loss of income. The motor and inverter were evidently incompatible, and since the inverter could not be modified, the motor was redesigned to make it less susceptible to the harmonics present in the inverter waveform.

These problems have led to the development of a variable speed drive simulation package at the University for use by the local industry which can accurately model the complete system of inverter, motor and its associated load. It is envisaged that this package could be used to predict the performance of a drive system and highlight problems that may occur. To be able to do this, an accurate model of the motor is required.

This investigation gives the development of an induction motor model which is suitable for variable speed drive system simulations. The model accounts for the deep bar effect by using lumped parameter circuits and includes saturation of the leakage paths using only information which is typically available from motor design data. A complete analysis is given of the different lumped parameter models and their suitability for use in this application. The thesis also shows the utilisation of the deep bar model to simulate reswitching transients and double cage motors. The author hopes that the models used in the simulation package will allow industry to predict problems prior to their occurrence, alter the designs and thereby avoid costly remanufacture of the system.

I would like to acknowledge the following people and/or groups for their support during this project. The list is given in no specific order because I feel equally indebted to everyone.

- The National Energy Council of South Africa for the required funding of this project.
- Professor C. Landy of the Department of Electrical Engineering, University of the Witwatersrand, Johannesburg, for his foresight in realising that the work had potential. He has always been available for advice and has readily given encouragement, for which I am extremely grateful.

- Malcolm McCulloch, my co-researcher on this project, for all the assistance and suggestions he has given during the project. Malcolm, it has really been a pleasure working with you.

- GEC Machines of South Africa, for their willingness to provide design data of various machines used for verification of this project.

- My parents, who have always given support and encouragement when I needed it most, and who have been understanding and patient during the period of writing this thesis.

LIST OF SYMBOLS

A = area

B = flux density (T)

C_s = number of stator conductors per slot

D_{is} = stator inside diameter (mm)

d = depth (mm)

F = coefficient of friction

$\mathcal{F}$ = magneto-motive force (mmf)

$[G]$ = rotational inductance matrix

H = mmf per m

I = current (A)

$[I]$ = vector of two-axis currents

J = rotational moment of inertia

K_d = stator winding distribution factor

K_p = stator coil pitch factor

L = self inductance (H)

L_l = leakage inductance (H)

$[L]$ = inductance matrix

l = length (mm)

M = mutual inductance (H)

N = number of turns

N_1 = number of stator turns in series per phase

P_c = number of stator parallel circuits

PU = per unit

$\mathcal{P}$ = permeance

p = number of pole pairs
q = number of phases
R = resistance (Ω)
$[R]$ = resistance matrix
RMS = root mean square
S = number of slots
$\mathcal{T}$ = torque (Nm)
t = time (seconds)
V = voltage (V)
$[V]$ = vector of two-axis voltages
w = width (mm)

Superscripts

$'$ = rotor value referred to stator
T = matrix transposition

Subscripts

a, b, c = three phase winding subscripts
b = bar
blk = block
c = core
d = d-axis
e = end-ring, electrical
i = inner bar
l = leakage, load
m = mechanical

o = outer bar

q = q-axis

r = rotor

s = stator, saturable, synchronous

sat = saturable portion

sec = section

t = tooth tip

u = unsaturable portion

0 = refers to leakage above bar

$0, 1..n$ = refers to the number of any specific section of bar

Greek Letters

α, β = axes which three phase a,b,c system is passively transformed to

γ = zero sequence axis

θ = angle between stator and rotor axis

λ = permeance coefficient per unit length

μ_0 = magnetic space constant

ρ = resistivity

σ = saturation factor

τ = time constant

Φ = flux

Ψ = flux linkage

ω = rotational speed

Table of Contents

FOREWORD i

LIST OF SYMBOLS iv

CHAPTER 1 : INTRODUCTION 1

CHAPTER 2 : BACKGROUND INFORMATION 5
  2.1. Induction Motor Differential Equations 5
  2.2. Electromagnetic Torque 9
  2.3. The Simulation Program 10

CHAPTER 3 : DEEP BAR MODEL 12
  3.1. The Need For An Accurate Deep Bar Model 12
  3.2. Previous Models 14
  3.3. Equivalent Circuit For Rectangular Rotor Bar 17
  3.4. Other Lumped Parameter Circuits 22
  3.5. Accuracy Of Equivalent Circuit 29
  3.6. Algorithm To Improve The Accuracy Of Models 36
  3.7. Implementation Of Different Bar Shapes 41
  3.8. Model Verification 46
    3.8.1. Sinusoidal input waveform 46
    3.8.2. Inverter input 51

CHAPTER 4 : DOUBLE CAGE MOTOR 56
  4.1. Traditional Model 56
  4.2. New Deep Bar Double Cage Model 59
    4.2.1. Method And Implementation 59
    4.2.2. Example 61

CHAPTER 5 : SATURATION 66
  5.1. Work Done By Other Researchers 66
  5.2. Methods Implemented In CASED 68
    5.2.1. The Empirical Method 69
    5.2.2. The Current Ratio Method 71
  5.3. Case Study 74

CHAPTER 6 : RESWITCHING TRANSIENTS 80
  6.1. Reswitching Using The Traditional Model 80
  6.2. Reswitching Using The Deep Bar Model 82
  6.3. Example 83

CHAPTER 7 : CONCLUSIONS 91

APPENDIX A 95

APPENDIX B 109

APPENDIX C 113

APPENDIX D 124
APPENDIX E 146
REFERENCES 153
EXTRA REFERENCES 158

CHAPTER 1

INTRODUCTION

The large increase in the industrial usage of induction motors for variable speed drives (VSD) has seen an associated increase in the problems encountered with these systems. These problems often arise because the motor has not been specifically designed for the inverter drive, but has simply been connected to an inverter with similar ratings. Typical problems encountered are instability of the system due to mechanical/electrical resonance and excessive heating of the motor due to additional harmonics present in the motor from the inverter supply, which can dramatically shorten the life span of the motor.

The non-sinusoidal waveform of the inverter introduces harmonics into the currents in the stator and rotor of the motor ([10], [11], [22]). Thus, in the rotor bars, high frequency components of current exist which flow in the upper portions of the bar. This phenomenon is known as the skin, or deep bar, effect and effectively increases the resistance of the bars. Also, under transient conditions, the currents in the motor are larger than rated value and saturation of the leakage paths will occur ([26], [33], [36]). Both these situations can have a profound effect on the performance of the system and need to be considered when examining a VSD system.

To try to avoid incompatibility problems associated with inverter drives, a method is required to predict the system performance <u>prior</u> to manufacture of the system. The most efficient method of prediction is computer simulation, which requires an accurate model of each component of the system. An induction motor model which accounts for deep bar and saturation effects is thus required which can link its input/output to the converter model of McCulloch et al [37]. The standard d-q axis motor model, as given by O'Kelly and Simmons [12], has some inherent assumptions which make it unsuitable for VSD system simulations. Firstly the rotor parameters used in the model are fixed and secondly the model assumes a linear characteristic, thus neither frequency nor saturation effects are accounted for.

The analytical solution of the deep bar equation as proposed by Liwschitz-Garik [5] and Alger [14] is the most accurate solution. It suffers from the following drawbacks when applied to VSD simulations :

1) Many frequencies exist in the current waveform and each separately contributes to the total skin effect.

2) Knowledge of the frequency content of the non-sinusoidal waveform is not readily available.

Mahmoud and Menzies [30] and Boldea and Nasar [32] suggest using fictitious coils in the rotor to simulate the deep bar effect, one coil for starting and one for running conditions. The parameters of these additional coils are obtained from frequency tests of the motor. This method has similar problems to those listed above, because many different frequencies exist in the motor and the model would thus require far too many coils. Bruges [2] first proposed a ladder-type network to model the rotor, and Babb and Williams [3 and 4] showed how a lumped parameter model could be used to calculate the impedance of a rotor bar. Babb and Williams [4] also suggest alternate lumped parameter models which can be used. This thesis analyses the accuracy of the different lumped parameter models and compares their performance under various frequency conditions. A novel algorithm is introduced which increases the accuracy of the model by up to thirty times at certain frequencies.

Articles on accounting for saturation effects of either the magnetising or the leakage flux paths abound in the literature. The research has been directed towards the effects in synchronous motors ([23], [27], [31]) and the problem has also been addressed for induction motors ([7], [13], [21], [25], [26], [28], [36]). Most articles use the same method of accounting for saturation - split the inductance into a saturable and an unsaturable portion and alter the saturable portion according to the motor's measured voltage-flux characteristic. This method would require tests to be performed on the motor and is thus unsuitable for the present application. Two alternative methods have been used - the first is an empirical correction factor and the second is based on the current at which the leakage paths will saturate (Agarwal and Alger [7]).

The aim of this work has been to develop an accurate induction motor model which is suitable to be used in conjunction with an inverter model. The motor model should be able to account for any frequency variations of the rotor parameters caused by harmonics from the inverter. Saturation of the leakage flux paths should also be included. The input parameters of the model must be obtained from design data so that no tests need be performed on the motor to simulate the system. This thesis details the development of a motor model which accounts for both the deep bar effect and saturation present in the motor. The correlation between the predicted curves using this model and the measured results indicate that the objective has been realised.

The motor models have been implemented in a variable-speed drive (VSD) simulation package which consists of three main programs as shown in Chapter 2. The author's main contribution to the package has been the development of the "CREATE" program which reads in the necessary data for the VSD system and saves the data in files which have a format suitable for the "SIM" program to use. The source code listings for the "CREATE" program would comprise a volume of more than 100 pages and have therefore not been included.

Chapter 2 gives background information of the d-q axis model and its implementation. Chapter 3 gives the development of the new deep bar model, followed by a Chapter showing that this deep bar model may be extended to model double cage motors. Chapter 5 gives the methods used to include saturation of the leakage paths in the tooth tips and the last Chapter shows how the deep bar model can be applied to reswitching transients.

CHAPTER 2

BACKGROUND INFORMATION

This chapter gives a review of the d-q axis theory of machines, showing the derivation of the differential equations of a three phase induction motor in any arbitrary reference frame. The transformations that are applied to the three phase equations to reduce them to the d-q axis equivalent will be given. The equation for the electromagnetic torque and a brief description of the implementation of the motor equations in the simulation program will also be given.

2.1. Induction Motor Differential Equations

For simulation of an induction motor on a digital computer, the three phase differential equations describing the performance of the motor are transformed to a corresponding set of two axis equations. These transformations simplify the equations by making the machine inductances independent of the angle between the axes of the stator and rotor windings, i.e. independent of time.

The following assumptions are made in deriving the two-axis equations :

1) Magnetic saturation of the leakage flux paths has been ignored; this assumption will be discussed in a later Chapter where a means of accounting for saturation effects is shown.

2) The magneto-motive force (mmf) produced by the distributed winding is sinusoidal.

3) Eddy current and hysteresis losses are negligible and have thus been ignored.

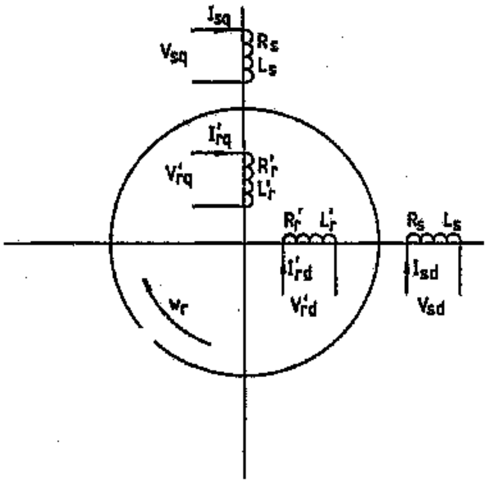

Figure 2.1 : d-q axis Representation Of Induction Motor

Appendix A gives the derivation of the stator and rotor equations transformed to the two phase d-q axis which rotates at an arbitrary speed, shown in Figure 2.1. The final form of these equations has made use of the following two facts :

1) The rotor winding (squirrel cage) is short-circuited and thus $V'_{rd} = V'_{rq} = 0$

2) The systems under consideration are balanced three phase, three wire systems and thus the zero sequence components are non-existent (i.e. $V_{s\gamma} = V'_{r\gamma} = I_{s\gamma} = I'_{r\gamma} = 0$)

Then, as given in equation (A.41), the induction motor equations are

$$\begin{bmatrix} V_{sd} \\ V_{sq} \\ 0 \\ 0 \end{bmatrix} = \begin{bmatrix} R_s + L_s \frac{d}{dt} & -\omega L_s & M\frac{d}{dt} & -\omega M \\ \omega L_s & R_s + L_s \frac{d}{dt} & \omega M & M\frac{d}{dt} \\ M\frac{d}{dt} & -(\omega-\omega_r)M & R'_r + L'_r \frac{d}{dt} & -(\omega-\omega_r)L'_r \\ (\omega-\omega_r)M & M\frac{d}{dt} & (\omega-\omega_r)L'_r & R'_r + L'_r \frac{d}{dt} \end{bmatrix} \begin{bmatrix} I_{sd} \\ I_{sq} \\ I'_{rd} \\ I'_{rq} \end{bmatrix} \tag{2.1}$$

where ω can have the following values :

1) $\omega = 0$: here the rotational terms in the stator equations fall away, the rotational terms in the rotor equations consist of ω_r only, and thus the system represents the motor equations in a stationary stator-fixed frame of reference.

2) $\omega = \omega_r$: the rotational terms in the rotor fall away and this system has its reference frame attached to the rotating rotor.

3) $\omega = \omega_s t$: ω_s is the frequency of the supply and thus this system has its frame of reference rotating at synchronous speed.

4) $\omega = \omega_a$: ω_a is any arbitrary rotational speed at which the frame of reference can rotate, relative to the rotor.

For simulation of the traditional fourth order differential equation of the motor as given by equation (2.1), the stator-fixed reference frame is the simplest, quickest and most efficient system to use. The derivation of the deep bar model given in Chapter 3 has used the rotor-fixed reference frame to avoid including rotational terms in the complex rotor equations.

Equation (2.1) can be rewritten in the form

$$[V] = [R]\cdot[I] + [L]\frac{d}{dt}[I] + [G]\cdot[I] \tag{2.2}$$

where

$$[V] = \begin{bmatrix} V_{sd} \\ V_{sq} \\ 0 \\ 0 \end{bmatrix} \tag{2.3}$$

$$[I] = \begin{bmatrix} I_{sd} \\ I_{sq} \\ I'_{rd} \\ I'_{rq} \end{bmatrix} \tag{2.4}$$

$$[R] = \begin{bmatrix} R_s & 0 & 0 & 0 \\ 0 & R_s & 0 & 0 \\ 0 & 0 & R'_r & 0 \\ 0 & 0 & 0 & R'_r \end{bmatrix} \tag{2.5}$$

$$[L] = \begin{bmatrix} L_s & 0 & M & 0 \\ 0 & L_s & 0 & M \\ M & 0 & L'_r & 0 \\ 0 & M & 0 & L'_r \end{bmatrix} \tag{2.6}$$

$$[G]=\begin{bmatrix} 0 & -\omega L_s & 0 & -\omega M \\ \omega L_s & 0 & \omega M & 0 \\ 0 & -(\omega-\omega_r)M & 0 & -(\omega-\omega_r)L'_r \\ (\omega-\omega_r)M & 0 & (\omega-\omega_r)L'_r & 0 \end{bmatrix} \tag{2.7}$$

2.2. Electromagnetic Torque

The electromagnetic torque of the induction motor is given by :

$$\mathcal{T}_e = p\ (\Psi'_{rq} I'_{rd} - \Psi'_{rd} I'_{rq}) \tag{2.8}$$

where Ψ'_{rq} and Ψ'_{rd} are given by equations (A.36). Substituting for the flux linkages gives

$$\begin{aligned} \mathcal{T}_e &= p\ (L'_r I'_{rd} I'_{rq} + M I_{sq} I'_{rd} - L'_r I'_{rd} I'_{rq} - M I_{sd} I'_{rq}) \\ &= p\ M (I_{sq} I'_{rd} - I_{sd} I'_{rq}) \end{aligned} \tag{2.9}$$

and the torque equation of the motor with its load is

$$\mathcal{T}_e - \mathcal{T}_l = F_m \omega_r + J_m \frac{d}{dt} \omega_r \tag{2.10}$$

where F_m is the coefficient of friction of the motor, J_m is the rotational moment of inertia of the motor plus load and $\mathcal{T}_l$ is the load torque.

2.3. The Simulation Program

The computer package CASED (Computer Analysis and Simulation of Electric Drives) is a modular program for the simulation of motors and variable speed drive systems (see McCulloch et al [40]). The package is composed of :

1) "CREATE" arranges the system to be simulated and reads in all the required data. Firstly the timing functions of the system simulation are entered i.e. frequency to save information to disk, time to change models, end time etc. Then the parameters of each individual component making up the system are read in, the state space model is generated and saved to files for the simulation program to use.

2) "SIM" is the main simulation program of CASED and has the flow diagram shown in Figure 2.2. The initialisation routine reads in the system files from "CREATE" and control of the program is then passed to the equation solver/event scheduler part of the program. The event scheduler is called up whenever an event occurs and needs to be processed (such as outputting to screen, logging to disk, changing sub-models and ending the simulation). The differential equation solver consecutively solves the state equations of each component of the system. The "state events" block is that portion of the program which changes the inverter model being used.

   For the model of the motor, as given by equation (2.2) to be used in this program, the state-space model is re-arranged to be of the form

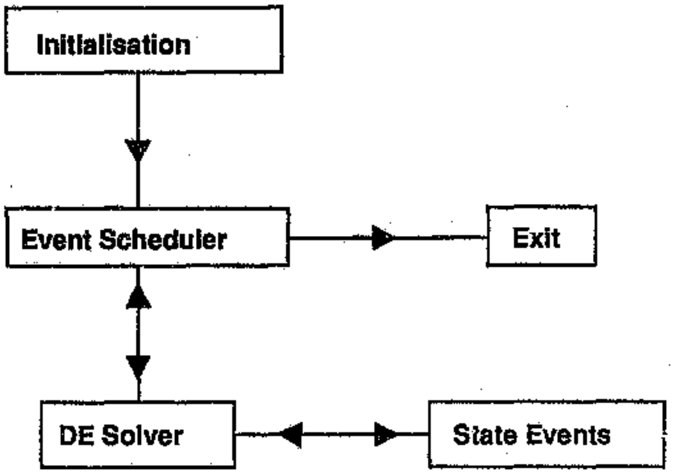

Figure 2.2 : **Simplified Flow Diagram Of The Simulation Program**

$$\frac{d}{dt}[I] = [L]^{-1}\{[V] - [R].[I] - [G].[I]\} \tag{2.11}$$

where [*V*] is the input to the motor model from the supply and [*I*] is the output of the motor model fed back to the supply. Both [*V*] and [*I*] here are two phase (d-q) quantities, whereas the inverter or sinusoidal supply work with three phase quantities. Thus $V_{a,b,c}$ are transformed to $V_{d,q}$, then the matrix of differential equations (2.11) is solved to give I_{sd}, I_{sq} which in turn are transformed back to $I_{a,b,c}$ and made available to the system.

3) "GRAPH" reads in the data file of saved information from "SIM" and allows various options for graphing the data.

CHAPTER 3

DEEP BAR MODEL

In this Chapter, the necessity for having a motor model which accurately accounts for deep bar effects is discussed. The work carried out in this field by other researchers is then reviewed. The new deep bar model is detailed and a comprehensive comparison of the accuracies is given. An algorithm is outlined to improve the accuracy at higher frequencies and two case studies are discussed to highlight the effectiveness of the model.

3.1. The Need For An Accurate Deep Bar Model

In an induction motor, the lower portions of the bars of the rotor cage are linked by more slot leakage flux than the upper portions of the bar. This can be seen in Figure 3.1, which shows a rectangular bar in a slot, with a higher density of lines representing leakage flux at the bottom of the slot. Under transient conditions, the inductance of the lower part of the bar is higher than that for the upper portion of the bar (caused by the non-uniform flux distribution) causing the current to flow primarily in the upper portion of the bar. The re-distribution of the current flowing in the bar effectively increases the resistance of the bar. This phenomenon of increased resistance and decreased inductance is known as the deep bar effect or skin effect. The effect is dominant in motors with rotor bars that have a large bar depth to bar width ratio (Alger [14]) and in motors where high frequency currents (> 50 Hz) flow in the bars.

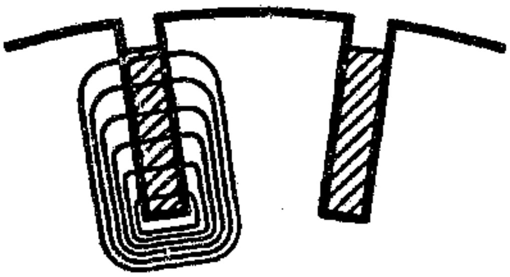

Figure 3.1 : Typical Leakage Flux Pattern In The Rectangular Slot Of A Rotor

Typically currents with a frequency ranging from nearly DC to 2500 Hz could be present in the rotor of the motor. If the motor is supplied from a sinusoidal source, the current would have a frequency equal to that of the supply (50 Hz) at starting and equal to the slip frequency (0.25 Hz for a 0.5 % slip) at running speed. For an inverter supply, the fundamental current could have a frequency from 100 Hz to less than 1 Hz. The inverter can also introduce time harmonics with frequencies up to or even greater than 2500 Hz (this frequency represents the 25th harmonic of a 100 Hz waveform). Therefore, whether a motor with deep bars is supplied from a sinusoidal source or an inverter supply is present, skin effect will be present and needs to be accounted for.

The model of the motor, as given by equation (2.2) does not take account of deep bar effects because the rotor values R'_r and L'_r are not dependent on the frequency of the currents flowing in the rotor. By not taking account of the rotor parameter variation with frequency, the predicted transient torque and currents will be incorrect, as shown in the first case study. Therefore a dynamic model is required in which the values R'_r and L'_r are continuously adjusted as the rotor frequency changes, thereby allowing better predictions of rotor current and developed torque.

3.2. Previous Models

Many articles have appeared in the literature on the simulation of induction motors fed from sinusoidal and non-sinusoidal waveforms ([9], [15], [29], [34], [35]). The researchers that have addressed the problem of modelling the deep bar effect will be discussed below.

Mahmoud and Menzies [30] have used the equivalence between a deep bar and a double cage rotor to account for the deep bar effects. Instead of having one d-axis and one q-axis winding to represent the rotor, they have used two windings on each axis. The resistances and inductances of the two rotor windings are obtained from measurements performed on the motor. This model is acceptable for sinusoidal waveforms where effectively one winding represents the rotor at start-up and the other winding represents the rotor at full speed. Under non-sinusoidal conditions, where harmonics introduce currents at higher frequencies than 50 Hz, this model will introduce inaccuracies. Also, this model is unsuitable to predict the performance of the motor prior to manufacture because tests need to be performed to obtain parameters of the model.

The model of Boldea and Nasar [32] uses two or three "fictitious short circuited windings" on each orthogonal axis, to represent the rotor. The parameters for these windings are determined from a range of frequency tests performed on the motor. The use of three circuits for the rotor improves the accuracy of Mahmoud and Menzies' [30] model under non-sinusoidal conditions but still has the drawbacks outlined in the previous paragraph.

Mukherjee et al [38] have modelled the induction motor using the three phase equations for the stator. The rotor is modelled as a phase for every slot per pole pair, where each phase has a differential equation associated with it. Finite element techniques are used to obtain all the required inductances as a function of θ, the rotor position relative to the stator. At each integration step, depending on the value of θ, the inductance matrix is generated and inverted, a computationally expensive procedure. Skin effect in the rotor bars is accounted for by using the integro-differential approach of Konrad [19 and 20], which is a finite element solution of Maxwell's equations.

An analytical solution of the deep bar equations, giving the ratios of AC to DC resistance and inductance, is proposed by Liwschitz-Garik [5] and [6]. The first paper gives the derivation of these ratios, in terms of hyperbolic sines and cosines, which at the time were awkward to calculate on a slide-rule. The second paper defines a "depth of penetration" as a function of the AC to DC ratios to avoid having to calculate the hyperbolic values. Alger [14] gives a similar derivation to Liwschitz-Garik [5] for a rectangular bar and states that different equations are needed for each different bar shape. For the rectangular bar, Alger gives a correction factor to be made to the DC resistance and inductance in terms of the frequency present in the bar. Although this analytical solution is obviously very precise, it could not be used in the present application for the following reasons :

- There are different deep bar differential equations for each bar shape, which is impractical for the generality required for CASED.

- This method only corrects the DC values of resistance and inductance for <u>one</u> particular frequency at a time. Under non-sinusoidal conditions when harmonics are present, more than one frequency exists in the rotor and it is difficult to determine what these frequencies are.

Therefore this method has not been used in the simulation, but it has been used for comparative purposes to analyse the accuracy of the lumped parameter circuit.

Bruges [2] was the first to show that a ladder network (or lumped parameter circuit) of resistances and inductances could be used as an equivalent circuit of a conductor in a slot of highly permeable material. In the 1950's, Babb and Williams published two articles on using the lumped parameter circuit to measure the impedance of a conductor in a slot at any frequency. The first, [3], describes the measurement of the resistance and the inductance of a rectangular bar, a T-bar and a slot containing one active and one idle bar. This paper concludes that the AC impedance of any shape of bar can be similarly calculated, and in the authors' reply to the discussion they mention that dividing the bar into unequal sections gives improved accuracy. In the second paper, [4], they suggest a new circuit to represent the sections of the bar which is more accurate than previous circuits. Klingshirn and Jordan [16] showed the possibility of using an analog simulation of an induction motor with deep rotor bars. They used the T configuration to approximate each section of the bar because this resulted in fewer meshes in the equivalent circuit. The work outlined by Babb and Williams in [3] and [4] forms the basis for the present investigation because this method accounts for any frequency being present and is suitable for any shape of bar.

3.3. Equivalent Circuit For Rectangular Rotor Bar

Appendix B shows the derivation of the resistance and leakage inductance of a rectangular bar in an open slot. The inductance is made up of two permeance contributions, one for the slot area above the bar (λ_0) and one for the bar itself (λ_b). The permeance coefficient of the bar is obtained by calculating the flux in an elemental slice of the bar and then integrating this flux over the depth of the bar. The resistance and leakage inductance so calculated is then used in the equivalent circuit of Figure 3.2 as R'_r and L'_{lr} respectively.

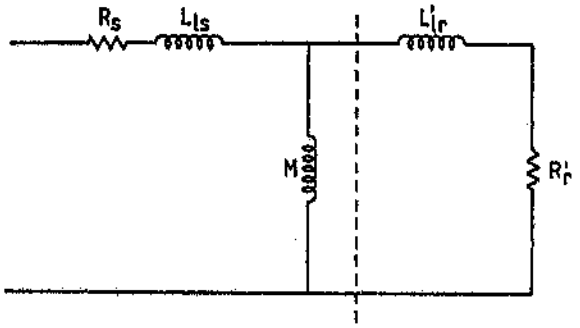

Figure 3.2 : **Equivalent Circuit Of An Induction Motor**

The same rectangular bar used in Appendix B is now divided into n equal sections along the depth of the bar, with each section having its own resistance and leakage inductance associated with it. Klingshirn and Jordan [16] have shown that such a rotor bar can be represented as a T-equivalent lumped parameter circuit as shown in Figure 3.3.

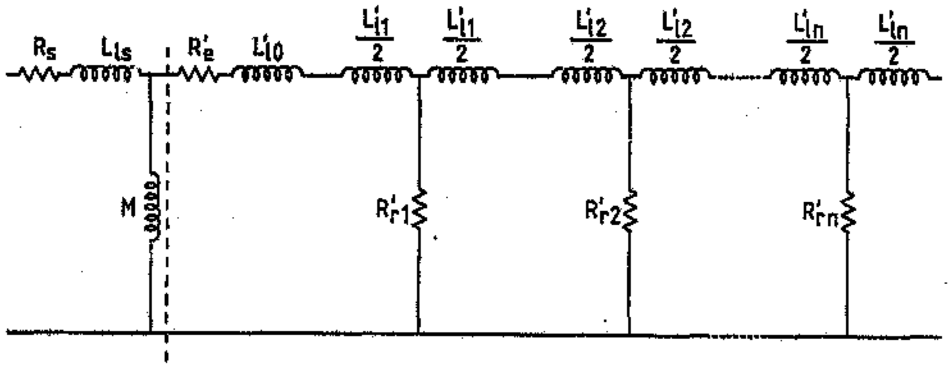

Figure 3.3 : **Equivalent T Circuit Of Induction Motor**

Both this circuit and that of Figure 3.2 are identical on the left of the dotted line, which represents the stator winding parameters and the mutual inductance. The new circuit has split the rotor values of Figure 3.2 into two components each. The resistance is split into the end-ring resistance R'_e and the bar resistance made up of $R'_{r1}...R'_{rn}$. The leakage inductance is composed of the inductance L'_{l0} whose flux links the whole bar i.e. it represents λ_0 of Appendix B, and the bar leakage inductance which is made up of $L'_{l1}...L'_{ln}$. The terminology used here is :

- a section (sec) denotes any individual segment that the bar has been divided into.
- a block (blk) denotes the sum of all the sections below and including the current section, as illustrated in Figure 3.4.

Each section of Figure 3.4 has a resistance of

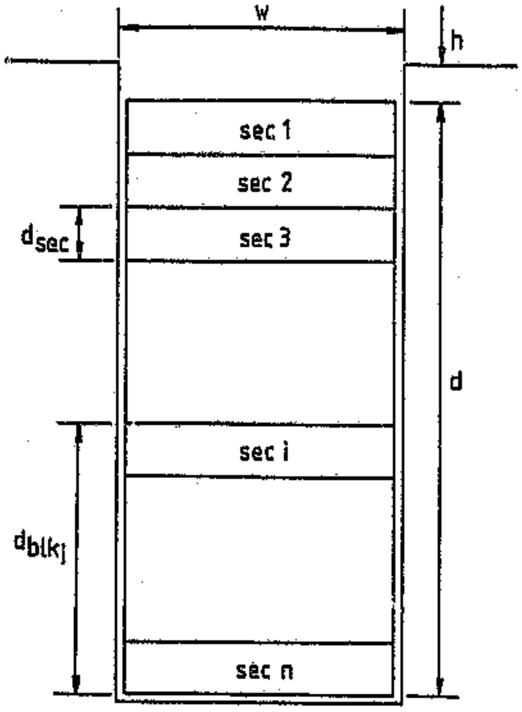

Figure 3.4 : **Rectangular Bar Divided Into n Equal Sections**

$$R_{sec}=\frac{\rho\, l_b}{w\, d_{sec}} \tag{3.1}$$

and a leakage inductance of

$$L_{l\,sec}=\mu_0 l_c \lambda_{sec} \tag{3.2}$$

where the permeance coefficient λ_{sec}, as shown below, is calculated by a similar procedure to that outlined in Appendix B.

The flux for any section is given a.

$$\Phi_{sec}=B_{blk}\,A_{sec} \tag{3.3}$$

where

$$A_{sec} = l_c\, d_{sec} \tag{3.4}$$

The flux density of the block is

$$B_{blk} = \mu_0 H_{blk} = \mu_0 \frac{N_{blk}\, I_{blk}}{w} \tag{3.5}$$

and, unlike the argument of Appendix B, the current of any block is now not a fraction of the total current, but is the total current for that block. This is so because the leakage inductance of that section due to the current flowing in that block is being calculated. Similarly, the number of turns for a block is not a portion of the total turns, as shown in Appendix B, it is the total for that block. Thus the total flux is

$$\Phi = \sum_{n} \Phi_{sec} \tag{3.6}$$

where

$$\Phi_{sec} = \frac{\mu_0}{w} l_c N_{blk}\, I_{blk}\, d_{sec} \tag{3.7}$$

Having followed a similar line of reasoning to that of Appendix B, equation (3.7) is the equivalent of equation (B.8). The integration for determining the total flux (Appendix B), has effectively been carried out here by adding the flux from each of the n sections. Thus the permeance coefficient for any section is derived from equation (3.7) as

$$\lambda_{sec} = \frac{d_{sec}}{w} \tag{3.8}$$

which is substituted into equation (3.2) to give the leakage inductance of a section.

Equations (3.1) and (3.2) give the resistance and leakage inductance for a section of each bar, whereas Figure 3.3 requires the per phase resistance and leakage inductance of the whole rotor cage referred to the stator winding. To achieve this, the resistance and inductance of each section must be :

- multiplied by the number of rotor slots S_r so that each value applies to the complete rotor winding
- divided by the number of phases q to work on a per phase basis
- multiplied by the equivalent turns ratio T_r which is given by

$$T_r = \left(\frac{S_s C_s K_{ws}}{S_r K_{wr} P_c} \right)^2$$

where

S_s, S_r = number of stator and rotor slots

C_s = number of stator conductors per slot

P_c = number of stator parallel circuits

K_{ws}, K_{wr} = stator and rotor winding factors

Thus $R'_{r\,\mathrm{sec}}$ and $L'_{l\,\mathrm{sec}}$ of Figure 3.3 (where sec = 1..n) are given by

$$R'_{r\,\mathrm{sec}} = \frac{T_r S_r}{q} \frac{\rho l_b}{w d_{\mathrm{sec}}}$$

$$L'_{l\,\mathrm{sec}} = \frac{T_r S_r}{q} \mu_0 l_c \lambda_{\mathrm{sec}}$$

3.4. Other Lumped Parameter Circuits

The procedure of Section 3.3 has been to calculate an inductance and a resistance of each section of bar, and then to use these values in the T equivalent circuit. There are other lumped parameter circuits for which the above analysis is equally valid, since these other circuits also require an inductance and a resistance of each section. The circuits that have been analysed are listed below and their differential equations appear in Appendix C.

1) The L circuit, where each section is represented as an inductance in series with its resistance, and each section is in parallel with the next as shown in Figure 3.5.

2) The Pi circuit which has each section represented as an inductance with twice the resistance of each section on either side of the inductance (see Figure 3.6).

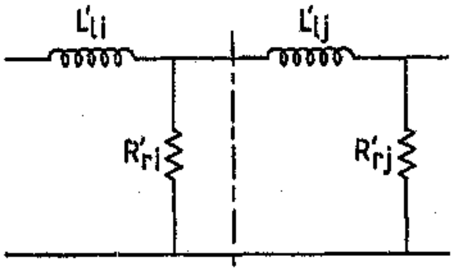

Figure 3.5 : **Lumped Parameter L Circuit**

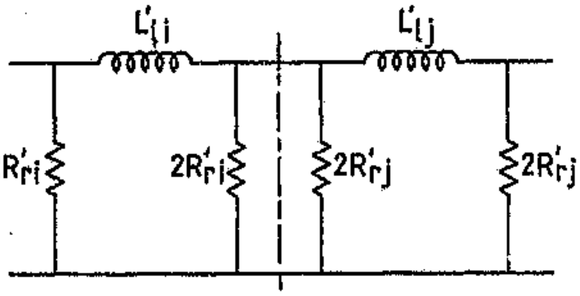

Figure 3.6 : **Lumped Parameter Pi Circuit**

3) An improved Pi circuit (as suggested by Babb and Williams [4]) which has the complex form shown in Figure 3.7 for each section of the bar. This circuit attempts to accurately predict the current present in each section of the bar, by weighting the inductances in the ratio one sixth, two thirds, one sixth (1:4:1). The method is based on Simpson's integration rule which is an accurate, high order numerical integration routine with its three predicted points in the ratio 1:4:1.

One way of understanding the equivalence of these lumped parameter circuits is to think of the section resistance as a resistance along the length of the bar and the section inductance as a link between one section and the next. Consider a rotor bar divided

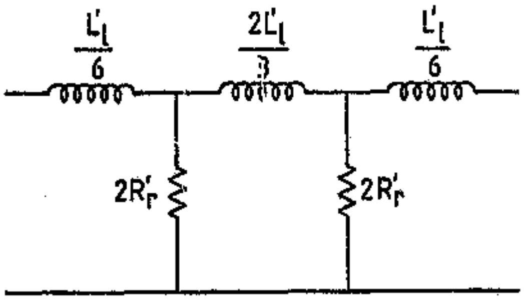

Figure 3.7 : Lumped Parameter Improved Pi Circuit

into four equal sections, and the typical non-linear current distribution for each section as shown in Figure 3.8. The current in the bottom section (section 1) is fairly constant along its depth, whereas the current in the top section (section 4) is highly non-linear.

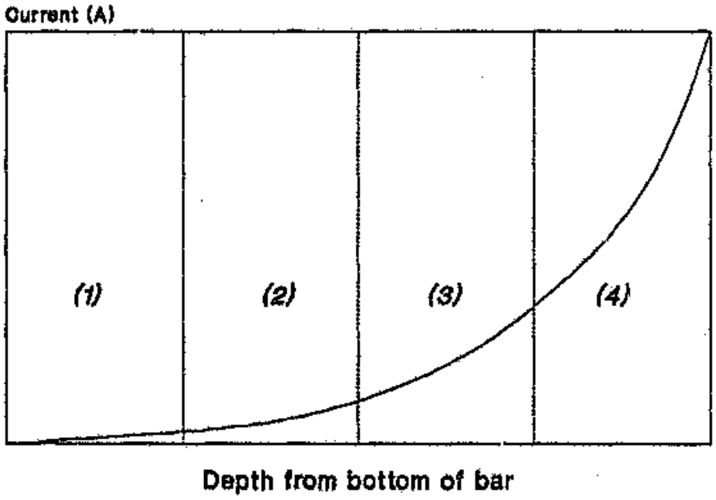

Figure 3.8 : Typical Current Distribution Along The Depth Of A Rotor Bar

The circuit of each section attempts to calculate the current distribution present in that section by predicting the current at one or more points, depending on which circuit is used. The overall circuit therefore tries to predict the non-uniform current along the depth of the bar. The lumped parameter circuits differ from each other in the number of currents predicted per section, the weightings that the prediction points have and where in the section the currents are predicted. This is analogous to the various numerical integration routines which also differ from each other by the number of points used, where the points are and their weightings. Each circuit will now be explained in terms of predicting the current along the curve of Figure 3.8, from which the accuracy of the circuit may be anticipated. In each case it is assumed that the bar is divided into four sections.

The L circuit predicts only one current per section (i.e. 4 points along the complete curve), that current being at the top of the section, as shown in Figure 3.9. This Figure shows that the circuit takes each predicted current as constant over that section, so that the error is the difference between the area under the predicted (stepped) curve and the actual curve. This circuit is based on the rectangle rule for integration, which is an order 0 method and will thus not be particularly accurate.

The T circuit also predicts one current per section (i.e. 4 points), but here that current is in the middle of the section, as shown in Figure 3.10. This circuit is based on the mid-point rule, which is a special case of the rectangle rule. It is also an order 0 method, but will be more accurate than the rectangle rule. The improved accuracy can be seen in Figure 3.10 which shows that the predicted curve follows the actual curve closer than the method of Figure 3.9. Also, the area under the predicted curve is closer to the area under the real curve than the L circuit can predict.

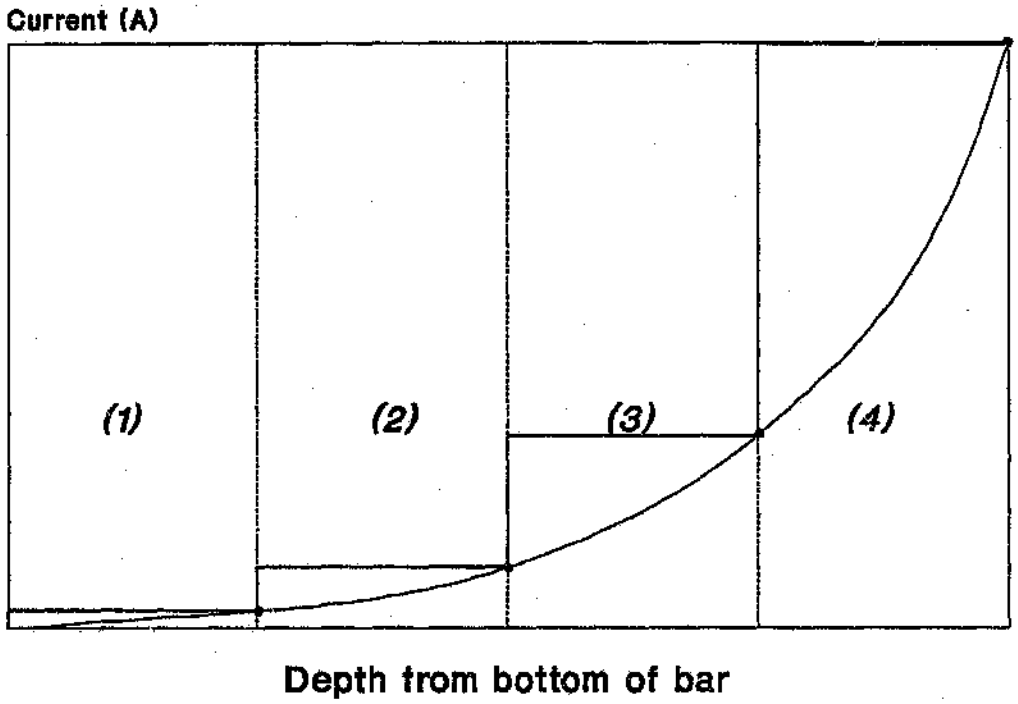

Figure 3.9 : Predicting The Current Distribution Of A Rotor Bar Using The L Circuit

The Pi circuit predicts two currents per section (i.e. 8 points along the complete curve), one at the top and one at the bottom of each section, as shown in Figure 3.11. Here the predicted current for a section is the straight line joining the two points in that section, which is obviously a more accurate method than the other two. This circuit is based on the trapezoidal rule which is an order 1 method.

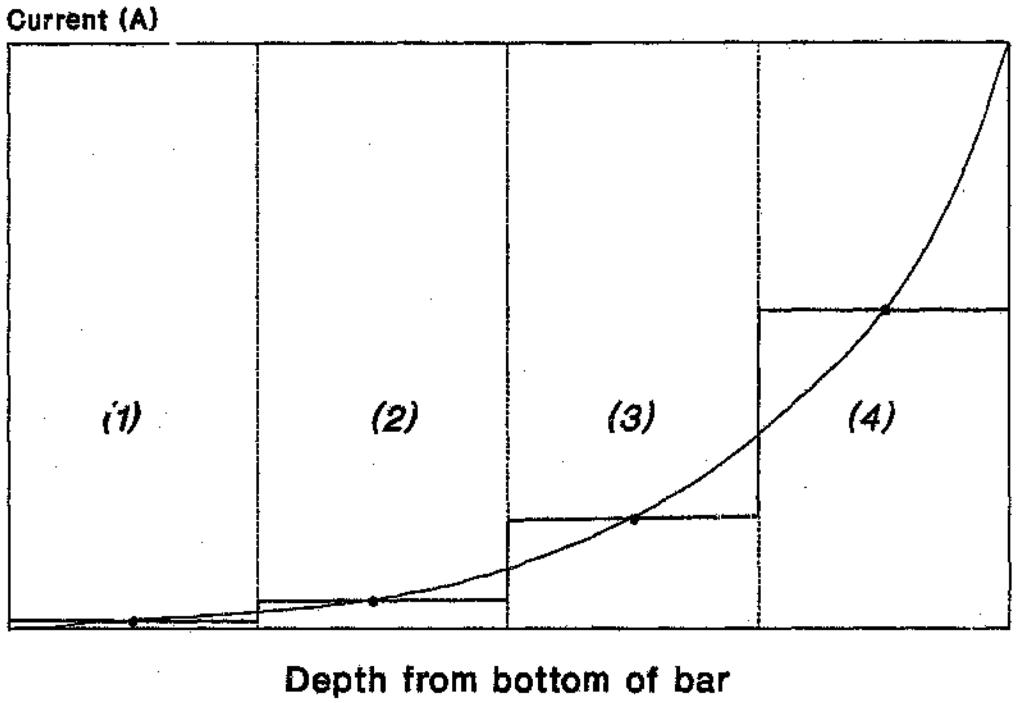

Figure 3.10 : **Predicting The Current Distribution Of A Rotor Bar Using The T Circuit**

The improved Pi circuit predicts three currents per section (i.e. 12 points along the complete curve), one at the top, one at the bottom and one in the middle, as shown in Figure 3.12. From this Figure it can be deduced that this circuit should be the most accurate of all the models. This is verified by the fact that the improved Pi circuit is based on Simpson's rule which is an order 2 method.

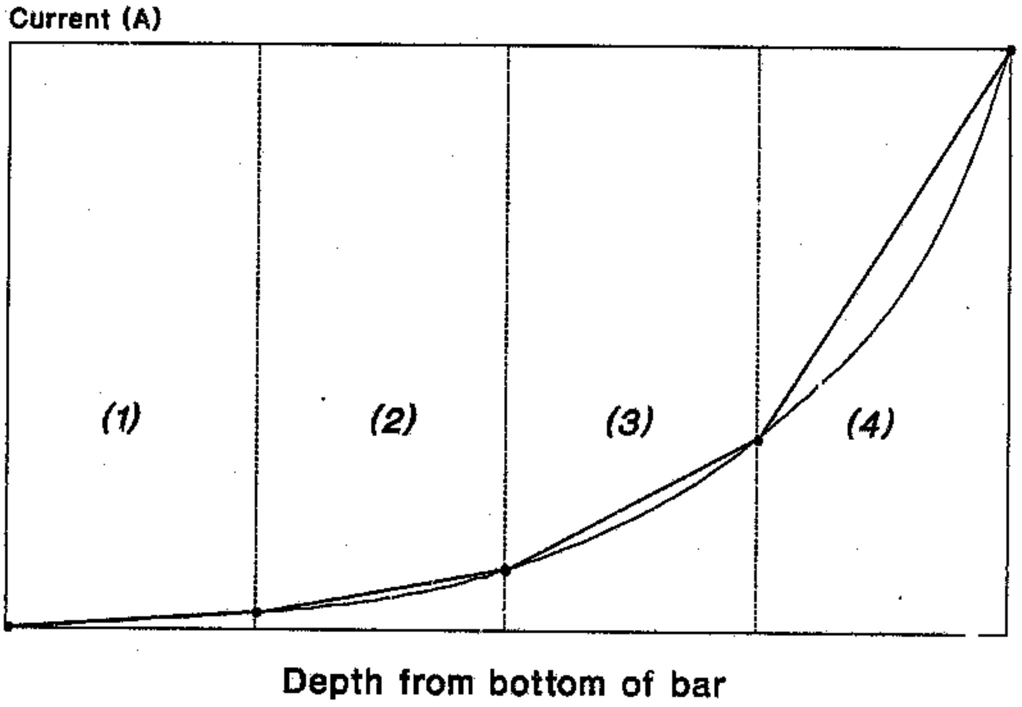

Figure 3.11 : Predicting The Current Distribution Of A Rotor Bar Using The Pi Circuit

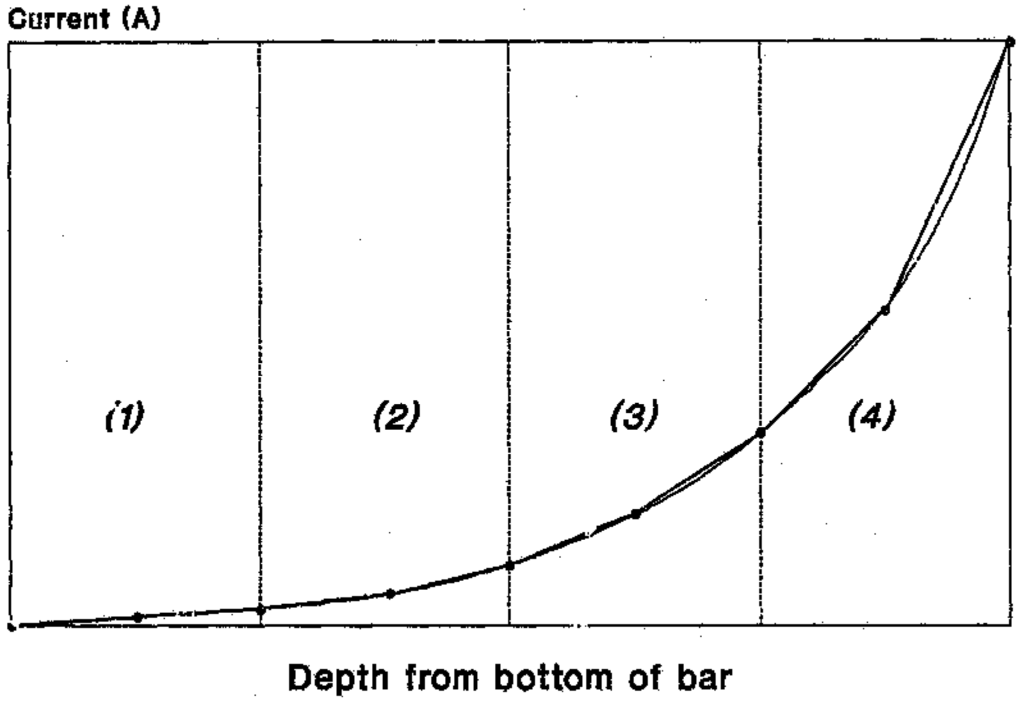

Figure 3.12 : Predicting The Current Distribution Of A Rotor Bar Using The Improved Pi Circuit

3.5. Accuracy Of Equivalent Circuit

In this Section, comparisons of the accuracy of the four equivalent circuits will be given, as were developed by Levy et al [39]. These comparisons will be made at frequencies across the typical expected spectrum of frequencies found in variable speed drive motors (as given in Section 3.1) and will also examine the effect of the number of sections used to model the bar.

Depending on which circuit is under consideration, the appropriate equivalent circuit can be constructed (i.e. one of those of Figures C.2, C.4 or C.6). The inductances in the circuit are converted to reactances, using the particular frequency that is being examined. The only details required to construct this circuit are slot and bar dimensions which are readily available from motor design data. The Thevenin impedance of the rotor circuit is then found giving an equivalent R and X for the rotor.

From the same design data, the DC value of the rotor resistance and leakage reactance can be obtained. The frequency dependent correction factors obtained from the analytical solution as given by Alger [14], are then applied to the DC rotor values. These corrected values are therefore the effective resistance and reactance of the rotor including deep bar effects.

The impedance of the rotor as given by the lumped parameter circuit (subscript Model) is then compared with the corresponding impedance obtained by applying the correction factor (subscript Analytical). This is expressed in terms of the percentage impedance error defined as

$$\% \quad Impedance \quad Error = 100\left(\frac{Z_{Analytical} - Z_{Model}}{Z_{Analytical}}\right) \tag{3.9}$$

where each impedance is given by

$$Z = \sqrt{R^2 + (j\omega L)^2} \tag{3.10}$$

The comparisons are for a 268 kW motor with a rectangular bar 4 mm wide and 50 mm deep. Initially the errors of all four models will be compared by varying the number of sections used and the frequency of the current present in the bar. The number of sections shown ranges from two to fifteen to show the trend, whereas practically no more than eight to ten sections would be used for a simulation because of numerical processing limitations. Three different frequencies have been considered, 50 Hz, 500 Hz and 2500 Hz, which accounts for most of the range of expected frequencies of variable speed drive motors. Figures 3.13, 3.14 and 3.15 show the percentage impedance error for the circuits at the different frequencies. Some points should be noted about the graphs at this stage

1) The error for the first few sections of some of the curves have purposefully been omitted from the graphs. The errors at these points are so large that they would have masked the trend of the other curves had they been included.

2) A positive error implies that the model's impedance is lower than the analytical impedance and a negative error implies that the model's impedance is higher than the analytical impedance.

3) The error decreases to zero as the number of sections increases. This result is expected because the larger the number of sections used, the more uniform will be the current distribution along the depth of that section. The non-uniform current distribution across the whole bar has been segmented into many sections having uniform distribution across each section.

4) An increase in frequency is accompanied by an increase in the error of all the lumped parameter circuits. This result is also expected because at the higher frequencies, skin effect is more pronounced. The less uniform current distribution

across each segment of the bar at higher frequencies means that all of the circuits are less able to account for these effects. (Note that the scales of the Y axes are different for the three graphs)

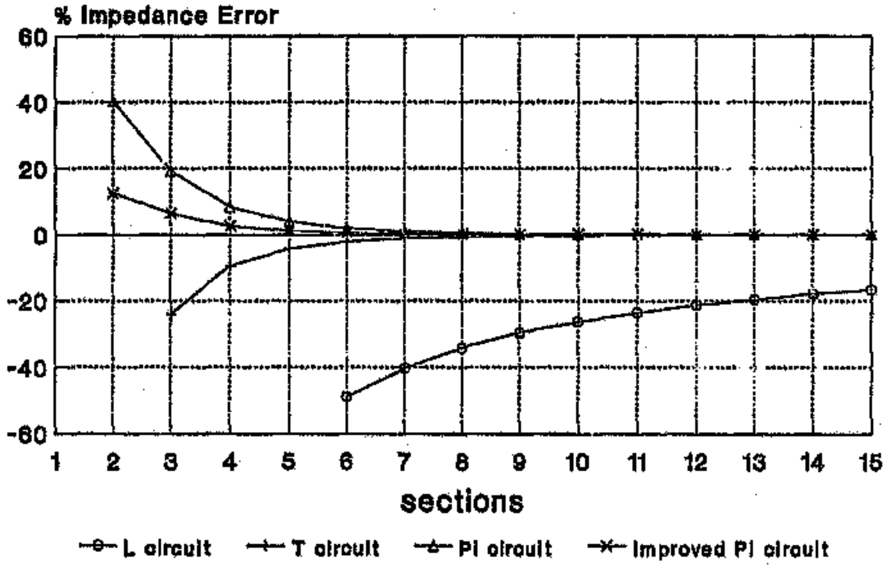

Figure 3.13 : Variation Of Percentage Impedance Error With Number Of Rotor Bar Sections For The Above Four Circuit Models. Bar Current Frequency = 50 Hz

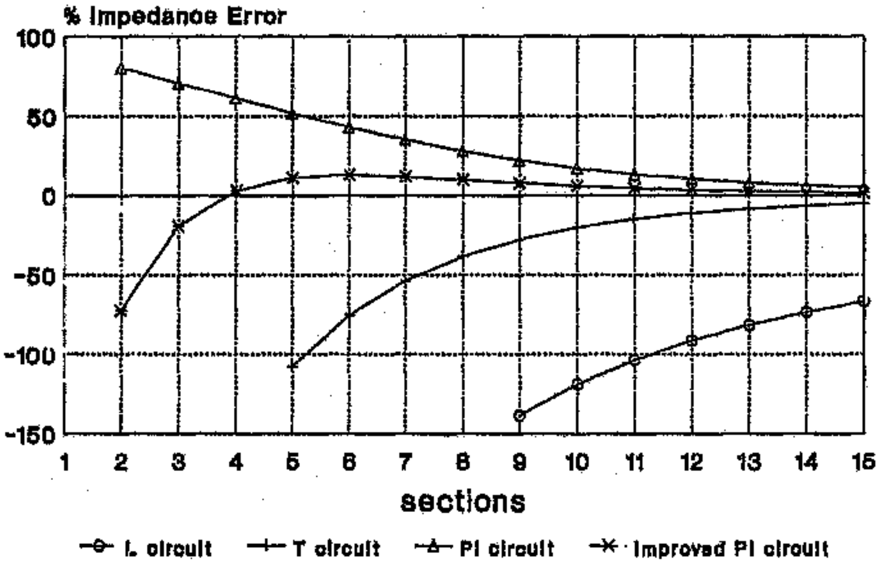

Figure 3.14 : Variation Of Percentage Impedance Error With Number Of Rotor Bar Sections For The Above Four Circuit Models. Bar Current Frequency = 500 Hz

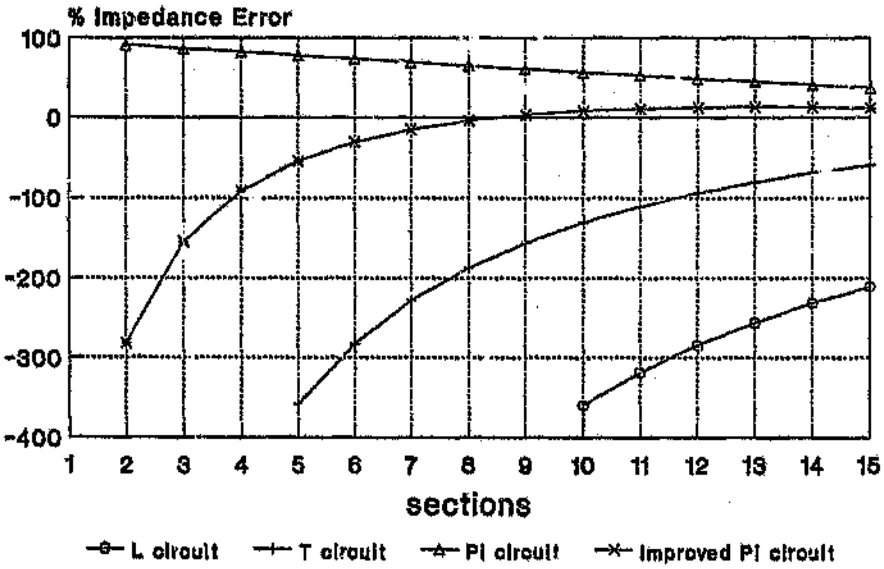

Figure 3.15 : Variation Of Percentage Impedance Error With Number Of Rotor Bar Sections For The Above Four Circuit Models. Bar Current Frequency = 2500 Hz

From the graphs it can be seen that the accuracy of the L circuit is much worse than the other circuits, as previously predicted. In fact for the higher frequency applications, the L circuit would need many more than fifteen sections to achieve any sort of reasonable accuracy. Thus this circuit has been discarded and will not be included in any further comparisons. The Pi and the T circuits seem to be equally accurate at the lower frequencies (the percentage error being positive and negative respectively), whereas the Pi circuit is significantly more accurate at the higher frequencies. The error of the Pi circuit is consistently greater than zero and that of the T circuit is consistently less than zero; this result is predicted by Babb and Williams [4]. The improved Pi circuit is the most accurate because the error converges faster to zero with fewer sections, than it does in the other circuits.

A factor which has thus far been ignored but needs to be considered is the time required for simulation. This time is dependent on the number of states of the system. For a particular model, the number of loop currents necessary to define the equivalent circuit of that model will give the number of d-axis or q-axis states i.e. twice the number of loop currents will give the total number of states required for that model. The equivalent circuit of Figure 3.2 requires two loop currents, thus the traditional three phase induction motor model comprises four states, two for the d-axis and two for the q-axis. The larger number of states necessary for the motor model which takes account of deep bar effects, is dependent on the number of sections used and on which "deep bar" model has been used. The reduced equivalent circuit for the T model of Figure C.2 requires one loop current for the stator and one for each rotor section, giving a total of $(2*\mathit{sections}+2)$ states for the whole motor. The reduced equivalent circuit for the Pi model of Figure

C.4 requires one loop current for the stator, one for loop 0 and one for each rotor section, giving a total of $(2*\mathit{sections}+4)$ states. The two additional states occur because the inductance L'_{l0} cannot be combined with L'_{l1} as it is in the T circuit. The improved Pi circuit of Figure C.6 requires one loop current for the stator and <u>two</u> for each rotor section giving a total of $(4*\mathit{sections}+2)$ states.

For this comparison, a sinusoidal source supplying a 268 kW induction motor with rectangular bars was simulated for two seconds [illegible] time, (the time required for the machine to accelerate from zero speed to the full speed steady state condition) on an HP 9000 Series 300 workstation. Two sets of results are given for each circuit, the first has the number of sections so arranged that each circuit has fourteen states and the second so that each circuit has eighteen states.

Table I : Computer Simulation Times For Various Lumped Parameter Circuits

Model	Sections	States	% Error @ 50 Hz	% Error @ 500 Hz	% Error @ 2500 Hz	Time (mins)
T	6	14	-2.07	-75.48	-282.06	42.95
Pi	5	14	3.96	51.84	78.17	44.12
Improved Pi	3	14	6.44	-19.21	-154.91	42.47
T	8	18	-0.67	-38.54	-187.27	79.40
Pi	7	18	1.11	34.93	69.49	94.50
Improved Pi	4	18	2.63	2.69	-92.00	74.85

The first set of results of Table I shows that the simulation times are approximately equal for the three circuits and, now that the number of states has been considered, the Pi circuit seems to be the most accurate. When the second set of results is examined it is seen that for a small increase in simulation time all the circuits display improved accuracy, and the improved Pi circuit shows improved accuracy in the low to medium frequency ranges. Regardless of which circuit is used, at frequencies greater than 500 Hz all the circuits are unacceptably inaccurate, and the next Section gives an algorithm which successfully improves the accuracy of all the circuits.

3.6. Algorithm To Improve The Accuracy Of Models

To increase the accuracy of the lumped parameter circuits, a new algorithm has been developed which divides the bar into unequal sections, the smallest section being at the top of the bar. This algorithm calculates a value, called a *unit* , which is a fraction of the total depth of the bar. A geometric series is then used such that the depth of each section is equal to *unit* multiplied by an increasing number of the form num^{sec-1}, where sec is the number of the section whose depth is being calculated and *num* is a parameter greater than 1.0. By setting *num* to 1.0, the equal sections criterion of Section 3.3 is obtained and by setting *num* to a value greater than 1.0, improved accuracy of the models is obtained. The algorithm reduces the error because the smaller sections at the top of the bar account far more accurately for the highly non-uniform current distribution that exists in that portion of the bar.

Figures 3.16, 3.17 and 3.18 show the error of the improved Pi circuit as a function of *num* for 3, 5 and 7 sections respectively, evaluated at the same frequencies that were examined previously (the bar shape being rectangular as before). From these graphs it is seen that a different "ideal" value for *num* exists for each frequency. Consequently, a particular value of *num* (referred to as the optimum value), must be chosen which ensures that the errors obtained at all frequencies are low. It is also clear that the number of sections used has a large influence on the optimum value of *num* to be used. Thus from the three graphs, the optimum values of *num* for 3, 5 and 7 sections of the improved Pi circuit are 4.4, 2.2 and 1.8 respectively. Similarly, the other circuits will also have different optimum values of *num*.

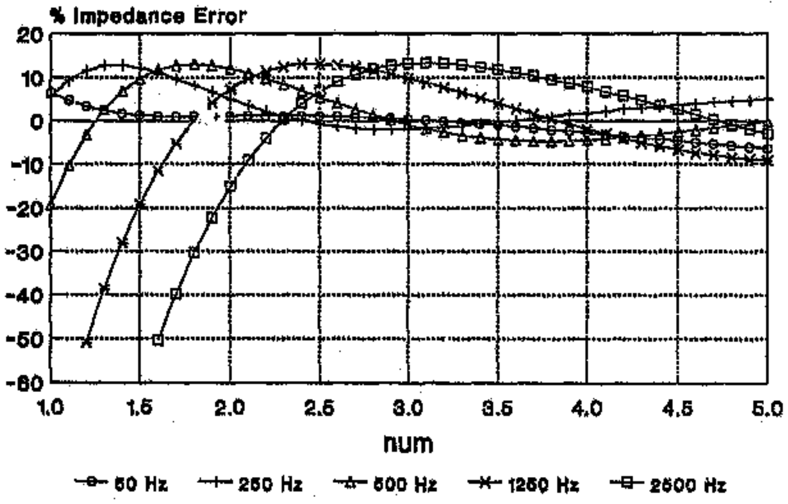

Figure 3.16 : Variation Of Percentage Impedance Error With Value Of *num* At Different Frequencies For Three Sections Of The Improved Pi Circuit

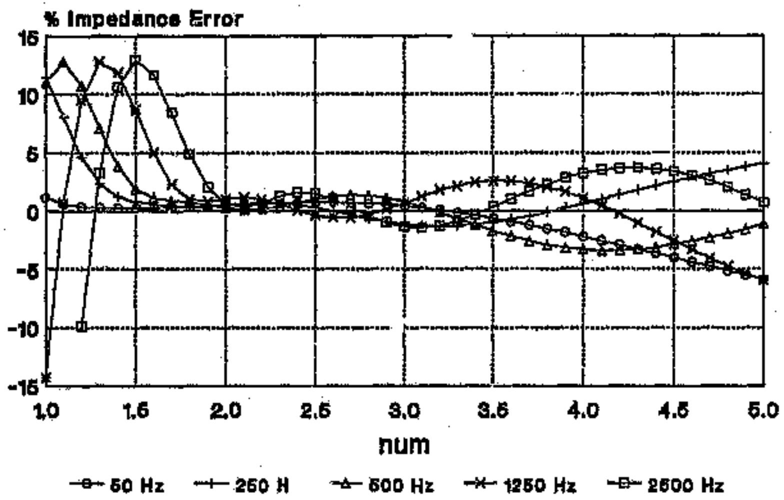

Figure 3.17 : Variation Of Percentage Impedance Error With Value Of *num* At Different Frequencies For Five Sections Of The Improved Pi Circuit

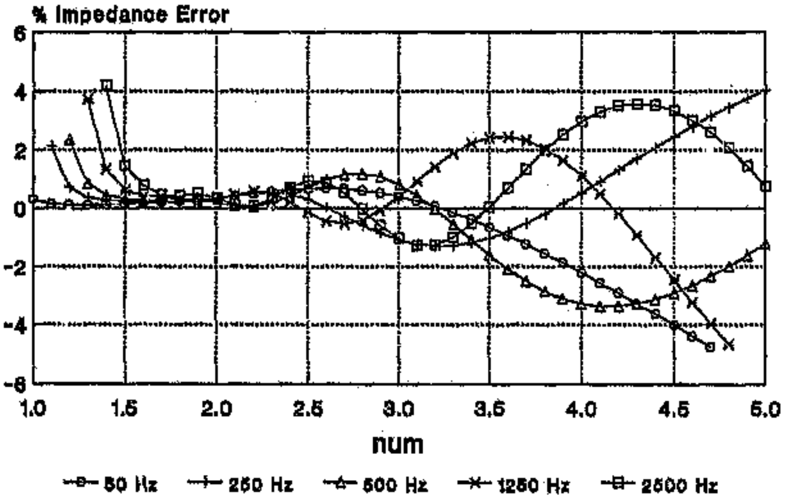

Figure 3.18 : Variation Of Percentage Impedance Error With Value Of *num* At Different Frequencies For Seven Sections Of The Improved Pi Circuit

Appendix D gives a complete set of graphs to find the optimum value of *num*. For each circuit, graphs are given for the number of sections ranging from two to fifteen.

The numerical processing ability available at the present time restricts the number of sections to about eight or ten, but the graphs for up to fifteen sections have been included because the ever-improving computing power may soon allow larger models to be simulated.

Table II shows the accuracy of the circuits for the same analysis as that used for Table I where the errors are now given for *num* set to the optimum value obtained from Appendix D. It can be seen that the errors for the higher frequencies have been dramatically reduced by choosing optimum values of *num* to partition the bar.

Table II : Improvements In Accuracy From Varying *num*

Model	Sections	num	% Error @ 50 Hz	% Error @ 500 Hz	% Error @ 2500 Hz	Time (mins)
T	6	2.1	-4.11	-4.25	-5.52	165.93
Pi	5	2.7	5.82	7.88	6.84	160.63
Improved Pi	3	4.4	-4.21	-3.03	3.65	158.23
T	8	1.7	-2.03	-2.50	-3.42	277.63
Pi	7	1.8	2.44	3.17	4.30	277.62
Improved Pi	4	2.6	0.81	1.83	0.22	279.12

The time taken to simulate these results is on average 3.5 times longer than the corresponding time for *num*=1.0. This increase in simulation time is deemed acceptable considering the increases in accuracy of up to sixty times achieved at certain frequencies. The increase in simulation time is expected because of the electrical time constants involved. The time constant of any section of the lumped parameter circuit is given by

$$\begin{aligned}\tau &= \frac{L}{R} \\ &= \left(\frac{\mu_0\, l_c\, d_{sec}}{w}\right)\Bigg/\left(\frac{\rho\, l_b}{w\, d_{sec}}\right) \\ &= \frac{\mu_0\, l_c\, d_{sec}^2}{l_b\, \rho} \qquad (3.11)\end{aligned}$$

from which it is seen that the time constant is proportional to the square of the section depth. If the depth of each section is equal (i.e. *num*=1.0), the time constant for each section will be the same, whereas if unequal section depths are used, the time constants will be different. Table III shows typical section depths for the different circuits for the same rotor bar used before. From the Table it is seen that the ratio of the bottom section depth to the top section depth can be in the order of 50. Therefore the ratio of the time constants of the bottom and top bar sections can be as high as 2500. Systems of equations having such high ratios of time constants are termed stiff and need specialised numerical differential equation solvers. Although these equation solvers cope with stiff equations far better than ordinary solvers, they are still somewhat slower (see Enright et al [18]).

This analysis has shown that improved accuracy of deep bar models can be achieved by having smaller sections at the top of the bar and the largest section at the bottom of the bar. The improved Pi model shows superior accuracy at the higher frequencies, with simulation times being very comparable to the other circuits.

Table III : Section Depths For Different Values Of *num*

Sections	Depth (mm) *num*=1.0	Depth (mm) T circuit *num*=2.1	Depth (mm) Pi circuit *num*=2.7	Depth (mm) Improved Pi *num*=2.0
1	10.0	1.38	0.60	1.61
2	10.0	2.90	1.61	3.23
3	10.0	6.09	4.35	6.45
4	10.0	12.78	11.74	12.90
5	10.0	26.85	31.70	25.81

3.7. Implementation Of Different Bar Shapes

Although the improved Pi circuit is the most accurate, as shown in the previous Section, the accuracy and simulation time of all three circuits (T, Pi and improved Pi) are similar and these have all been implemented in CASED. This has been done because situations exist where it is beneficial to use more sections of a less accurate circuit to achieve the same results to those obtained from fewer sections of a very accurate circuit. An example of this is the case study of Section 3.8.2, where the bar shape necessitated using hand calculations for the depth and width of each section (as explained later). The bar (Figure 3.26) is composed of five distinct segments - the top and bottom half circles, the rectangular portion, the tongue and the trapezoidal portion - and therefore needs to be divided into at least five sections. For this example the rectangular and trapezoidal portions were divided into more than one section each, giving a total of eight sections. These eight sections gave good accuracy using the T model, but would have taken far too long to simulate using eight sections of the improved Pi model.

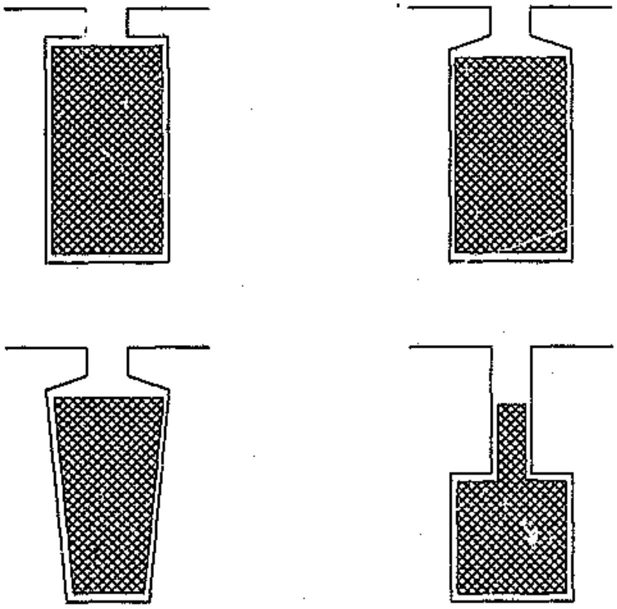

Figure 3.19 : Bar Shapes Implemented In CASED

Most bar shapes can be simulated and four of the commonly used shapes have been directly implemented. These four shapes, shown in Figure 3.19, are

1) A rectangular bar in an open slot.

2) A rectangular bar in a semi-closed slot with a wedge.

3) A trapezoidal bar in a semi-closed slot with a wedge. Here the wider portion of the bar can be at the top or the bottom. The width of any section is taken as the average width across the depth of that section.

4) A Tee shaped bar, which includes an inverted Tee where the upper portion of the bar is wider than the lower portion. The algorithm arranges the depths of the sections so that no section will ever straddle the part of the bar where the width changes.

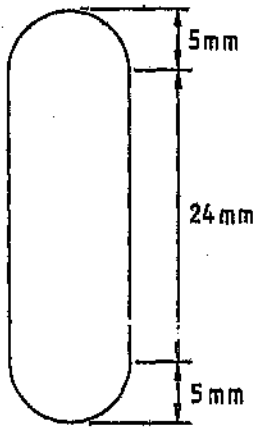

Figure 3.20 : Example Bar Shape

This implementation of the deep bar model has also been successfully applied to a double cage motor, as discussed in Chapter 4. Finally, a method has been implemented which allows virtually any bar shape to be simulated, but which does require some hand calculation by the user. If a bar shape is required which will not fit into one of the standard bar shapes shown in Figure 3.19, an alternative method is required to calculate the depth and width of each section. Take for example the shape shown in Figure 3.20, where the following user calculated steps would be required :

1) Divide the bar into a certain number of sections.

For the example, the half circles at the top and bottom would each be a section, and dividing the middle portion into three sections gives a total of five sections with depths from top to bottom of 5 mm, 8 mm, 8 mm, 8 mm, 5 mm.

2) Calculate the width of the bar for each section. If the width is not constant over the section, an average width is calculated.

The three middle sections are obviously each 10 mm wide and the top and bottom sections have an average width of 5 mm.

3) Calculate the width of the slot for each section, if it is different to the bar widths of step 2 above.

The algorithm to improve the accuracy of the models is only used with the four standard bar shapes; it does not apply to the method just described, as seen by the depths of each section given in step 1 above. To apply the algorithm to the above example, the user must substitute the steps below for step 1 above.

1a) Calculate the bar divisor *bd* as

$$bd = \sum_{\mathrm{sec}=1}^{\mathrm{sec}=sections} num^{\mathrm{sec}-1} \tag{3.12}$$

For the example, assume *sections* = 5 and the improved Pi circuit is being used, where *num* = 2.0

$$\begin{aligned} bd &= 2.0^0 + 2.0^1 + 2.0^2 + 2.0^3 + 2.0^4 \\ &= 31.0 \end{aligned} \tag{3.13}$$

1b) Calculate the unit depth *ud* as

$$ud = \frac{total \quad depth}{bd} \tag{3.14}$$

For the bar of Figure 3.20, the total bar depth is 34 mm, so that

$$\begin{aligned} ud &= \frac{34}{31.0} \\ &= 1.0968 \end{aligned} \tag{3.15}$$

1c) Calculate the depth of each section as

$$d_{sec} = ud \cdot num^{sec-1} \qquad \text{sec} = 1..sections \tag{3.16}$$

which, for the example, gives

$$\begin{aligned} &d_1 = 1.0968, d_2 = 2.1936, d_3 = 4.3872, \\ &d_4 = 8.7744, d_5 = 17.5488, \end{aligned}$$

3.8. Model Verification

This Section gives two case studies to show the validity of the models. The first example is for a sinusoidal input waveform to the motor and the second is for a motor supplied from an inverter.

3.8.1. Sinusoidal input waveform

The system under consideration is a sinusoidal supply feeding an induction motor with no attached load. The motor is a 254 kW, 3300 V, 3 phase, 50 Hz, 4 pole squirrel cage induction motor with fifty T-shaped rotor bars. All results are given for the motor initially at rest. The motor is then supplied with full rated sinusoidal voltage and is allowed to run up against its own inertia.

The measured results have been obtained using a "double disc" system. This involves connecting one disc to the shaft of the motor under test and connecting the other disc to a reference motor, which is placed so that the discs line up axially and are separated from each other by only about 10 mm. Both discs are opaque and have many slots accurately machined into their periphery. A concentrated light source is shone onto a section of the periphery, spanning approximately five slots. The light that crosses both sets of slots is focussed onto a photo-transistor by means of an optical lens. The second motor is driven at a constant speed and thus the output of the transistor is a pulse train whose frequency is directly proportional to the speed of the test motor. The speed can be differentiated to give acceleration, which is proportional to the torque because the motor is unloaded. Thus this measurement system gives a torque-time and speed-time trace of the motor under test. More information on this measurement technique as well as circuit diagrams of the measuring system can be found in Gomes [24].

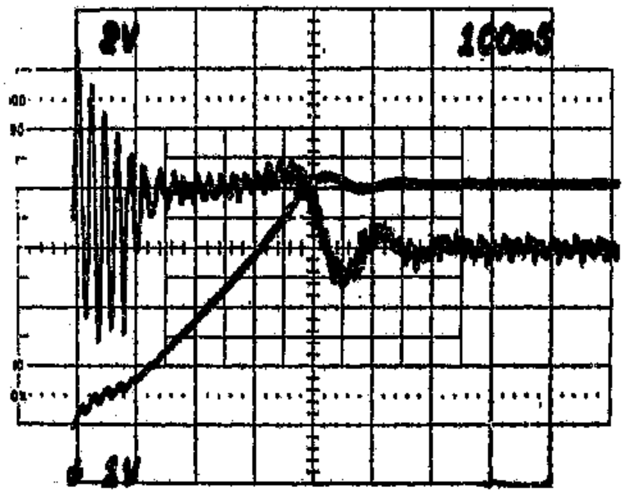

Figure 3.21 : **Measured Torque And Speed Trace Of 254 kW, 3300 V, 4 Pole Induction Motor With T-Shaped Rotor Bar (Time = 100 ms/div, Torque = 1.65 PU/div, Speed = 0.25 PU/div)**

Figures 3.21 and 3.22 show the measured results which have been recorded on a storage oscilloscope and then photographed. From these graphs it will be seen that the first peak of speed occurs at 0.43-0.46 seconds, the initial peak of torque is 5.28 PU and the pull-out torque is 2.10 PU. Two sets of photographs have been given for the same run-up condition which show slightly different results due to different initial conditions of the supply and some noise on the measuring system, thus a small discrepancy appears in the results of Figures 3.21 and 3.22.

Figure 3.23 shows the predicted results obtained using the improved Pi model with the rotor bar divided into four sections. The value of *num* used here is 2.6, as shown in

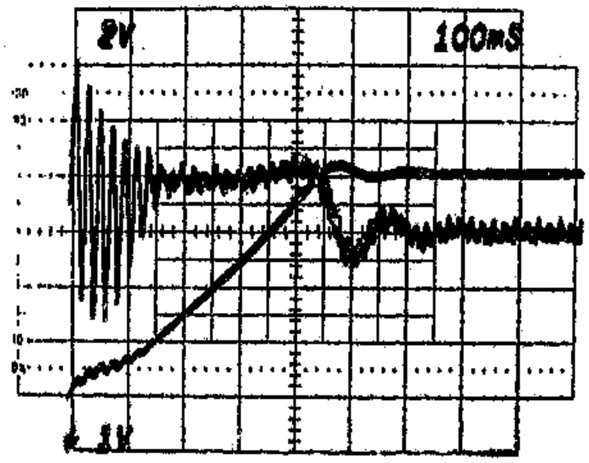

Figure 3.32 : Measured Torque And Speed Trace Of 254 kW, 3300 V, 4 Pole Induction Motor With T-Shaped Rotor Bar (Time = 100 ms/div, Torque = 1.65 PU/div, Speed = 0.25 PU/div)

Table II. The overall shape of both the torque and the speed trace are very similar to the measured results, including the initial oscillations in the speed. The first peak of speed occurs at 0.52 seconds, the initial peak of torque is 4.1 PU and the pull-out torque is 2.0 PU. These results show that the simulation model is able to predict the shape of the torque and speed curve, but there is a difference in the measured and predicted magnitudes. This discrepancy can be attributed to the fact that thus far saturation effects in the motor have been neglected. If saturation was accounted for, the large starting current would cause the leakage flux paths to saturate which would increase the magnitude of the torque peaks. This effect has been verified in Chapter 5 which deals with saturation of the tooth tip leakage flux.

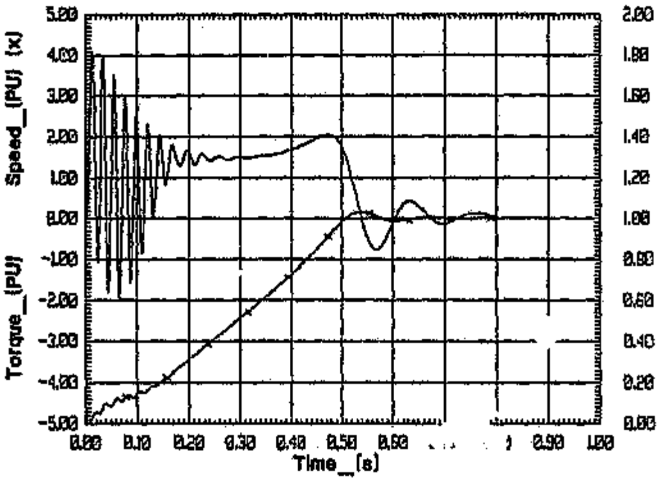

Figure 3.23 : **Predicted Torque And Speed Curves Of 254 kW, 3300 V, 4 Pole Induction Motor With T-Shaped Rotor Bar Using Improved Pi Model**

To illustrate the effectiveness of the new deep bar models developed, simulations were performed with the bar resistance and leakage inductance fixed at two sets of values. These are :

1) The 50 Hz or starting values which can only be obtained from correction curves as given in Alger [14] or from tests performed on the motor.

2) The DC or running values which are obtained from the design calculations.

Figures 3.24 and 3.25 show the predicted results for the 50 Hz and DC cases respectively. Figure 3.24 shows that although the motor runs up in the correct time, the predicted torque is far too high and the speed trace has no overshoot as measured. Figure 3.25 shows a starting torque which is half the magnitude that it should be and consequently the motor takes 1.84 seconds to run up to speed. The corresponding currents are shown in Appendix E, along with those of the deep bar model.

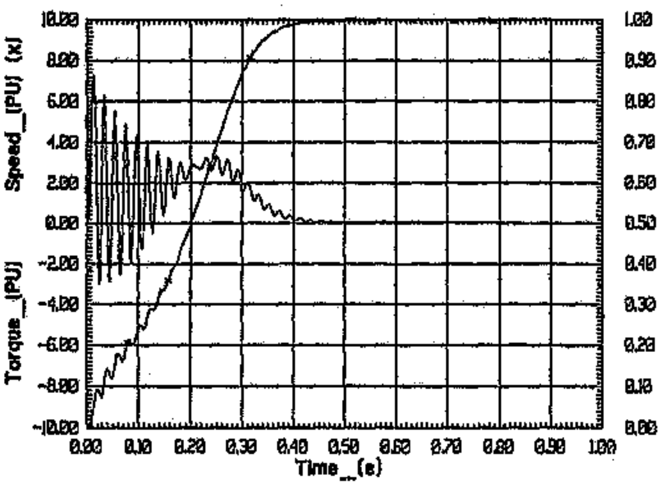

Figure 3.24 : **Predicted Torque And Speed Of 254 kW, 3300 V, 4 Pole Induction Motor With T-Shaped Rotor Bar Using The Traditional Model And The 50 Hz Rotor Parameters**

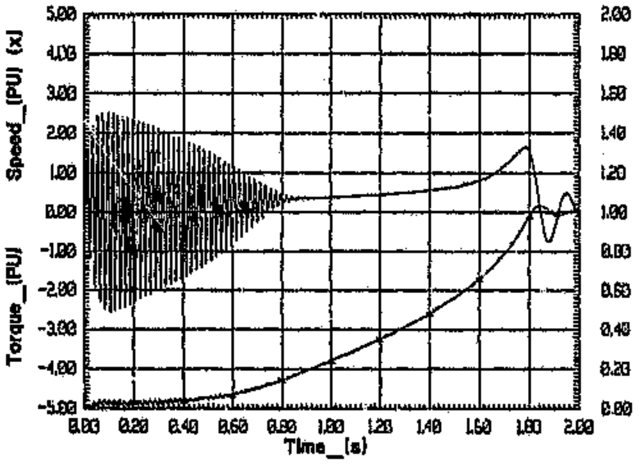

Figure 3.25 : **Predicted Torque And Speed Of 254 kW, 3300 V, 4 Pole Induction Motor With T-Shaped Rotor Bar Using The Traditional Model And The DC Rotor Parameters**

This case study has shown that the deep bar models will give far better correlation with measured results than the traditional model. The rotor bars of the test motor are T-shaped, which the new model is able to easily cope with.

3.8.2. Inverter input

This example is of a 70 kW, 270 V, 8 pole induction motor supplied from a PWM inverter. The motor has the rotor bar shape and dimensions shown in Figure 3.26. The results are given for the motor initially at rest and lightly loaded; with the inverter set to 7 Hz the motor is then allowed to accelerate up to speed. When the motor was constructed and tested, instability problems were discovered at 7 Hz.

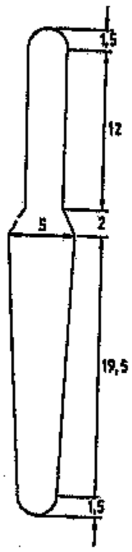

Figure 3.26 : Bar Shape And Dimensions Of 70 kW, 270 V, 8 Pole Induction Motor

The shape of the rotor bar implies that none of the standard pre-defined deep bar shapes can be used for the simulation. Thus the user defined bar division has been used with eight sections defined. The first and last sections are taken as the half circles at the top and bottom of the bar; the rectangular portion of the bar is divided into two sections 3 mm and 9 mm deep. The tongue portion is taken as one section and the trapezoidal portion is split into three sections 2 mm, 6.5 mm and 11 mm deep. The T circuit has been used because the accuracy of eight T sections is acceptable and it uses fewer states than the other circuits.

Figures 3.27 and 3.28 show the predicted torque-time and speed-time run-up curves for the fourth order model and the deep bar model respectively. The first peak of torque in Figure 3.27 is 500 Nm whereas the deep bar model's peak is 521 Nm. Both models show the instability at "steady state" which the motor exhibited in practice. (Note that the scale on the right hand side refers to the curve marked with X's). The rotor parameters used here with the traditional model are those for DC conditions. As shown in Section 3.8.1, using DC rotor parameters will result in a torque magnitude less than the correct value. The torque of the deep bar model (Figure 3.28) is thus assumed to be more accurate.

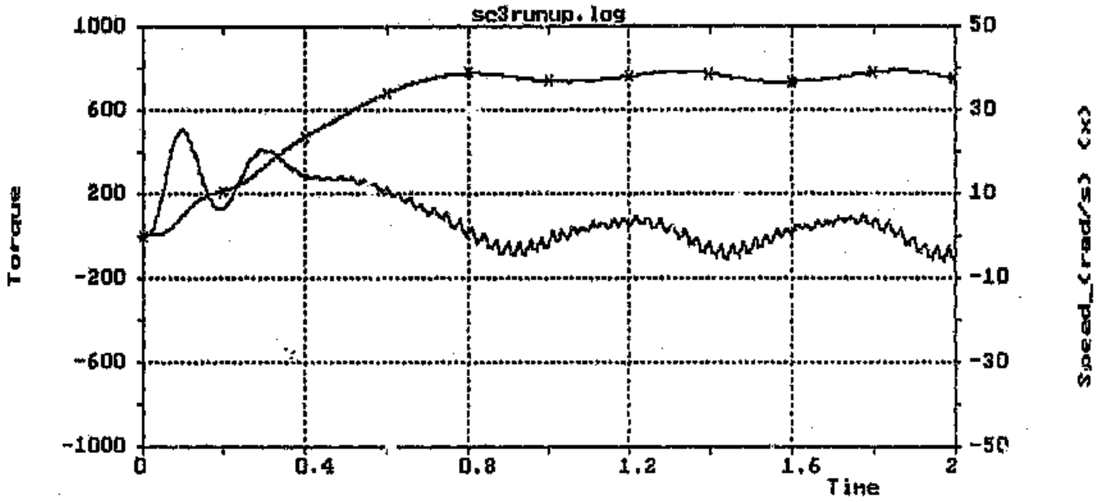

Figure 3.27 : Predicted Results Of 70 kW, 270 V, 8 Pole Induction Motor Supplied From A PWM Inverter Using Traditional Model

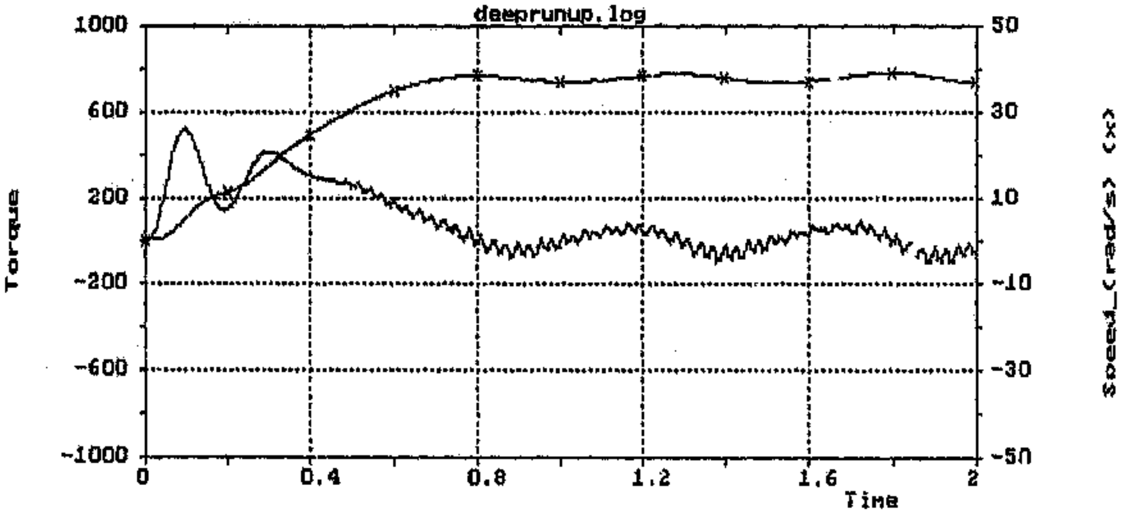

Figure 3.28 : Predicted Results Of 70 kW, 270 V, 8 Pole Induction Motor Supplied From A PWM Inverter Using Deep Bar Model

Figure 3.29 gives the current density in the top and bottom sections of the deep bar model for the first half second of the run-up. Current density as opposed to current has been used because the sections all have different areas. This graph clearly shows the harmonics which flow in the top section, distorting the waveform, and the lack of harmonics in the bottom section, resulting in a nearly smooth sinusoidal waveform. Figure 3.30 shows the conditions at steady state. It is seen that the current density in the top section (the smaller trace) has a high harmonic content whereas the current density of the bottom section contains harmonics with greatly reduced magnitudes. (Note that the scales of the two current densities are different, but the peak values are approximately equal).

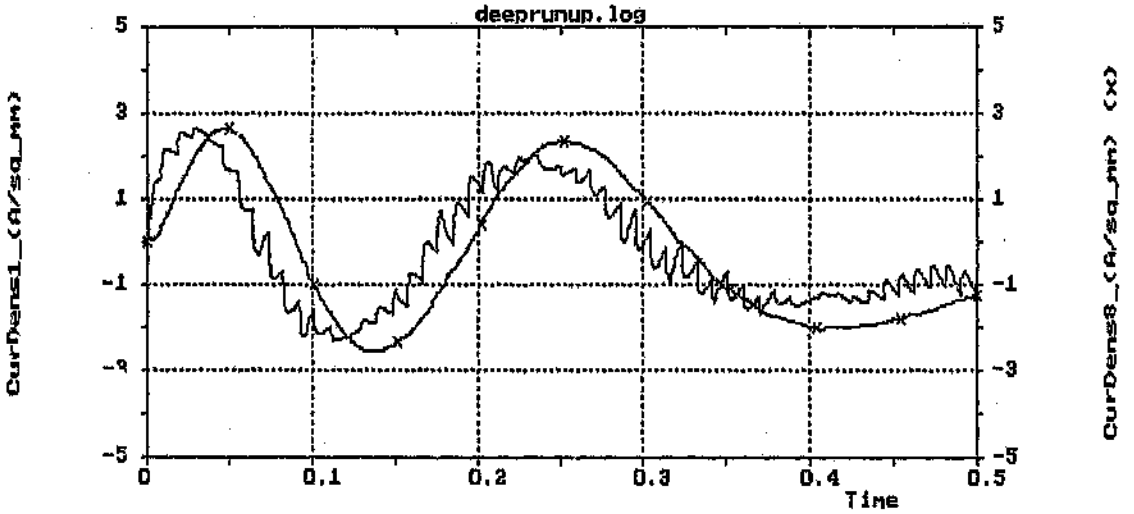

Figure 3.29 : Current Densities In Top And Bottom Sections Of Rotor Bar For Run-up Condition (70 kW, 270 V, 8 Pole Induction Motor Supplied From A PWM Inverter)

This case study has shown that the deep bar model can supply much useful information about the harmonics present in the rotor bars under both starting and steady-state conditions. Also, the magnitude of the currents flowing in different sections of the bar can be examined, which illustrates the deep bar phenomenon.

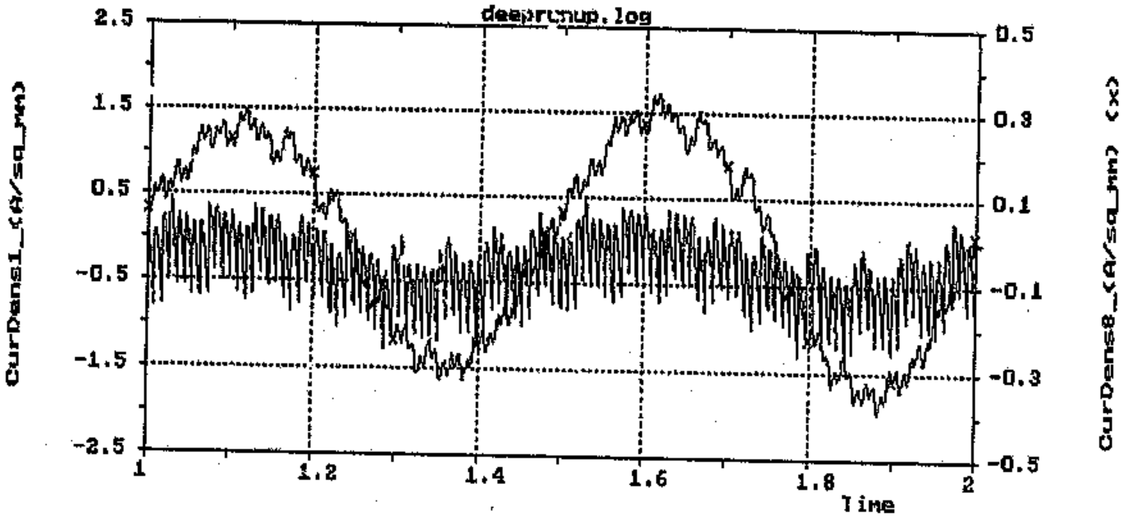

Figure 3.30 : Current Densities In Top And Bottom Sections Of Rotor Bar For Steady State Condition (70 kW, 270 V, 8 Pole Induction Motor Supplied From A PWM Inverter)

CHAPTER 4

DOUBLE CAGE MOTOR

Many induction motors are designed with two squirrel cages to ensure a high starting torque. The high resistance outer cage usually has a high starting torque and the pull-out torque occurs near or below zero speed. In contrast, the high reactance low resistance inner cage has a very low starting torque and a high pull-out torque which occurs near slip speed. The superposition of the two characteristics gives the typical double cage torque-speed curve of a high starting torque, a tendency for the torque to decrease as the speed increases and a pull-out torque which is often not as large as the starting torque.

This Chapter shows that the deep bar model developed in the previous Chapter can readily be adapted to simulate double cage motors. The method used and its implementation is given and a predicted torque-speed curve is compared with a measured curve for a particular motor.

4.1. Traditional Model

The standard sixth order double cage induction motor model is similar to the single cage model of equation (2.2), except that it has two sets of rotor equations. Thus the equations, given in an arbitrary reference frame are

$$[V] = [R]\cdot[I] + [L]\frac{d}{dt}[I] + [G]\cdot[I] \tag{4.1}$$

where

$$[V] = \begin{bmatrix} V_{sd} \\ V_{sq} \\ 0 \\ 0 \\ 0 \\ 0 \end{bmatrix} \tag{4.2}$$

$$[I] = \begin{bmatrix} I_{sd} \\ I_{sq} \\ I'_{rd\,i} \\ I'_{rq\,i} \\ I'_{rd\,o} \\ I'_{rq\,o} \end{bmatrix} \tag{4.3}$$

$$[R] = \begin{bmatrix} R_s & 0 & 0 & 0 & 0 & 0 \\ 0 & R_s & 0 & 0 & 0 & 0 \\ 0 & 0 & R'_{r\,i} & 0 & R'_e & 0 \\ 0 & 0 & 0 & R'_{r\,i} & 0 & R'_e \\ 0 & 0 & R'_e & 0 & R'_{r\,o} & 0 \\ 0 & 0 & 0 & R'_e & 0 & R'_{r\,o} \end{bmatrix} \tag{4.4}$$

$$[L]=\begin{bmatrix} L_s & 0 & M & 0 & M & 0 \\ 0 & L_s & 0 & M & 0 & M \\ M & 0 & L'_{r\,i} & 0 & M & 0 \\ 0 & M & 0 & L'_{r\,i} & 0 & M \\ M & 0 & M & 0 & L'_{r\,o} & 0 \\ 0 & M & 0 & M & 0 & L'_{r\,o} \end{bmatrix} \tag{4.5}$$

$$[G]=\begin{bmatrix} 0 & -\omega L_s & 0 & -\omega M & 0 & -\omega M \\ \omega L_s & 0 & \omega M & 0 & \omega M & 0 \\ 0 & -(\omega-\omega_r)M & 0 & (\omega-\omega_r)L'_{r\,i} & 0 & (\omega-\omega_r)M \\ (\omega-\omega_r)M & 0 & (\omega-\omega_r)L'_{r\,i} & 0 & (\omega-\omega_r)M & 0 \\ 0 & (\omega-\omega_r)M & 0 & (\omega-\omega_r)M & 0 & (\omega-\omega_r)L'_{r\,o} \\ (\omega-\omega_r)M & 0 & (\omega-\omega_r)M & 0 & (\omega-\omega_r)L'_{r\,o} & 0 \end{bmatrix} \tag{4.6}$$

Subscripts i refer to the inner cage and subscripts o refer to the outer cage. The electromagnetic torque is given by

$$\mathcal{T}_e = pM(I_{sq}\cdot I'_{rd\,i}+I_{sq}\cdot I'_{rd\,o}-I_{sd}\cdot I'_{rq\,i}-I_{sd}\cdot I'_{rq\,o}) \tag{4.7}$$

4.2. New Deep Bar Double Cage Model

4.2.1. Method and implementation

Using the same technique as that employed in Section 3.3, the rotor portion of the double cage model can be replaced by an equivalent lumped parameter circuit. Each bar is divided into a number of sections and the resistance and leakage inductance of each section is calculated using equations (3.1) and (3.2) respectively.

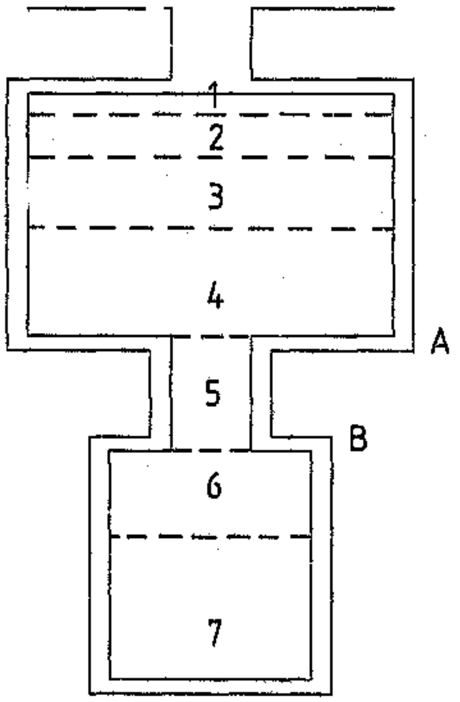

Figure 4.1 : Correct Method Of Dividing Double Cage Bar

The algorithm which calculates the depth of each section of bar arranges that the bottom-most section of the outer bar (section 4 in Figure 4.1) always coincides with line A which is the interface between the outer bar and the tongue. Similarly, the bottom-most section of the tongue (section 5) will always coincide with line B, the interface between the tongue and the inner bar. Thus the algorithm ensures that no section overlaps from the outer bar to the tongue or from the tongue to the inner bar, which is the case in Figure 4.2. If the tongue between the two cages is a leakage portion i.e. there is no bar in that portion of the slot, then that section will have a leakage inductance and no resistance. From the equivalent circuits of the lumped parameter models in Appendix C, the section which has no bar portion will have an infinite resistance and thus the series inductances may be combined, thereby reducing the number of sections (and states). The torque of this deep bar model is the same as that of equation (2.9). This method of combining the inductances and reducing the number of sections has been implemented in CASED. The results obtained are illustrated in the following example.

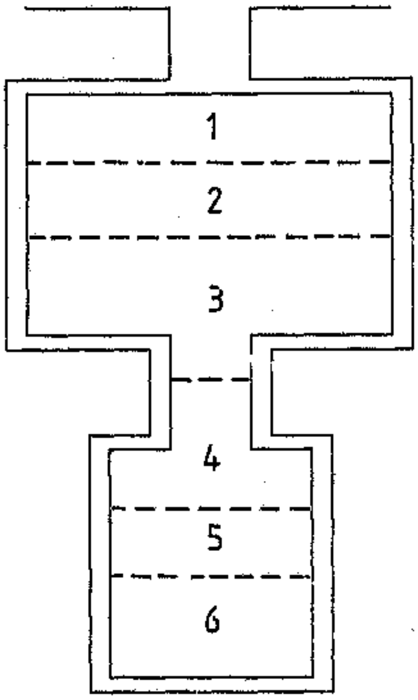

Figure 4.2 : **Incorrect Method Of Dividing Double Cage Bar**

4.2.2. Example

The induction motor used for this example is a 1850 kW, 6600 V, 3 phase, 50 Hz, 6 pole, double cage motor with outer bar dimensions of 19x19 mm, an inner cage 18 mm deep by 12.5 mm wide and a tongue portion 13.5 mm deep by 5 mm wide with no bar section present. The results are given for the unloaded motor being run at full speed in one direction, plugged and allowed to decelerate through zero speed and accelerate to full speed in the opposite direction. This then gives a steady state run-up curve of the motor.

The measured results are obtained using a DC tacho-generator which is hand held against the shaft of the machine. The tacho-generator output is filtered and recorded as the speed signal. This signal is also differentiated to give the shaft angular acceleration, which can be scaled in terms of the torque because the motor runs up against its own inertia. The motor is tested on reduced voltage to allow a longer run-up time, and the supply voltage is also monitored. It was observed that during the measured run-up, the voltage changed and thus the torque curve has been corrected for this volt drop.

(Note : Even though the measurements were taken at the reduced voltage of 1230 V, the measured curve shown has been scaled to full voltage by the voltage^2 method)

Figure 4.3 gives the measured torque-speed curve of the motor, from which the typical double cage characteristic can be seen. The predicted torque-speed curve of the motor using the traditional double cage model of equations (4.1) to (4.7) is given in Figure 4.4. The predicted "deep bar" curve, Figure 4.5, has been obtained using five sections of the improved Pi model, three sections for the outer bar, one section for the inner bar and one for the tongue portion. The fact that there is no bar in the tongue portion means that the simulation reduces the number of sections by one and thus the number of states by four. Both of the predicted curves have the measured torque-speed curve superimposed on them for comparative purposes.

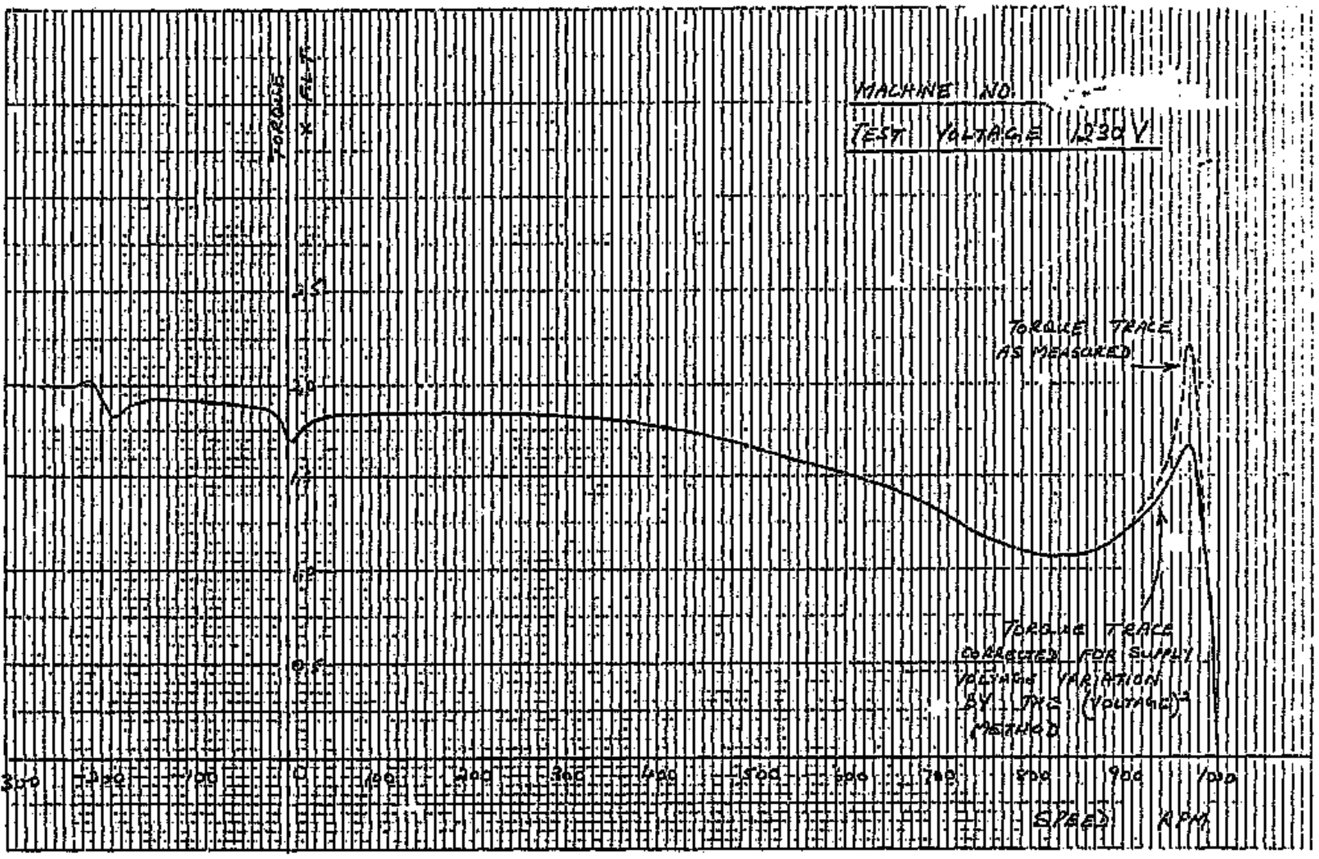

Figure 4.3 : Measured Torque-Speed Curve Of 1850 kW, 6600 V, 6 Pole Double Cage Motor

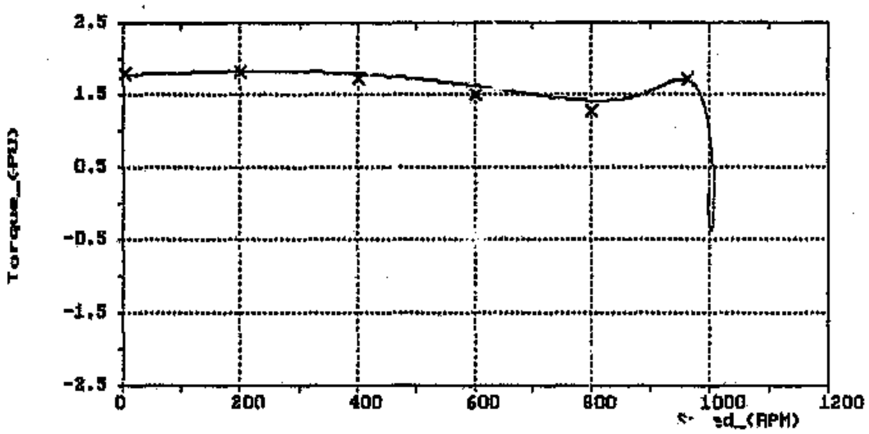

Figure 4.4 : **Predicted Torque-Speed Curve Of 1850 kW, 6600 V, 6 Pole Motor Using Traditional Double Cage Model (The X's Are The Measured Points Transcribed From The Measured Curve)**

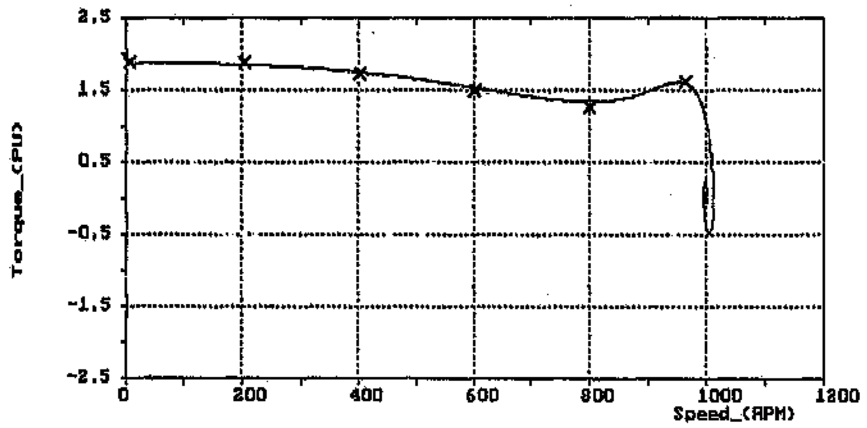

Figure 4.5 : **Predicted Torque-Speed Curve Of 1850 kW, 6600 V, 6 Pole Motor Using Deep Bar Double Cage Model (The X's Are The Measured Points Transcribed From The Measured Curve)**

There seems to be little difference between the two predicted curves, although the "deep bar" model comes closer to predicting the dip in torque prior to the pull-out torque. The similarity in these results can be attributed to the following :

1) The traditional double cage model is capable of producing results very similar to the measured values.

2) The "deep bar" model has only used three sections for the outer bar (i.e. for start-up) and one section for the inner bar, which may have introduced some inaccuracy into the prediction.

It can be seen that both the predicted curves show a slight overshoot in speed, which the measured curve does not display. This overshoot may have been introduced by using a value for the inertia which is slightly too small.

This Chapter has shown that the deep bar model developed in Chapter 3 can readily be applied to double cage motors, although the results show that the traditional model is capable of producing predictions which compare favourably with measured values.

CHAPTER 5

SATURATION

In induction motors, which generally have fairly narrow slot openings and small air gaps, the slot leakage flux which links the whole slot as well as the zigzag flux is forced through the small area of the tooth tip. Under transient conditions, when the current is high, the concentration of flux into a narrow portion of iron leads to saturation of the leakage flux paths. This saturation effectively reduces the leakage reactance, thus [illegible] the current and the corresponding torque.

This Chapter will review some of the work done by other researchers in this field and then describe the methods which have been implemented in CASED to account for this phenomenon. Finally the case study which was carried out in Chapter 3 is extended to show improved results when accounting for saturation.

5.1. Work Done By Other Researchers

Many research papers have been published on methods of accounting for saturation effects during starting, and more recently for taking these effects into account in simulations. These methods will now be reviewed.

Fuchs et al [33] use finite element methods to predict the flux fields during starting. Their calculation of the stator and rotor leakage reactances, like most other methods, is based on splitting each component into a saturable and an unsaturable portion. Mukherjee et al [38] use a finite element package which can accept non-linear curves for the magnetic material to calculate the leakage reactances.

Lipo and Consoli [26] and Keyhani and Tsai [36] show similar methods of accounting for saturation of the stator and rotor leakage inductances. Lipo and Consoli [26] apply a saturation factor to the saturable portion of the inductance which is defined as the ratio of the change in inductance due to saturation over the unsaturated inductance. These values are obtained from the measured voltage-flux characteristic. Keyhani and Tsai [36] obtain the saturation factor by defining the flux linkages as some function of the current, where the constants involved are estimated using a non-linear curve fitting program. These methods are unsuitable for the present application because both methods rely on measured data.

Chalmers and Dodgson [13] calculate a saturation factor based on the comparison of the leakage flux present with no saturation to that when saturated. Each unsaturated leakage flux is calculated and its path determined assuming no other fluxes are present. When the paths of all the fluxes are determined, decisions can then be made as to which path will saturate first. Once the saturation of this path has been accounted for, the next path to saturate is determined, and so on. Although this method has shown good correlation with measurement in the paper, it requires a knowledge of the magnitude of the flux in each path. Such information is not readily available from the simulation and would thus require extensive additional calculations.

Agarwal and Alger [7] have proposed a method of calculating a saturation factor for the tooth tip leakage flux of both the stator and rotor. The factor is based on the ratio of the current at which saturation occurs to the actual current in the stator or rotor. This method is readily adaptable to the present situation and is one of the methods that has been implemented.

5.2. Methods Implemented In CASED

Two methods of accounting for saturation of the leakage flux through the tooth tips have been implemented, both of which calculate a saturation factor σ. Both the stator and rotor leakage inductances are split into a saturable and an unsaturable portion such that

$$L_{ls} = \sigma_s L_{ls\,s} + L_{ls\,u} \tag{5.1}$$

$$L'_{lr} = \sigma_r L'_{lr\,s} + L'_{lr\,u} \tag{5.2}$$

where the unsaturable portion is made up of the end winding and the skew leakage inductances and the saturable portion is composed of the zigzag and slot leakage inductances.

5.2.1. The empirical method

The first method to be implemented makes use of an empirical curve for the saturation factor σ. It is a generalised solution of the saturation problem and has been used extensively and successfully in an induction motor design analysis program. The curve used to obtain the saturation factor is shown in Figure 5.1 where the variable amp wires per mm is defined as

$$AW/mm = \frac{C_s K_p S_s}{P_c \pi D_{is}} I \tag{5.3}$$

where

C_s = number of stator conductors per slot

K_p = stator coil pitch factor

S_s = number of stator slots

P_c = number of stator parallel circuits

D_{is} = stator inside diameter (mm)

I = either the stator or rotor current

This empirical method assumes that the width of the stator and rotor slot openings are the same, which is often erroneous in practice. The current ratio method accounts for the width of the stator and rotor slot openings being different. Thus the empirical method will not be as accurate as the second method because of its generalisation but is useful if complete stator slot details are unavailable. The current to be used in equation (5.3) is calculated from the two-axis currents for each of the stator and rotor as follows

$$I_s = \sqrt{I_{sd}^2 + I_{sq}^2} \tag{5.4}$$

$$I_r = \sqrt{I_{rd}^2 + I_{rq}^2} \tag{5.5}$$

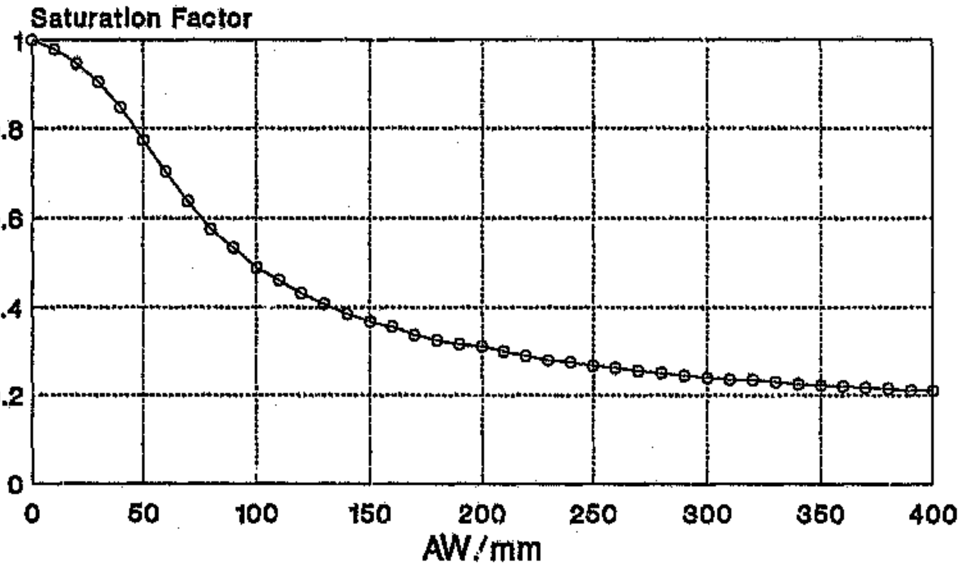

Figure 5.1 : Curve For Evaluation Of The Empirical Saturation Factor

5.2.2. The current ratio method

This method is based on that proposed by Agarwal and Alger [7], where the saturation factor σ is defined as

$$\sigma = \frac{I_{sat}}{I} \tag{5.6}$$

where

I_{sat} = the current at which saturation occurs

I = the actual stator or rotor current

Considering the stator winding, the peak leakage flux passing through the tooth tips of the stator slot is

$$\hat{\Phi}_t = \sqrt{2} I_{RMS} \mathcal{P}_t \tag{5.7}$$

where I_{RMS} is the total RMS current per stator slot and $\mathcal{P}_t$ is the sum of all the permeances of the flux passing through the tooth tip portion of the stator slot, i.e.

$$I_{RMS} = \frac{2qK_sN_1I_p}{S_s} \tag{5.8}$$

where

q = the number of phases

N_1 = number of stator turns in series per phase

I_p = the stator current per phase

If the flux in the stator tooth tips begins to saturate at a flux density of $B_{s\,sat}$, corresponding to an RMS slot current of $I_{RMS\,sat}$ then

$$\hat{\Phi}_t = B_{s\,sat} l_c d_t \tag{5.9}$$

where

d_t = the depth of the tooth tip section through which the saturating flux flows

Equating (5.7) and (5.9) and replacing I_{RMS} with $I_{RMS\,sat}$ gives

$$\sqrt{2} I_{RMS\,sat} \mu_0 l_c \lambda_t = B_{s\,sat} l_c d_t \tag{5.10}$$

where

$\mathcal{P}_t = \mu_0 l_c \lambda_t$

λ_t = the permeance coefficient per unit length of the tooth tip

$$I_{RMS\,sat} = \frac{B_{s\,sat} d_t}{\sqrt{2} \mu_0 \lambda_t} \tag{5.11}$$

From equation (5.8), the stator phase current at which saturation occurs, $I_{s\,sat}$, is given by

$$I_{s\,sat} = \frac{S_s I_{RMS\,sat}}{2qK_d N_1}$$

$$= \frac{S_s B_{s\,sat} d_t}{2qK_d N_1 \sqrt{2}\mu_0 \lambda_t} \tag{5.12}$$

so that the stator saturation factor is now

$$\sigma_s = \frac{I_{s\,sat}}{I_s} \tag{5.13}$$

Similarly for the rotor tooth tips, the saturation factor is

$$\sigma_r = \frac{I_{r\,sat}}{I_r} \tag{5.14}$$

where

$$I_{r\,sat} = \frac{S_r B_{r\,sat} d_t}{2qK_d N_1 \sqrt{2}\mu_0 \lambda_t} \tag{5.15}$$

and I_r = the rotor current defined by equation (5.5)

$B_{r\,sat}$ = the flux density at the tooth tips begin to saturate.

For both the stator and the rotor, the saturation factor is

$$\sigma = \frac{I_{sat}}{I} \tag{5.16}$$

except if $I < I_{sat}$ then $\sigma = 1.0$.

5.3. Case Study

The same 254 kW motor that was examined in Section 3.8.1 with deep bar effects is now considered with saturation included. Two simulations have been carried out, both using identical conditions to those of Section 3.8.1, except that the two methods of accounting for saturation have been included. The data used for both saturation methods was readily obtained from the motor manufacturer's design sheet.

For the amp wire method, from equation (5.3)

$$AW/mm = \frac{16 \times 0.978 \times 60}{1 \times \pi \times 379.1} I = 0.788 \times I \tag{5.17}$$

For the current ratio method, the saturable stator current is given by equation (5.12) as

$$\begin{aligned} I_{s\,sat} &= \frac{60 \times 1.3 \times 0.002}{2 \times 3 \times 0.957 \times 160 \times \sqrt{2} \times 4 \times \pi \times 10^{-7} (0.285 + 0.089)} \\ &= 255.47 \end{aligned} \tag{5.18}$$

and the corresponding saturable rotor current is

$$I_{r\,sat} = \frac{50 \times 1.3 \times 0.00254}{2 \times 3 \times 0.957 \times 160 \times \sqrt{2} \times 4 \times \pi \times 10^{-7}(0.464 + 0.8)} \tag{5.19}$$

$$= 80.00$$

so that the saturation factors are

$$\sigma_s = \frac{255.47}{I_s} \tag{5.20}$$

$$\sigma_r = \frac{80.00}{I_r} \tag{5.21}$$

This result of a saturable stator current which is larger than the corresponding saturable rotor current is expected if the slot shapes of the two portions are considered. The stator has a rectangular open slot 11.176 mm wide whereas the rotor has a T-shaped slot with a slot opening of 3.175 mm. Thus the stator tooth tip area is large and will only saturate at a large current. In contrast, the rotor tooth tip area is small and saturates at a much lower current.

This occurrence of the stator and rotor tooth tips saturating at different currents is not taken into account with the empirical method because the same value for equation (5.3), excluding the current, is used for both the stator and rotor. This can be seen in Figures 5.2 and 5.3 which give comparisons of the stator and rotor saturation factors for both methods.

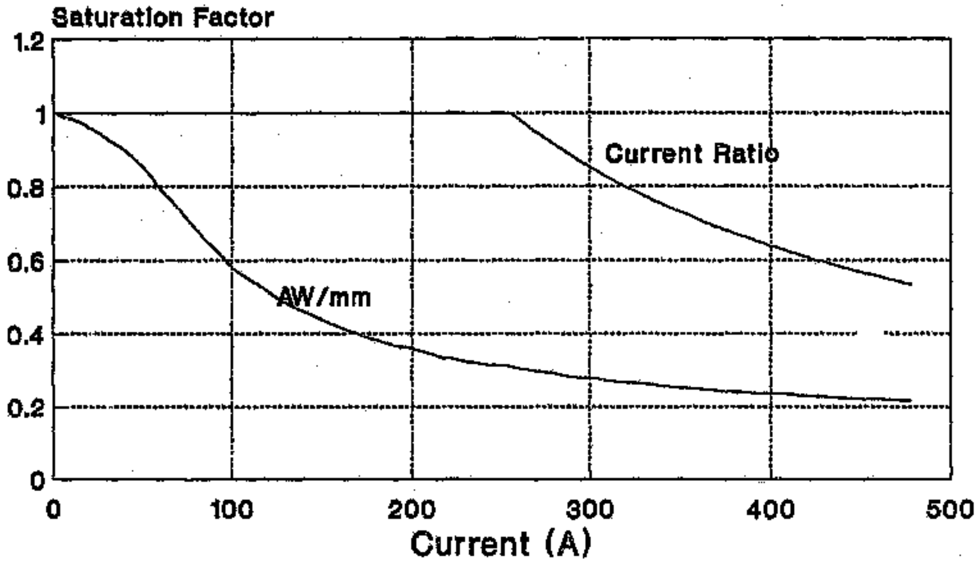

Figure 5.2 : Comparison Between The Stator Saturation Factor Obtained Using The Empirical Method And That Obtained Using The Current Ratio Method

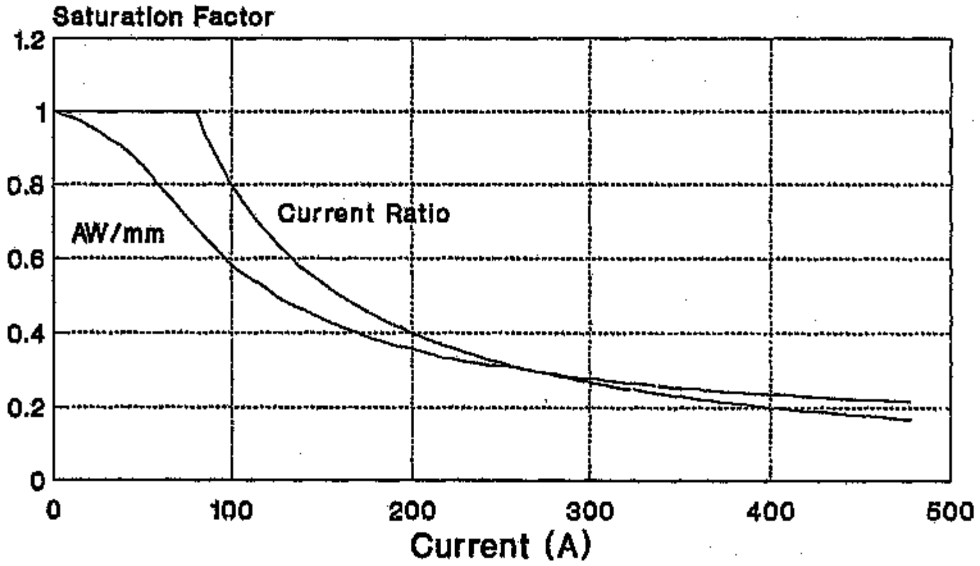

Figure 5.3 : Comparison Between The Rotor Saturation Factor Obtained Using The Empirical Method And That Obtained Using The Current Ratio Method

The ordinate on the graphs is the saturation factor σ and the abscissa is the current found in the stator or rotor. As discussed, the empirical (AW/mm) method is the same for both the stator and the rotor and the current ratio method shows the large difference between its two factors. The flat portion of the current ratio method at low currents represents the linear portion of the B-H curve, which the first method does not take into account.

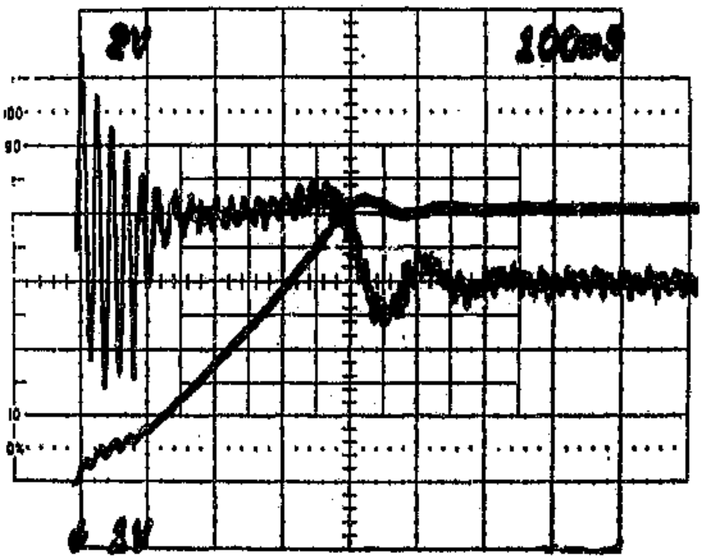

<u>Figure 5.4</u> : **Measured Torque And Speed Traces Of 254 kW, 3300 V, 4 Pole Squirrel Cage Induction Motor (Time = 100 ms/div, Torque = 1.65 PU/div, Speed = 0.25 PU/div)**

(Although the measured torque and speed results for this motor were given in Section 3.8.1, they are repeated here (Figure 5.4) for ease of comparison.) Figure 5.5 gives the predicted results for the simulation of the motor with the deep bar effect <u>and</u> the empirical method of saturation included. Figure 5.6 gives the corresponding predictions with the current ratio method of saturation used. In the case study of the deep bar effect, the predicted torque waveform compared well with the measured curve but the magnitude of the peak torques was lower than the measured value. Both Figures 5.5 and 5.6 show that the magnitude of the peak torques has increased now that saturation has also been accounted for and that the shape of the torque waveform is essentially the same. The predicted first peak of torque is 5.13 PU for the empirical method and 5.30 PU for the current ratio method. The value for the current ratio method compares well with the measured value of 5.28 PU. From Figures 5.2 and 5.3 it is seen that the difference between the saturation factor determined by the two methods is fairly large. However, the saturable portion of the leakage inductance only accounts for 10-20% of the total stator or rotor leakage inductance. Therefore the effect on the torque and current predictions is not very marked so the difference between the predicted results using either method is minimal in this case.

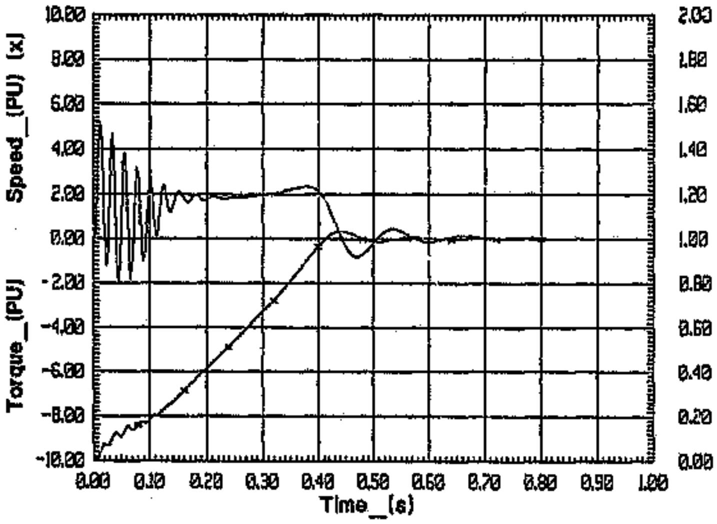

Figure 5.5 : **Predicted Torque And Speed Traces Of 254 kW, 3300 V, 4 Pole Squirrel Cage Induction Motor Using The Empirical Method Of Saturation**

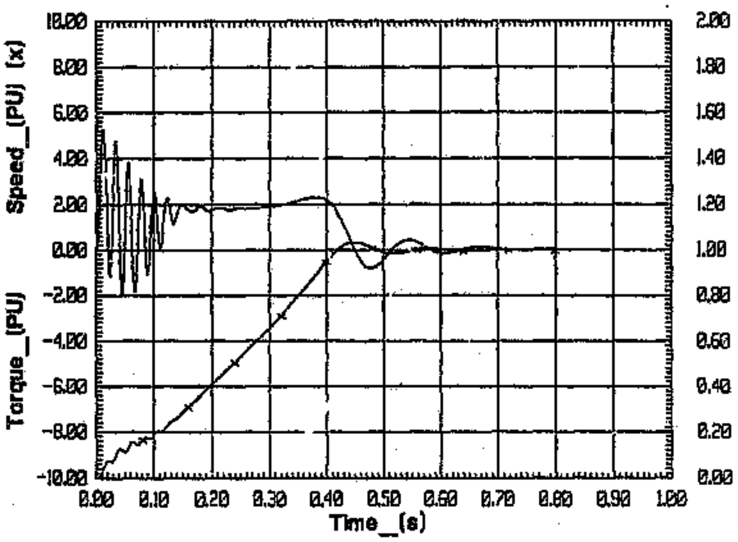

Figure 5.6 : **Predicted Torque And Speed Traces Of 254 kW, 3300 V, 4 Pole Squirrel Cage Induction Motor Using The Current Ratio Method Of Saturation**

This case study has shown that accounting for deep bar and saturation effects give torque and speed predictions which compare very favourably in all respects. Both methods of accounting for saturation are acceptable, but the current ratio method is more accurate because it allows for different saturating currents in the stator and the rotor. The empirical method has been generalised and is very useful if the stator slot shape is not fully known. This is so because only the rotor dimensions need be known to account for the deep bar effects.

CHAPTER 6

RESWITCHING TRANSIENTS

Reswitching transients occur when the supply to the motor is disconnected and then reconnected a short time later. Landy [17] has shown that the current and torque transients that result under these conditions can be many times their rated values depending on the phase of the motor induced voltage with respect to the supply voltage. This Chapter shows the development of the equations and initial conditions for the evaluation of reswitching transients for both the traditional model and the deep bar model of Chapter 3. An example is given which shows that the transient torque predicted by using the deep bar model is considerably larger than that predicted by using the traditional model.

6.1. Reswitching Using The Traditional Model

This model is derived using the basic equations (A.37) - (A.40) and applying certain boundary conditions. When the supply is disconnected from the motor, the stator currents are zero and thus

$$V_{sd} = M\frac{d}{dt}I'_{rd} - \omega M I'_{rq} \tag{6.1}$$

$$V_{sq} = M\frac{d}{dt}I'_{rq} - \omega M I'_{rd} \tag{6.2}$$

$$V_{rd} = 0 = R'_r I'_{rd} + L'_r \frac{d}{dt} I'_{rd} - (\omega - \omega_r) L'_r I'_{rq} \tag{6.3}$$

$$V_{rq} = 0 = R'_r I'_{rq} + L'_r \frac{d}{dt} I'_{rq} + (\omega - \omega_r) L'_r I'_{rd} \tag{6.4}$$

The d- and q-axis currents are proportional to the mmf's produced by them so that, just before disconnection of the supply,

$$\mathcal{F}_d \quad \propto \quad I_{sd-} + I'_{rd-} \tag{6.5}$$

$$\mathcal{F}_q \quad \propto \quad I_{sq-} + I'_{rq-} \tag{6.6}$$

and once the supply has been removed,

$$\mathcal{F}_d \quad \propto \quad I'_{rd+} \tag{6.7}$$

$$\mathcal{F}_q \quad \propto \quad I'_{rq+} \tag{6.8}$$

where the subscripts - and + refer to just before and just after the instant of switching. To maintain the balance of mmf over the instant of switching, the rotor current must adjust as follows

$$I'_{rd+} = I'_{rd-} + I_{sd-} \tag{6.9}$$

$$I'_{rq+} = I'_{rq-} + I_{sq-} \tag{6.10}$$

6.2. Reswitching Using The Deep Bar Model

As derived in Appendix C, the stator equations for the deep bar model are

$$V_{sd}=R_sI_{sd}+L_s\frac{d}{dt}I_{sd}+M\frac{d}{dt}I'_{rd}+\omega_rMI'_{rq}+\omega_rL_sI_{sq} \tag{6.11}$$

$$V_{sq}=R_sI_{sq}+L_s\frac{d}{dt}I_{sq}+M\frac{d}{dt}I'_{rq}-\omega_rMI'_{rd}-\omega_rL_sI_{sd} \tag{6.12}$$

The rotor equations for the first loop of any of the lumped parameter circuits have a similar format to equations (6.13) and (6.14)

$$V_{rd}=0=(R_0+R'_e)I'_{rd\,0}+L_0\frac{d}{dt}I'_{rd\,0}-R_1I'_{rd\,1}+M\frac{d}{dt}I'_{rd\,0}+M\frac{d}{dt}I_{sd} \tag{6.13}$$

$$V_{rq}=0=(R_0+R'_e)I'_{rq\,0}+L_0\frac{d}{dt}I'_{rq\,0}-R_1I'_{rq\,1}+M\frac{d}{dt}I'_{rq\,0}+M\frac{d}{dt}I_{sq} \tag{6.14}$$

where 0 refers to the first loop, 1 refers to the second loop and R'_e is the end-ring resistance. As for the previous Section, for disconnection of the supply, the stator currents are zero and thus

$$V_{sd} = M\frac{d}{dt}I'_{rd} + \omega_r M I'_{rq} \tag{6.15}$$

$$V_{sq} = M\frac{d}{dt}I'_{rq} + \omega_r M I'_{rd} \tag{6.16}$$

$$V_{rd} = 0 = (R_0 + R'_e)I'_{rd\,0} + L_0\frac{d}{dt}I'_{rd\,0} - R_1 I'_{rd\,1} + M\frac{d}{dt}I'_{rd\,0} \tag{6.17}$$

$$V_{rq} = 0 = (R_0 + R'_e)I'_{rq\,0} + L_0\frac{d}{dt}I'_{rq\,0} - R_1 I'_{rq\,1} + M\frac{d}{dt}I'_{rq\,0} \tag{6.18}$$

The boundary conditions for the currents to maintain the balance of mmf over the interval of switching are

$$I'_{rd\,0_+} = I'_{rd\,0_-} + I_{sd_-} \tag{6.19}$$

$$I'_{rq\,0_+} = I'_{rq\,0_-} + I_{sq_-} \tag{6.20}$$

The application of these models is well illustrated by the following example.

6.3. Example

The 254 kW induction motor of Section 3.8.1 has been used for this comparative example. For the traditional model, the DC (running) values of rotor resistance and leakage inductance have been used. The deep bar model is the same as that in Section

3.8.1, i.e. the improved Pi model with the bar divided into four sections. For both cases, the motor was run up to slip speed so that steady-state conditions were achieved. These steady-state conditions were then used as initial conditions for the rest of the work. Also, the friction and inertia used here are larger than those used in Section 3.8.1, so that the simulation is that of a motor operated at full load.

Figure 6.1 shows the torque and the speed trace of the motor, predicted by the traditional model, with the supply disconnected at 0.1 seconds for 8 cycles (0.16 seconds) and then being re-made. Figure 6.2 shows the same conditions predicted using the deep bar model. The traditional model was simulated using a rotor fixed reference frame so that the current waveforms can easily be compared to those of the deep bar model.

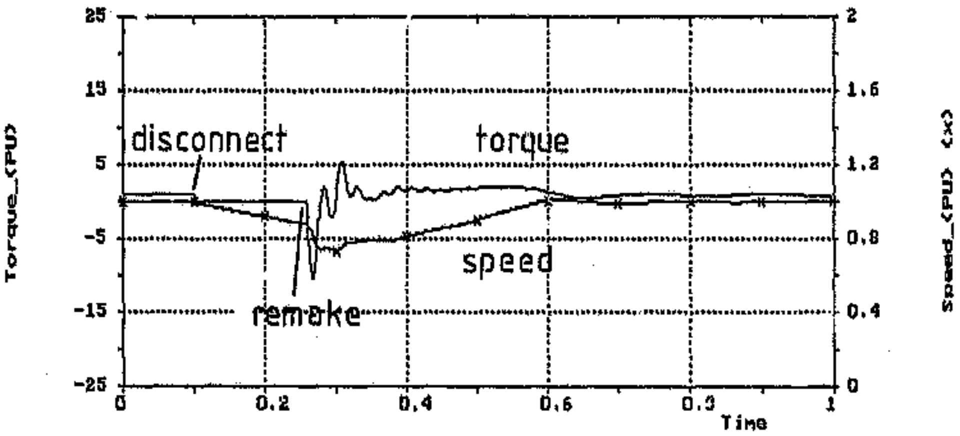

Figure 6.1 : Predicted Results Of 254 kW, 3300 V, 4 Pole Induction Motor Using The Traditional Model. The Supply Is Disconnected At 0.1 Seconds For 8 Cycles (0.16 Seconds) And Then Re-made

For both cases, the graphs show zero developed electromagnetic torque while the supply is disconnected. This is expected because equation (2.9) shows that the torque is dependent on both the d- and q-axis stator currents. Both graphs also show a negative reswitching

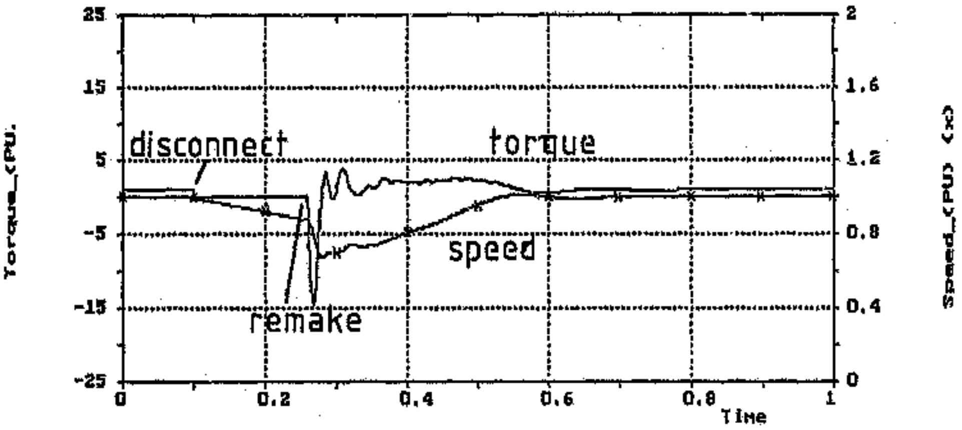

Figure 6.2 : **Predicted Results Of 254 kW, 3300 V, 4 Pole Induction Motor Using The Deep Bar Model. The Supply Is Disconnected At 0.1 Seconds For 8 Cycles (0.16 Seconds) And Then Re-made**

torque transient many times larger than the rated torque, which is as predicted by Landy [17] and de Mello and Walsh [8]. The deep bar model predicts the peak at -14 PU whereas the traditional model predicts -10 PU. This difference comes from the transient currents that occur under reswitching conditions, which the deep bar model predicts more accurately. Also, it should be noted that during the off period the motor speed has dropped to 0.68 PU at the instant when the supply is reconnected. For the traditional model, the rotor parameters are no longer valid because the rotor frequency has increased from nearly zero to 16 Hz. Thus, at the instant when the supply is reconnected, the traditional model will be inaccurate and the predicted negative torque will not be as large as the torque predicted by the deep bar model.

Figures 6.3 and 6.4 show the stator currents and Figures 6.5 and 6.6 show the rotor currents of the traditional model for the condition of Figure 6.1. Figures 6.7, 6.8, 6.9

and 6.10 show the corresponding stator and rotor currents for the deep bar model. It should be noted that the magnitude of the current transients predicted using the deep bar model are significantly larger than those predicted by using the traditional model.

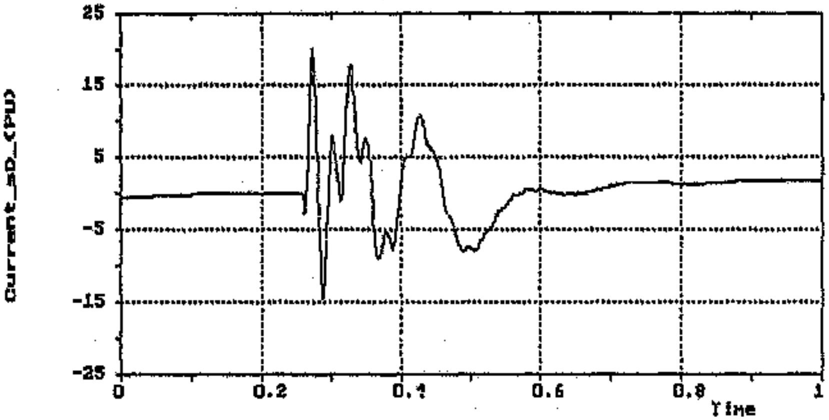

Figure 6.3 : Predicted Stator d-axis Current Of 254 kW, 3300 V, 4 Pole Induction Motor Using The Traditional Model. The Supply Is Disconnected At 0.1 Seconds For 8 Cycles (0.16 Seconds) And Then Re-made

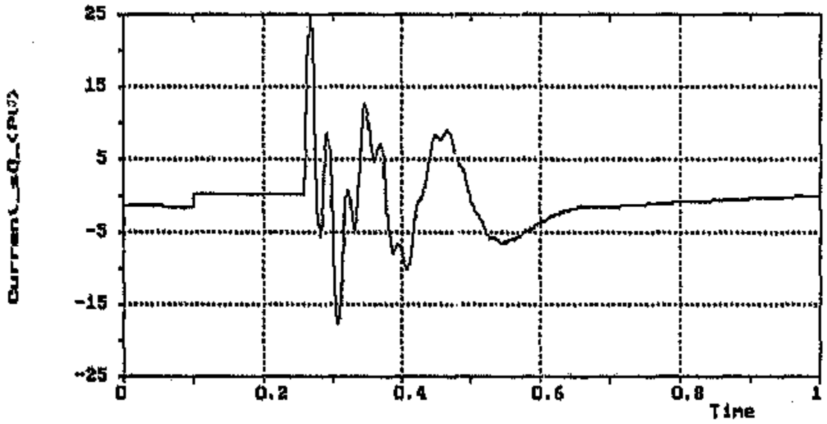

Figure 6.4 : Predicted Stator q-axis Current Of 254 kW, 3300 V, 4 Pole Induction Motor Using The Traditional Model. The Supply Is Disconnected At 0.1 Seconds For 8 Cycles (0.16 Seconds) And Then Re-made

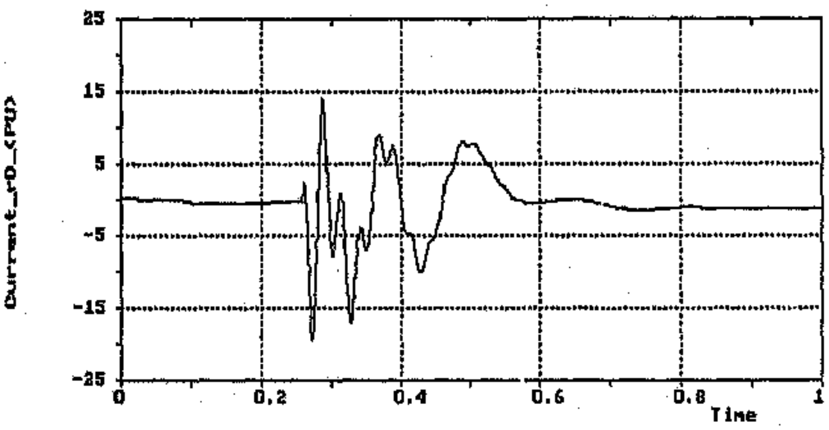

Figure 6.5 : **Predicted Rotor d-axis Current Of 254 kW, 3300 V, 4 Pole Induction Motor Using The Traditional Model. The Supply Is Disconnected At 0.1 Seconds For 8 Cycles (0.16 Seconds) And Then Re-made**

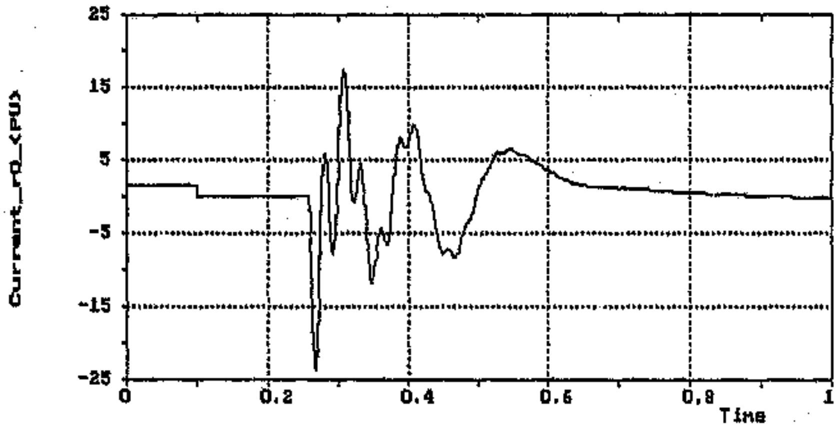

Figure 6.6 : **Predicted Rotor q-axis Current Of 254 kW, 3300 V, 4 Pole Induction Motor Using The Traditional Model. The Supply Is Disconnected At 0.1 Seconds For 8 Cycles (0.16 Seconds) And Then Re-made**

NOTE : Equations (6.9) and (6.10) or (6.17) and (6.18) suggest that, at the instant that the supply is disconnected, the rotor current will usually increase because of the stator current contribution. Here, for both the traditional and the deep bar model, the rotor current seems to drop to zero. This is actually not the case, but the large scale of the rest of the graph hides its value during the off period. The fact that the rotor current does not increase is attributed to the phase of the stator and rotor currents at that particular instant.

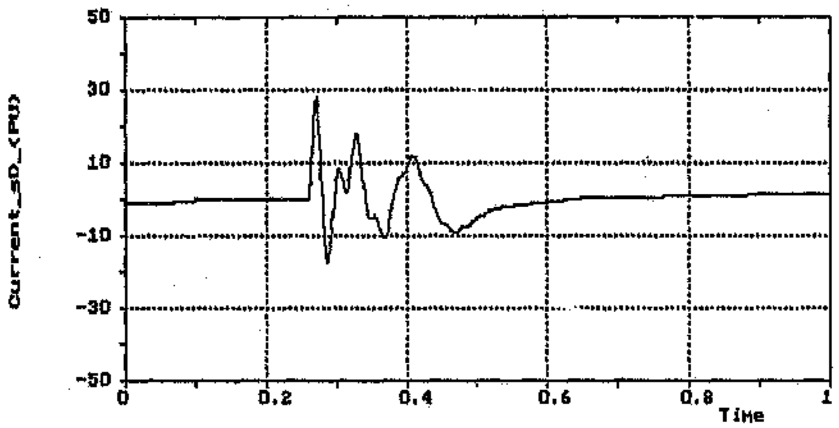

Figure 6.7 : Predicted Stator d-axis Currents Of 254 kW, 3300 V, 4 Pole Induction Motor Using The Deep Bar Model. The Supply Is Disconnected At 0.1 Seconds For 8 Cycles (0.16 Seconds) And Then Re-made

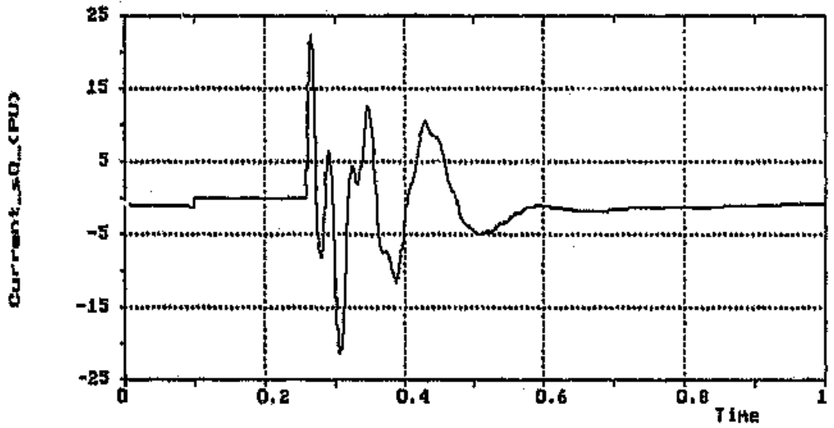

Figure 6.8 . Predicted Stator q-axis Currents Of 254 kW, 3300 V, 4 Pole Induction Motor Using The Deep Bar Model. The Supply Is Disconnected At 0.1 Seconds For 8 Cycles (0.16 Seconds) And Then Re-made

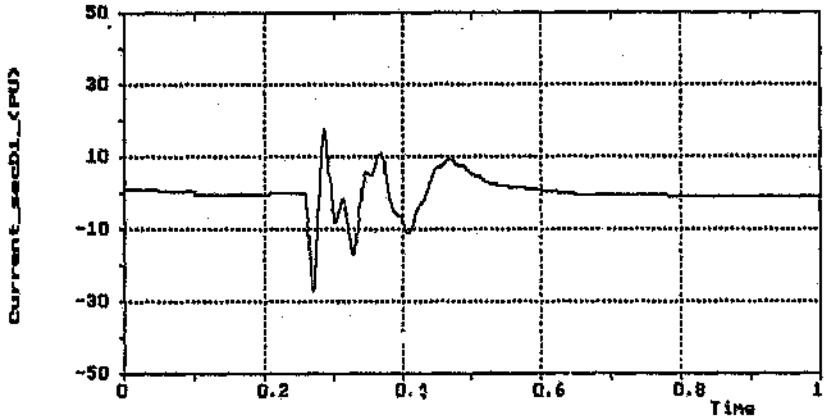

<u>Figure 6.9</u> : **Predicted Rotor d-axis Currents Of 254 kW, 3300 V, 4 Pole Induction Motor Using The Deep Bar Model. The Supply Is Disconnected At 0.1 Seconds For 8 Cycles (0.16 Seconds) And Then Re-made**

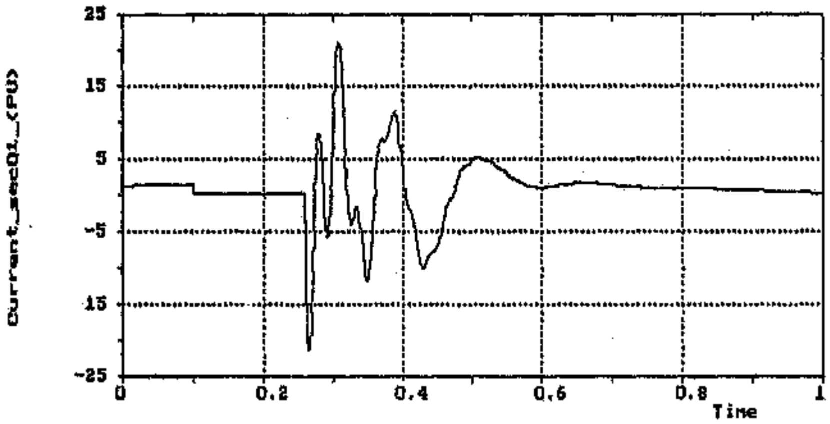

<u>Figure 6.10</u> : **Predicted Rotor q-axis Currents Of 254 kW, 3300 V, 4 Pole Induction Motor Using The Deep Bar Model. The Supply Is Disconnected At 0.1 Seconds For 8 Cycles (0.16 Seconds) And Then Re-made**

This example has shown that the deep bar model is capable of being used for reswitching transients. It accounts for the switching transient currents and the frequency effects due to the motor slowing down, better than does the traditional model. Therefore improved predictions of transient torques are obtained which are required for the mechanical analysis of the reswitching effects.

The importance of being able to predict reswitching transients was highlighted when a large industrial motor failed (note that it is not the one given in the example in this Chapter). The motor had been in service for some time prior to its failure. It was found that several rotor bars had broken and that the key on the shaft had been distorted by several millimetres. The distortion of the key indicated that the motor had been subjected to severe negative torques during operation. Analysis revealed that the supply to the motor was occasionally lost and thus the motor was being subjected to reswitching transients. Simulating this condition could have suggested the minimum amount of time to wait, once the supply has been disconnected, before reswitching the supply.

CHAPTER 7

CONCLUSIONS

The first objective of this work has been to develop an accurate induction motor model which can be used for variable speed drive system simulations. The model must be able to account for deep bar effects and include saturation of the tooth tip leakage flux. From the curves given in the examples of Chapters 3 and 5, the predicted results using this new model compare very favourably with the measured results. Therefore it is clear that this objective has been realised.

The other objective has been to implement all these models in the computer package CASED. This entailed writing the CREATE program referred to in Chapter 2, which forms the state space models of the system. The models are then written to files in a format suitable for use by the simulation program.

The development of a deep bar model is given in Chapter 3. Although the analytical solution to the deep bar differential equations, as given by Alger [14] is accurate, it is unsuitable for transient predictions because knowledge of the frequency content of the waveform is unavailable. A lumped parameter circuit has thus been used to account for the non-linear current distribution in the rotor bar, by having many sections whose distribution is linear.

Four circuits were compared with the analytical solution, in terms of their accuracy at different frequencies across the typical expected frequency spectrum. Section 3.5 shows that, at higher frequencies, the circuits only begin to have acceptable accuracies when a large number of sections are used. A large number of sections is undesirable because the length of time required for simulation is large. Thus a novel algorithm was developed which divides the rotor bar unequally along its depth, having smaller sections at the top where the current distribution is highly non-linear and larger sections at the bottom where the distribution is more linear. The analysis shows that different circuits and even different number of sections used requires slightly different constants in the algorithm. The results shown in Section 3.6 indicate that improvements in accuracy of up to thirty times at certain frequencies can be obtained by using this algorithm. For each of the models, the larger the number of sections used, the smaller the error will be. However the improved Pi model achieves this negligible error across a wide frequency range using fewer sections than the other models. The improved Pi model is thus the most accurate model.

Although it was beyond the scope of this project, it would be interesting to investigate whether there is a mathematical expression which could describe the error of the models as a function of *num*. This would then mean that the optimum value of *num* could be obtained analytically instead of graphically.

This method of accounting for deep bar effects is dependent on the shape of the bar, and thus numerous standard bar shapes have been implemented in CASED. Also included is a method of entering the depth and width of each section, so that almost any uncommon bar shape may also be simulated. As an extension of this routine, a unique method of simulating double cage motors using the deep bar model has been produced. Verification of the suitability of this algorithm to double cage machines is very aptly demonstrated by the good agreement achieved between the measured and predicted torque speed curves shown in Chapter 4.

The aim of this work has been to use a saturation factor which does not require testing of the motor. Thus two methods have been implemented for saturation of the stator and rotor tooth tip leakage flux. The first method uses an empirical factor which is a generalised solution of the saturation problem. The second method, based on the work by Agarwal and Alger [7], uses the current at which saturation of the leakage path occurs, which is obtained from the permeances of that path. That current is then compared to the actual current in the motor to determine the saturation factor. The case study of Chapter 5 shows that correlation between measured and predicted torque is very good when both the deep bar effect and saturation are accounted for.

It must be noted here that for all the examples, only torque measurements have been compared while the predicted currents have played a lesser role in the discussions. Only the torque was measured and it has been assumed for the purposes of this work that if the predicted torque compares well with the measured torque, then the predicted currents will also be accurate. This assumption is reasonable because the torque is calculated using the two stator and two rotor currents (see equation (2.9)). Thus if the predicted torque is correct, the currents giving the torque must be correct.

As an example of one of the applications of this deep bar model, reswitching transients are examined in Chapter 6. It is shown that the standard equations of a motor which has its supply disconnected for a certain period of time and then reconnected, can be applied to the deep bar model. Depending on the inertia of the load and the duration of disconnection, the speed of the motor can drop to half speed or even lower. The traditional model has rotor parameters which are then not correct for the frequency of the currents present in the rotor. Thus the deep bar model applied to reswitching transients predicts higher transient torques than would be predicted with the traditional model.

It must be emphasised that the case studies used for verification of the models are large induction motors used in industry. The motor used for the deep bar model and for saturation is a 254 kW induction motor and the double cage model was verified with a 1850 kW motor.

CASED has already been successfully used by undergraduate students of the Department of Electrical Engineering at the University. The modularity of the package has also been used advantageously by other students being able to add their own controllers and permanent magnet motor models. It is hoped that the package will be used by the industry for variable speed drive system simulations and ordinary sinusoidal motor simulations. Further, the author hopes that the accurate models developed will allow designers to readily predict with confidence the performance of a system prior to its manufacture.

applied to the deep bar model. Depending on the inertia of the load and the duration of disconnection, the speed of the motor can drop to half speed or even lower. The traditional model has rotor parameters which are then not correct for the frequency of the currents present in the rotor. Thus the deep bar model applied to reswitching transients predicts higher transient torques than would be predicted with the traditional model.

It must be emphasised that the case studies used for verification of the models are large induction motors used in industry. The motor used for the deep bar model and for saturation is a 254 kW induction motor and the double cage model was verified with a 1850 kW motor.

CASED has already been successfully used by undergraduate students of the Department of Electrical Engineering at the University. The modularity of the package has also been used advantageously by other students being able to add their own controllers and permanent magnet motor models. It is hoped that the package will be used by the industry for variable speed drive system simulations and ordinary sinusoidal motor simulations. Further, the author hopes that the accurate models developed will allow designers to readily predict with confidence the performance of a system prior to its manufacture.

APPENDIX A

Derivation Of Two-Axis Differential Equations Of Induction Motor

This appendix shows the transformation from the three phase stationary stator and the three phase rotating rotor to two sets of two phase windings, rotating at any arbitrary speed.

The conversion of any three phase winding to an equivalent two phase winding rotating at some arbitrary speed involves first passively transforming the three phase 120° winding (a,b,c) to a "two" phase [illegible] winding (α, β, γ) and then actively transforming the (α, β, γ) winding to a (d,q,γ) frame of reference rotating at ω_1 electrical radians/second.

Transformation between three phase (a,b,c) and two phase (α, β, γ) windings

Consider the balanced three phase winding and its corresponding orthogonal α, β axes, shown in Figure A.1, where the a-axis and the α-axis are co-incident.

By resolving the instantaneous mmf's set up by the a,b,c phase windings along the α, β axes, the following equations are obtained :

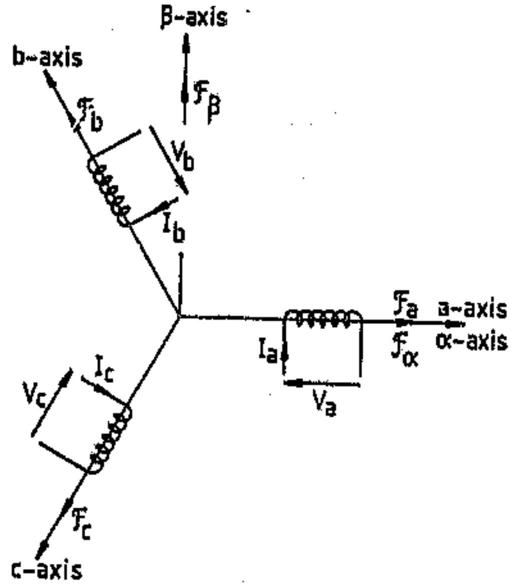

Figure A.1 : Three Phase And Two Phase Windings

$$\mathcal{F}_\alpha = \mathcal{F}_a + \mathcal{F}_b \cos(120°) + \mathcal{F}_c \cos(-120°)$$

$$\mathcal{F}_\beta = \mathcal{F}_b \sin(120°) + \mathcal{F}_c \sin(-120°) \tag{A.1}$$

or in matrix form :

$$\begin{bmatrix} \mathcal{F}_\alpha \\ \mathcal{F}_\beta \end{bmatrix} = \begin{bmatrix} 1 & -\frac{1}{2} & -\frac{1}{2} \\ 0 & \frac{\sqrt{3}}{2} & -\frac{\sqrt{3}}{2} \end{bmatrix} \cdot \begin{bmatrix} \mathcal{F}_a \\ \mathcal{F}_b \\ \mathcal{F}_c \end{bmatrix} \tag{A.2}$$

Equation (A.2) is acceptable in its present form, but to obtain $\mathcal{F}_{a,b,c}$ in terms of $\mathcal{F}_{\alpha,\beta}$ requires inverting the two by three matrix, which cannot be done in its present form. Thus an additional γ axis is added which is normal to both the α and β axes. Then

$$\begin{bmatrix} \mathcal{F}_\alpha \\ \mathcal{F}_\beta \\ \mathcal{F}_\gamma \end{bmatrix} = \begin{bmatrix} 1 & -\frac{1}{2} & -\frac{1}{2} \\ 0 & \frac{\sqrt{3}}{2} & -\frac{\sqrt{3}}{2} \\ \frac{1}{\sqrt{2}} & \frac{1}{\sqrt{2}} & \frac{1}{\sqrt{2}} \end{bmatrix} . \begin{bmatrix} \mathcal{F}_a \\ \mathcal{F}_b \\ \mathcal{F}_c \end{bmatrix} \tag{A.3}$$

or

$$[\mathcal{F}_{\alpha,\beta,\gamma}] = [A].[\mathcal{F}_{a,b,c}] \tag{A.4}$$

and

$$[\mathcal{F}_{a,b,c}] = [A]^{-1}.[\mathcal{F}_{\alpha,\beta,\gamma}] \tag{A.5}$$

where the values $\frac{1}{\sqrt{2}}$ have been chosen so that the inversion of $[A]$ reduces to the transposition of $[A]$, and for balanced conditions

$$\mathcal{F}_\gamma = \frac{1}{\sqrt{2}}(\mathcal{F}_a + \mathcal{F}_b + \mathcal{F}_c) = 0 \tag{A.6}$$

Thus

$$[A] = \sqrt{\frac{3}{2}}\sqrt{\frac{2}{3}} \begin{bmatrix} 1 & -\frac{1}{2} & -\frac{1}{2} \\ 0 & \frac{\sqrt{3}}{2} & -\frac{\sqrt{3}}{2} \\ \frac{1}{\sqrt{2}} & \frac{1}{\sqrt{2}} & \frac{1}{\sqrt{2}} \end{bmatrix} = \sqrt{\frac{3}{2}}\ [B] \tag{A.7}$$

$$[A]^{-1} = \sqrt{\frac{2}{3}}\sqrt{\frac{3}{2}} \begin{bmatrix} 1 & 0 & \frac{1}{\sqrt{2}} \\ -\frac{1}{2} & \frac{\sqrt{3}}{2} & \frac{1}{\sqrt{2}} \\ -\frac{1}{2} & -\frac{\sqrt{3}}{2} & \frac{1}{\sqrt{2}} \end{bmatrix} = \sqrt{\frac{2}{3}}\ [B]^T \tag{A.8}$$

i.e.

$$[B]^{-1} = [B]^T \tag{A.9}$$

and thus

$$[\mathcal{F}_{\alpha,\beta,\gamma}] = \sqrt{\frac{3}{2}}\ [B]\,[\mathcal{F}_{a,b,c}] \tag{A.10}$$

$$[\mathcal{F}_{a,b,c}] = \sqrt{\frac{2}{3}}\ [B]^T[\mathcal{F}_{\alpha,\beta,\gamma}] \tag{A.11}$$

Transformation between two phase (α, β, γ) and two phase (d,q,γ) windings

Consider two sets of axes, where the $\alpha-\beta$ axis is rotating at a speed ω_2 electrical radians/second and the d-q axis is rotating at some arbitrary speed ω_1 electrical radians/second. Initially the a-axis, α-axis and d-axis are all coincident. After some time t the situation is as shown in Figure A.2.

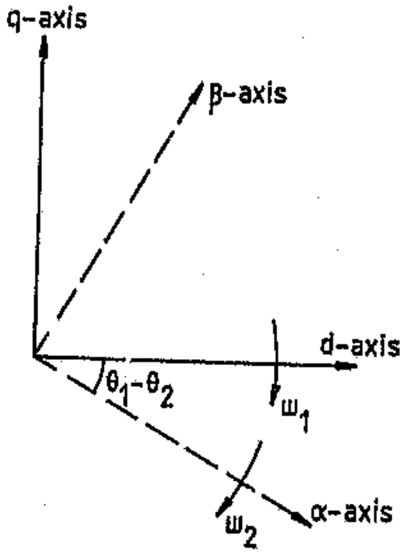

Figure A.2 : $\alpha-\beta$ And d-q Axes

At this instant the mmf relationships are

$$\mathcal{F}_d = \mathcal{F}_\alpha \cos(\theta_1 - \theta_2) + \mathcal{F}_\beta \sin(\theta_1 - \theta_2)$$

$$\mathcal{F}_q = -\mathcal{F}_\alpha \sin(\theta_1 - \theta_2) + \mathcal{F}_\beta \cos(\theta_1 - \theta_2)$$

$$\mathcal{F}_\gamma = \mathcal{F}_\gamma \tag{A.12}$$

or in matrix form

$$\begin{bmatrix} \mathcal{F}_d \\ \mathcal{F}_q \\ \mathcal{F}_\gamma \end{bmatrix} = \begin{bmatrix} \cos(\theta_1 - \theta_2) & \sin(\theta_1 - \theta_2) & 0 \\ -\sin(\theta_1 - \theta_2) & \cos(\theta_1 - \theta_2) & 0 \\ 0 & 0 & 1 \end{bmatrix} \begin{bmatrix} \mathcal{F}_\alpha \\ \mathcal{F}_\beta \\ \mathcal{F}_\gamma \end{bmatrix} \tag{A.13}$$

and the inverse is

$$\begin{bmatrix} \mathcal{F}_\alpha \\ \mathcal{F}_\beta \\ \mathcal{F}_\gamma \end{bmatrix} = \begin{bmatrix} \cos(\theta_1 - \theta_2) & -\sin(\theta_1 - \theta_2) & 0 \\ \sin(\theta_1 - \theta_2) & \cos(\theta_1 - \theta_2) & 0 \\ 0 & 0 & 1 \end{bmatrix} \begin{bmatrix} \mathcal{F}_a \\ \mathcal{F}_b \\ \mathcal{F}_\gamma \end{bmatrix} \tag{A.14}$$

$$[\mathcal{F}_{d,q,\gamma}] = [S]\,[\mathcal{F}_{\alpha,\beta,\gamma}] \tag{A.15}$$

$$[\mathcal{F}_{\alpha,\beta,\gamma}] = [S]^T\,[\mathcal{F}_{d,q,\gamma}] \tag{A.16}$$

where

$$[S] = \begin{bmatrix} \cos(\theta_1 - \theta_2) & \sin(\theta_1 - \theta_2) & 0 \\ -\sin(\theta_1 - \theta_2) & \cos(\theta_1 - \theta_2) & 0 \\ 0 & 0 & 1 \end{bmatrix} \tag{A.17}$$

To obtain the transformations between $\mathcal{F}_{a,b,c}$ and $\mathcal{F}_{d,q,\gamma}$, equations (A.10) and (A.11) are combined with (A.15) and (A.16) respectively, so that

$$[\mathcal{F}_{a,b,c}] = \sqrt{\frac{2}{3}}\ [B]^T [\mathcal{F}_{\alpha,\beta,\gamma}]$$

$$= \sqrt{\frac{2}{3}}\ [B]^T [S]^T [\mathcal{F}_{d,q,\gamma}] \tag{A.18}$$

$$[\mathcal{F}_{d,q,\gamma}] = [S]\ [\mathcal{F}_{\alpha,\beta,\gamma}]$$

$$= [S]\sqrt{\frac{3}{2}}\ [B]\ [\mathcal{F}_{a,b,c}] \tag{A.19}$$

Now

$$[C] = [S].[B]$$

$$= \sqrt{\frac{2}{3}}\begin{bmatrix} \cos(\theta_1-\theta_2) & \cos(\theta_1-\theta_2-120°) & \cos(\theta_1-\theta_2+120°) \\ -\sin(\theta_1-\theta_2) & -\sin(\theta_1-\theta_2-120°) & -\sin(\theta_1-\theta_2+120°) \\ \frac{1}{\sqrt{2}} & \frac{1}{\sqrt{2}} & \frac{1}{\sqrt{2}} \end{bmatrix} \tag{A.20}$$

and

$$[C]^T = [B]^T.[S]^T$$

$$= \sqrt{\frac{2}{3}}\begin{bmatrix} \cos(\theta_1-\theta_2) & -\sin(\theta_1-\theta_2) & \frac{1}{\sqrt{2}} \\ \cos(\theta_1-\theta_2-120°) & -\sin(\theta_1-\theta_2-120°) & \frac{1}{\sqrt{2}} \\ \cos(\theta_1-\theta_2+120°) & -\sin(\theta_1-\theta_2+120°) & \frac{1}{\sqrt{2}} \end{bmatrix}$$

(A.21)

Thus

$$[\mathcal{F}_{d,q,\gamma}] = \sqrt{\frac{3}{2}}\ [C]\,[\mathcal{F}_{a,b,c}] \tag{A.22}$$

$$[\mathcal{F}_{a,b,c}] = \sqrt{\frac{2}{3}}\ [C]^T[\mathcal{F}_{d,q,\gamma}] \tag{A.23}$$

Stator transformations

The stator voltage equations can be expressed as

$$\begin{bmatrix} V_{s1} \\ V_{s2} \\ V_{s3} \end{bmatrix} = R_s \begin{bmatrix} I_{s1} \\ I_{s2} \\ I_{s3} \end{bmatrix} + \frac{d}{dt} \begin{bmatrix} \Psi_{s1} \\ \Psi_{s2} \\ \Psi_{s3} \end{bmatrix} \tag{A.24}$$

where s1,s2,s3 are the stator a,b,c phases respectively. Equation (A.24) is to be transformed from the stationary a,b,c axis to an arbitrary rotating d,q,γ axis. Thus in Figure A.2, $\omega_2 = 0,\ \omega_1 = \omega$ and

$$[C]^T = \sqrt{\frac{2}{3}} \begin{bmatrix} \cos(\theta) & -\sin(\theta) & \frac{1}{\sqrt{2}} \\ \cos(\theta - 120°) & -\sin(\theta - 120°) & \frac{1}{\sqrt{2}} \\ \cos(\theta + 120°) & -\sin(\theta + 120°) & \frac{1}{\sqrt{2}} \end{bmatrix} \tag{A.25}$$

Therefore

$$[V_{s1 \quad s2 \quad s3}] = [C]^T.[V_{sd \quad sq \quad s\gamma}] \tag{A.26}$$

$$[I_{s1 \quad s2 \quad s3}] = [C]^T.[I_{sd \quad sq \quad s\gamma}] \tag{A.27}$$

$$\frac{d}{dt}[\Psi_{s1 \quad s2 \quad s3}] = \frac{d}{dt}\{[C]^T.[\Psi_{sd \quad sq \quad s\gamma}]\} \tag{A.28}$$

Matrix $[C]^T$ of equation (A.25) is time dependent because θ is a function of time. Thus equation (A.28) is expanded as follows :

$$\frac{d}{dt}\begin{bmatrix}\Psi_{s1}\\ \Psi_{s2}\\ \Psi_{s3}\end{bmatrix}=\frac{d}{dt}\left\{\sqrt{\frac{2}{3}}\begin{bmatrix}\cos(\theta) & -\sin(\theta) & \frac{1}{\sqrt{2}}\\ \cos(\theta-120°) & -\sin(\theta-120°) & \frac{1}{\sqrt{2}}\\ \cos(\theta+120°) & -\sin(\theta+120°) & \frac{1}{\sqrt{2}}\end{bmatrix}.\begin{bmatrix}\Psi_{sd}\\ \Psi_{sq}\\ \Psi_{s\gamma}\end{bmatrix}\right\}$$

$$=\sqrt{\frac{2}{3}}\begin{bmatrix}\sin(\theta) & -\cos(\theta) & 0\\ -\sin(\theta-120°) & -\cos(\theta-120°) & 0\\ -\sin(\theta+120°) & -\cos(\theta+120°) & 0\end{bmatrix}.\begin{bmatrix}\Psi_{sd}\\ \Psi_{sq}\\ \Psi_{s\gamma}\end{bmatrix}\omega_1$$

$$+\sqrt{\frac{2}{3}}\begin{bmatrix}\cos(\theta) & -\sin(\theta) & \frac{1}{\sqrt{2}}\\ \cos(\theta-120°) & -\sin(\theta-120°) & \frac{1}{\sqrt{2}}\\ \cos(\theta+120°) & -\sin(\theta+120°) & \frac{1}{\sqrt{2}}\end{bmatrix}\frac{d}{dt}\begin{bmatrix}\Psi_{sd}\\ \Psi_{sq}\\ \Psi_{s\gamma}\end{bmatrix}$$

$$=\sqrt{\frac{2}{3}}\begin{bmatrix}\cos(\theta) & -\sin(\theta) & \frac{1}{\sqrt{2}}\\ \cos(\theta-120°) & -\sin(\theta-120°) & \frac{1}{\sqrt{2}}\\ \cos(\theta+120°) & -\sin(\theta+120°) & \frac{1}{\sqrt{2}}\end{bmatrix}\begin{bmatrix}\frac{d}{dt}\Psi_{sd}-\omega_1\Psi_{sq}\\ \frac{d}{dt}\Psi_{sq}+\omega_1\Psi_{sd}\\ \frac{d}{dt}\Psi_{s\gamma}\end{bmatrix} \qquad \text{(A.29)}$$

$$=[C]^T\left\{\frac{d}{dt}\begin{bmatrix}\Psi_{sd}\\ \Psi_{sq}\\ \Psi_{s\gamma}\end{bmatrix}+\omega\begin{bmatrix}-\Psi_{sq}\\ \Psi_{sd}\\ 0\end{bmatrix}\right\}$$

Substituting equations (A.26, A.27 and A.29) into equation (A.24) gives the stator transformed voltage equations as :

$$[C]^T\begin{bmatrix}V_{sd}\\V_{sq}\\V_{s\gamma}\end{bmatrix}=R_s[C]^T\begin{bmatrix}I_{sd}\\I_{sq}\\I_{s\gamma}\end{bmatrix}+[C]^T\left\{\frac{d}{dt}\begin{bmatrix}\Psi_{sd}\\\Psi_{sq}\\\Psi_{s\gamma}\end{bmatrix}+\omega\begin{bmatrix}-\Psi_{sq}\\\Psi_{sd}\\0\end{bmatrix}\right\} \tag{A.30}$$

or

$$[V_{sd\quad sq\quad s\gamma}]=R_s[I_{sd\quad sq\quad s\gamma}]+\frac{d}{dt}[\Psi_{sd\quad sq\quad s\gamma}]+\omega[\Psi_{-sq\quad sd\quad 0}] \tag{A.31}$$

Rotor transformations

The rotor voltage equations can be expressed as

$$\begin{bmatrix}V'_{r}\\V'_{r2}\\V'_{r3}\end{bmatrix}=R'_r\begin{bmatrix}I'_{r1}\\I'_{r2}\\I'_{r3}\end{bmatrix}+\frac{d}{dt}\begin{bmatrix}\Psi'_{r1}\\\Psi'_{r2}\\\Psi'_{r3}\end{bmatrix} \tag{A.32}$$

where r1,r2,r3 are the rotor a,b,c phases respectively. Equation (A.32) is to be transformed from the rotating a,b,c axis to the same arbitrary rotating d,q,γ axis as for the stator. Thus in Figure A.2, $\omega_2=\omega_r$ and $\omega_1=\omega$

where ω_r is the speed of the rotor.

The transformation is

$$[C]^T = \sqrt{\frac{2}{3}} \begin{bmatrix} \cos(\theta-\theta_r) & -\sin(\theta-\theta_r) & \frac{1}{\sqrt{2}} \\ \cos(\theta-\theta_r-120°) & -\sin(\theta-\theta_r-120°) & \frac{1}{\sqrt{2}} \\ \cos(\theta-\theta_r+120°) & -\sin(\theta-\theta_r+120°) & \frac{1}{\sqrt{2}} \end{bmatrix} \tag{A.33}$$

and following a similar procedure to that used for the stator gives the rotor transformed voltage equations as :

$$[C]^T \begin{bmatrix} V'_{rd} \\ V'_{rq} \\ V'_{r\gamma} \end{bmatrix} = R'_r [C]^T \begin{bmatrix} I'_{rd} \\ I'_{rq} \\ I'_{r\gamma} \end{bmatrix} + [C]^T \left\{ \frac{d}{dt} \begin{bmatrix} \Psi'_{rd} \\ \Psi'_{rq} \\ \Psi'_{r\gamma} \end{bmatrix} + (\omega-\omega_r) \begin{bmatrix} -\Psi'_{rq} \\ \Psi'_{rd} \\ 0 \end{bmatrix} \right\} \tag{A.34}$$

or

$$[V'_{rd\ \ rq\ \ r\gamma}] = R'_r [I'_{rd\ \ rq\ \ r\gamma}] + \frac{d}{dt} [\Psi'_{rd\ \ rq\ \ r\gamma}] + (\omega-\omega_r)\, [\Psi'_{-rq\ \ rd\ \ 0}] \tag{A.35}$$

Stator and rotor d-q axis equations

Due to the fact that the three phase configuration of both the stator and rotor is balanced and that the air-gap is uniform, the resistances and inductances are equal for each stator phase and each rotor phase respectively. This implies that the resistances and inductances of the d-q axis windings are equal for the stator and rotor respectively. Also, because only balanced winding conditions are under consideration, the γ-axis equations are discarded. Thus the flux linkages of the stator and rotor are defined as follows :

$$\begin{aligned}\Psi_{sd} &= L_s I_{sd} + M I'_{rd} \\ \Psi_{sq} &= L_s I_{sq} + M I'_{rq} \\ \Psi'_{rd} &= L'_r I'_{rd} + M I_{sd} \\ \Psi'_{rq} &= L'_r I'_{rq} + M I_{sq}\end{aligned} \tag{A.36}$$

and substituting equations (A.36) into (A.31) and (A.35) gives the d-q axis induction motor equations as ;

$$V_{sd} = R_s I_{sd} + L_s \frac{d}{dt} I_{sd} + M \frac{d}{dt} I'_{rd} - \omega L_s I_{sq} - \omega M I'_{rq} \tag{A.37}$$

$$V_{sq} = R_s I_{sq} + L_s \frac{d}{dt} I_{sq} + M \frac{d}{dt} I'_{rq} + \omega L_s I_{sd} + \omega M I'_{rd} \tag{A.38}$$

$$V_{rd} = 0 = R'_r I'_{rd} + L'_r \frac{d}{dt} I'_{rd} + M \frac{d}{dt} I_{sd} - (\omega - \omega_r) L'_r I'_{rq} - (\omega - \omega_r) M I_{sq} \tag{A.39}$$

$$V_{rq} = 0 = R'_r I'_{rq} + L'_r \frac{d}{dt} I'_{rq} + M \frac{d}{dt} I_{sq} + (\omega - \omega_r) L'_r I'_{rd} + (\omega - \omega_r) M I_{sd} \tag{A.40}$$

or in matrix form

$$\begin{bmatrix} V_{sd} \\ V_{sq} \\ 0 \\ 0 \end{bmatrix} = \begin{bmatrix} R_s + L_s \frac{d}{dt} & -\omega L_s & M \frac{d}{dt} & -\omega M \\ \omega L_s & R_s + L_s \frac{d}{dt} & \omega M & M \frac{d}{dt} \\ M \frac{d}{dt} & -(\omega - \omega_r) M & R'_r + L'_r \frac{d}{dt} & -(\omega - \omega_r) L'_r \\ (\omega - \omega_r) M & M \frac{d}{dt} & (\omega - \omega_r) L'_r & R'_r + L'_r \frac{d}{dt} \end{bmatrix} \begin{bmatrix} I_{sd} \\ I_{sq} \\ I'_{rd} \\ I'_{rq} \end{bmatrix} \tag{A.41}$$

The two rotor voltages, V_{rd} and V_{rq}, are set to zero in equations (A.39 - A.41) because in a squirrel cage motor, the rotor is short circuited. Setting these voltages to zero is only valid for squirrel cage motors.

APPENDIX B

Resistance And Leakage Inductance Of A Rectangular Bar Rotor

This Appendix shows the method used to calculate the resistance and leakage inductance of a rectangular bar in an open slot. This is used to obtain the equivalent circuit of an induction motor.

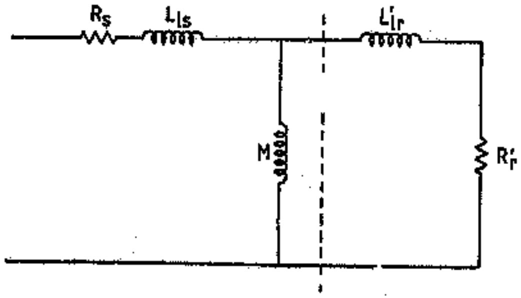

Figure B.1 : **Equivalent Circuit Of Induction Motor**

The per phase equivalent circuit of an induction motor with rotor values referred to the stator is shown in Figure B.1, where the stator and rotor leakage inductances are given as $L_{ls} = L_s - M$ and $L'_{lr} = L'_r - M$ respectively.

Referring to Figure B.2, the rotor slot leakage inductance for one bar in an open, rectangular slot is obtained from the permeance coefficient per unit axial length of the slot as

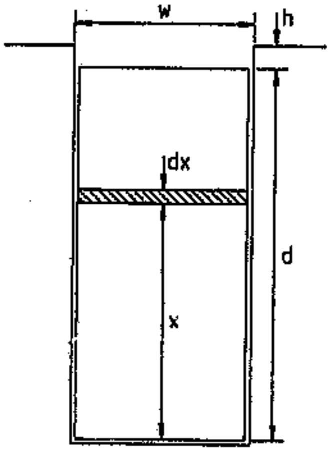

Figure B.2 : **Rectangular Bar In An Open Slot**

$$L_{lr} = \mu_0 l_c(\lambda_0 + \lambda_b) \tag{B.1}$$

λ_0 is the permeance coefficient of the slot area above the bar, and is equal to h/w. The permeance coefficient of the bar itself, λ_b, is more complex. To calculate the leakage flux of the whole bar, the leakage flux $d\Phi_{dx}$ in the elemental path dx (at height x from the bottom of the bar), is given as

$$d\Phi_{dx} = B_x(dA_{dx}) \tag{B.2}$$

where $(dA_{dx}) = l_c\,(dx)$ = the area that the flux links and

$$B_x = \mu_0 H_x = \mu_0 \frac{N_x I_x}{w} \tag{B.3}$$

where w is the length of the flux path across the slot. Substituting for B_x gives

$$d\Phi_{dx} = \mu_0 l_c \frac{N_x I_x}{w} dx \tag{B.4}$$

The flux in path dx only links the fraction x/d of the conductor, and the flux density B_x is less than the total flux density because only the fraction x/d of the total conductor current is available to provide mmf. Therefore substituting for N_x and I_x as

$$N_x = \frac{x}{d} N_T \tag{B.5}$$

$$I_x = \frac{x}{d} I_T \tag{B.6}$$

into equation (B.4) gives the amount of flux in path dx as

$$d\Phi_{dx} = \frac{\mu_0}{w} l_c \frac{x}{d} N_T \frac{x}{d} I_T dx \tag{B.7}$$

Integrating this equation from x=0 to x=d gives the total flux as

$$\Phi = \frac{\mu_0}{w} l_c N_T I_T \frac{d}{3} \tag{B.8}$$

from which the permeance coefficient can be deduced as

$$\lambda_b = \frac{d}{3w} \tag{B.9}$$

The corresponding bar resistance is

$$R_b = \frac{\rho l_b}{wd} \tag{B.10}$$

The values L_{lr} and R_b of equations (B.1) and (B.10) respectively, are then modified to account for all the rotor bars and referred to the stator to give L'_{lr} and R'_r of the equivalent circuit.

APPENDIX C

Differential Equations Of Lumped Parameter Circuits

This Appendix gives the differential equations of the lumped parameter circuits which are discussed in Chapter 3. Equations are given for the T model, the Pi model and the improved Pi model.

The differential equations given in this Appendix are all in a rotor fixed reference frame so that the rotational terms (those with ω_r) appear in the stator equations instead of the rotor equations. This has been done because the rotor equations are now not as simple as those of the traditional fourth order model, but are much more complicated to account for deep bar effects. For each circuit the differential equations for both the stator and the rotor will be presented.

T Model

The equivalent circuit of an n section T model is shown in Figure C.1. The rotor resistance and leakage inductance of each section is given by equations (3.1) and (3.2) respectively.

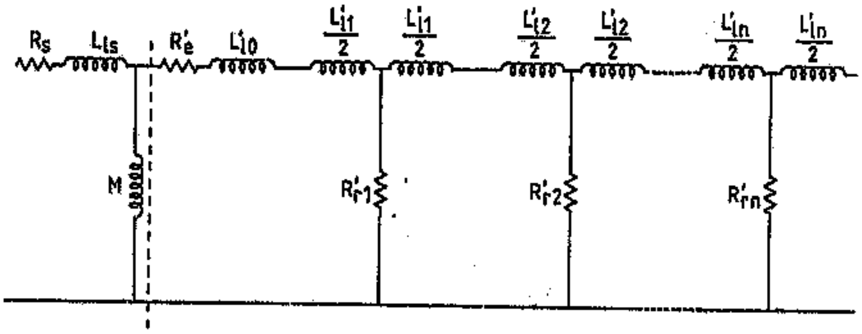

Figure C.1 : Equivalent Circuit Of The T Model

The series inductances are combined to give the circuit of Figure C.2, where the subscript i,j refers to a value composed of an ith and a jth component. The values of the reduced circuit are obtained from the original circuit by the relationships

$$R_i = R'_i$$

$$L_{0,1} = L'_{l0} + \frac{1}{2}L'_{l1}$$

$$L_{i,j} = \frac{1}{2}L'_{li} + \frac{1}{2}L'_{lj} \qquad \text{(C.2)}$$

Please note that these new inductances $L_{i,j}$ are all leakage inductances even though the subscript l has been omitted.

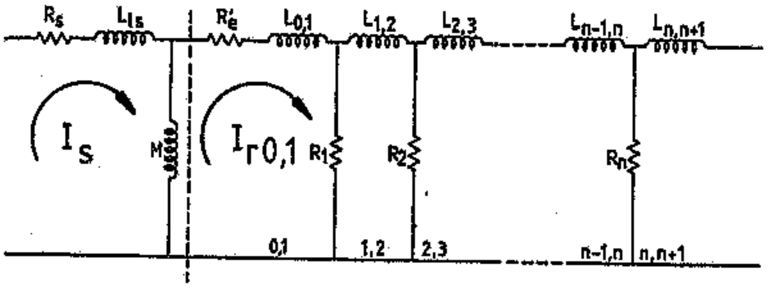

Figure C.2 : **Reduced Equivalent Circuit Of The T Model**

For this system, the stator equations are

$$V_{sd} = R_s I_{sd} + L_s \frac{d}{dt} I_{sd} + M \frac{d}{dt} I'_{rd} + \omega_r M I'_{rq} + \omega_r L_s I_{sq} \tag{C.3}$$

$$V_{sq} = R_s I_{sq} + L_s \frac{d}{dt} I_{sq} + M \frac{d}{dt} I'_{rq} - \omega_r M I'_{rd} - \omega_r L_s I_{sd} \tag{C.4}$$

and the equations for the loops are

first loop (0,1) :

$$\begin{aligned} V'_{rd\,0,1} = 0 = & (R_1 + R'_e) I'_{rd\,0,1} + L_{0,1} \frac{d}{dt} I'_{rd\,0,1} \\ & - R_1 I'_{rd\,1,2} + M \frac{d}{dt} I'_{rd\,0,1} + M \frac{d}{dt} I_{sd} \end{aligned} \tag{C.5}$$

$$V'_{rq\,0,1} = 0 = (R_1 + R'_e)I'_{rq\,0,1} + L_{0,1}\frac{d}{dt}I'_{rq\,0,1}$$

$$-R_1 I'_{rq\,1,2} + M\frac{d}{dt}I'_{rq\,0,1} + M\frac{d}{dt}I_{sq} \qquad \text{(C.6)}$$

intermediate loops (i,j) :

$$V'_{rd\,i,j} = 0 = -R_i I'_{rd\,i-1,i} + (R_i + R_j)I'_{rd\,i,j}$$

$$-R_j I'_{rd\,j,j+1} + L_{i,j}\frac{d}{dt}I'_{rd\,i,j} \qquad \text{(C.7)}$$

$$V'_{rq\,i,j} = 0 = -R_i I'_{rq\,i-1,i} + (R_i + R_j)I'_{rq\,i,j}$$

$$-R_j I'_{rq\,j,j+1} + L_{i,j}\frac{d}{dt}I'_{rq\,i,j} \qquad \text{(C.8)}$$

last loop (n) :

$$V'_{rd\,n-1,n} = 0 = -R_{n-1}I'_{rd\,n-2,n-1}$$

$$+(R_{n-1} + R_n)I'_{rd\,n-1,n} + L_{n-1,n}\frac{d}{dt}I'_{rd\,n-1,n} \qquad \text{(C.9)}$$

$$V'_{rd\,n-1,n} = 0 = -R_{n-1}I'_{rd\,n-2,n-1}$$

$$+(R_{n-1} + R_n)I'_{rd\,n-1,n} + L_{n-1,n}\frac{d}{dt}I'_{rd\,n-1,n} \qquad \text{(C.10)}$$

Pi Model

The equivalent circuit of an n section Pi model is shown in Figure C.3. The rotor resistance and leakage inductance of each section is given by equations (3.1) and (3.2) respectively.

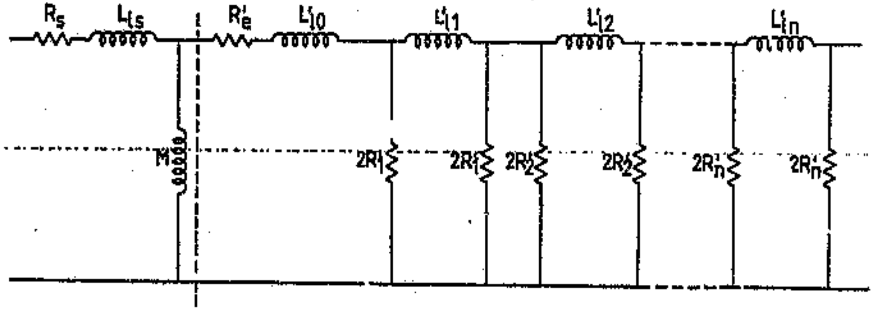

Figure C.3 : **Equivalent Circuit Of The Pi Model**

The parallel resistances are combined to give the circuit of Figure C.4, where

$$R_0 = 2R'_1$$

$$R_n = 2R'_n$$

$$R_i = 2R'_i \parallel 2R_{i+1} = \frac{2R'_i R'_{i+1}}{R'_i + R'_{i+1}}$$

$$L_i = L'_{li} \qquad \text{(C.11)}$$

Please note that these new inductances L_i are all leakage inductances even though the subscript l has been omitted.

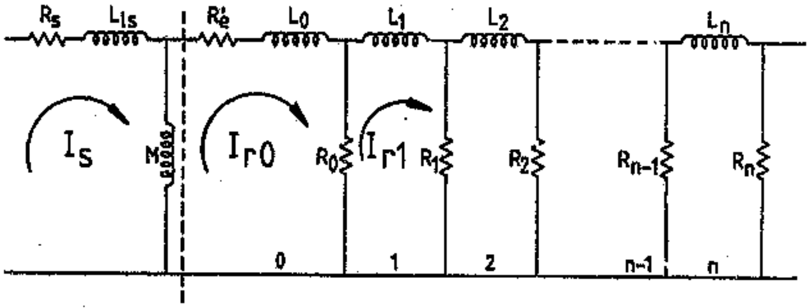

Figure C.4 : **Reduced Equivalent Circuit Of The Pi Model**

For this system, the stator equations are

$$V_{sd} = R_s I_{sd} + L_s \frac{d}{dt} I_{sd} + M \frac{d}{dt} I'_{rd} + \omega_r M I'_{rq} + \omega_r L_s I_{sq} \tag{C.12}$$

$$V_{sq} = R_s I_{sq} + L_s \frac{d}{dt} I_{sq} + M \frac{d}{dt} I'_{rq} - \omega_r M I'_{rd} - \omega_r L_s I_{sd} \tag{C.13}$$

and the equations for the loops are

first loop (0) :

$$\begin{aligned} V'_{rd\,0} = 0 = & (R_0 + R'_e) I'_{rd\,0} + L_0 \frac{d}{dt} I'_{rd\,0} \\ & - R_0 I'_{rd\,1} + M \frac{d}{dt} I'_{rd\,0} + M \frac{d}{dt} I_{sd} \end{aligned} \tag{C.14}$$

$$V'_{rq\,0} = 0 = (R_0 + R'_e)I'_{rq\,0} + L_0 \frac{d}{dt} I'_{rq\,0}$$

$$- R_0 I'_{rq\,1} + M \frac{d}{dt} I'_{rq\,0} + M \frac{d}{dt} I_{sq} \tag{C.15}$$

intermediate loops (i) :

$$V'_{rd\,i} = 0 = -R_{i-1} I'_{rd\,i-1} + (R_{i-1} + R_i) I'_{rd\,i} - R_i I'_{rd\,i+1} + L_i \frac{d}{dt} I'_{rd\,i} \tag{C.16}$$

$$V'_{rq\,i} = 0 = -R_{i-1} I'_{rq\,i-1} + (R_{i-1} + R_i) I'_{rq\,i} - R_i I'_{rq\,i+1} + L_i \frac{d}{dt} I'_{rq\,i} \tag{C.17}$$

last loop (n) :

$$V'_{rd\,n} = 0 = -R_{n-1} I'_{rd\,n} \quad + (R_{n-1} + R_n) I'_{rd\,n} + L_n \frac{d}{dt} I'_{rd\,n} \tag{C.18}$$

$$V'_{rq\,n} = 0 = -R_{n-1} I'_{rq\,n-1} + (R_{n-1} + R_n) I'_{rq\,n} + L_n \frac{d}{dt} I'_{rq\,n} \tag{C.19}$$

Improved Pi Model

The equivalent circuit of an n section improved Pi model is shown in Figure C.5. The rotor resistance and leakage inductance of each section is given by equations (3.1) and (3.2) respectively.

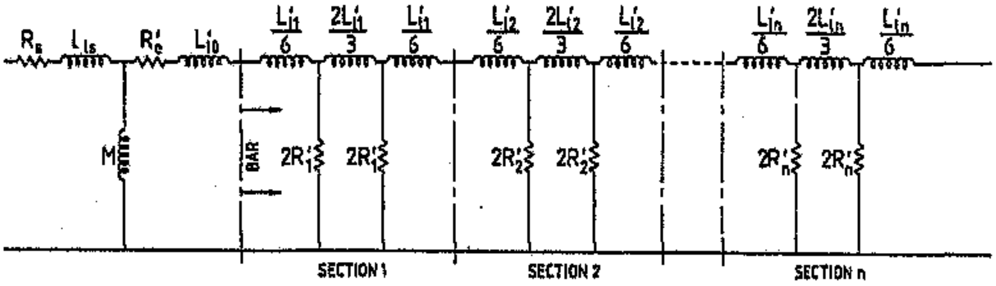

Figure C.5 : **Equivalent Circuit Of The Improved Pi Model**

The series inductances are combined to give the circuit of Figure C.6, where subscripts i refer to values of the i^{th} section, subscripts j refer to the j^{th} section and subscripts i,j refer to combinations of the i^{th} and j^{th} section. The values of the reduced circuit are obtained from the original circuit by

$$R_i = 2R'_i$$

$$L_{0,1} = L'_{l0} + \frac{1}{6}L'_{l1}$$

$$L_i = \frac{2}{3}L'_{li}$$

$$L_{i,j} = \frac{1}{6}L'_{li} + \frac{1}{6}L'_{lj} \qquad \text{(C.20)}$$

Please note that these new inductances L_i and $L_{i,j}$ are all leakage inductances even though the subscript l has been omitted.

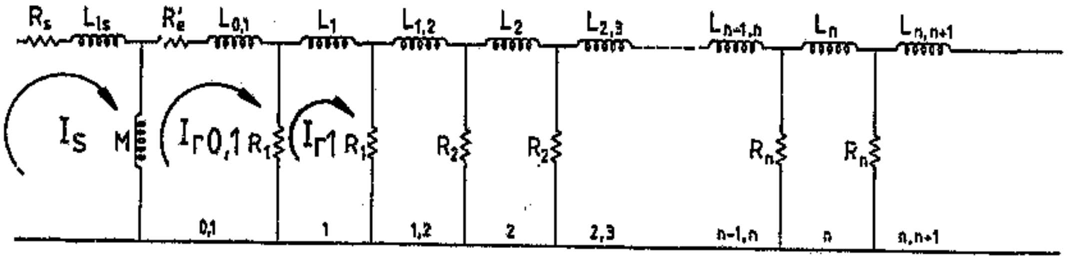

Figure C.6 : Reduced Equivalent Circuit Of Improved The Pi Model

For this system, the stator equations are

$$V_{sd} = R_s I_{sd} + L_s \frac{d}{dt} I_{sd} + M \frac{d}{dt} I'_{rd} + \omega_r M I'_{rq} + \omega_r L_s I_{sq} \tag{C.21}$$

$$V_{sq} = R_s I_{sq} + L_s \frac{d}{dt} I_{sq} + M \frac{d}{dt} I'_{rq} - \omega_r M I'_{rd} - \omega_r L_s I_{sd} \tag{C.22}$$

There will always be a specific equation for the first loop (0,1), for the last loop (n) and for each set of two intermediate loops (i) and (i,j). The equations for the loops are first loop (0,1) :

$$V'_{rd\,0,1} = 0 = (R_1 + R'_e)I'_{rd\,0,1} + L_{0,1}\frac{d}{dt}I'_{rd\,0,1}$$

$$-R_1 I'_{rd\,1} + M\frac{d}{dt}I'_{rd\,0,1} + M\frac{d}{dt}I_{sd} \tag{C.23}$$

$$V'_{rq\,0,1} = 0 = (R_1 + R'_e)I'_{rq\,0,1} + L_{0,1}\frac{d}{dt}I'_{rq\,0,1}$$

$$-R_1 I'_{rq\,1} + M\frac{d}{dt}I'_{rq\,0,1} + M\frac{d}{dt}I_{sq} \tag{C.24}$$

intermediate loops (i) :

$$V'_{rd\,i} = 0 = -R_i I'_{rd\,i-1,i} + 2R_i I'_{rd\,i} - R_i I'_{rd\,i,i+1} + L_i\frac{d}{dt}I'_{rd\,i} \tag{C.25}$$

$$V'_{rq\,i} = 0 = -R_i I'_{rq\,i-1,i} + 2R_i I'_{rq\,i} - R_i I'_{rq\,i,i+1} + L_i\frac{d}{dt}I'_{rq\,i} \tag{C.26}$$

and intermediate loops (i,j) :

$$V'_{rd\,i,j} = 0 = -R_i I'_{rd\,i} + (R_i + R_j)I'_{rd\,i,j} - R_j I'_{rd\,j} + L_{i,j}\frac{d}{dt}I'_{rd\,i,j} \tag{C.27}$$

$$V'_{rq\,i,j} = 0 = -R_i I'_{rq\,i} + (R_i + R_j)I'_{rq\,i,j} - R_j I'_{rq\,j} + L_{i,j}\frac{d}{dt}I'_{rq\,i,j} \tag{C.28}$$

last loop (n) :

$$V'_{rd\,n} = 0 = -R_n I'_{rd\,n-1,n} + 2R_n I'_{rd\,n} + L_n \frac{d}{dt} I'_{rd\,n} \tag{C.29}$$

$$V'_{rq\,n} = 0 = -R_n I'_{rq\,n-1,n} + 2R_n I'_{rq\,n} + L_n \frac{d}{dt} I'_{rq\,n} \tag{C.30}$$

APPENDIX D

Accuracy Of Different Lumped Parameter Circuits

This Appendix gives the full set of graphs of impedance error versus *num* of the three lumped parameter circuits. The graphs are given in order of increasing number of rotor bar sections, from two to fifteen, and in the order T, Pi and then improved Pi.

Note : the first few and/or last few points have purposefully been omitted from some of the graphs as the error at these points is very large and masks the trend of the other curves on that graph.

All results are given for the 254 kW, 3300 V, 3 phase, 50 Hz, 4 pole squirrel cage induction motor of Section 3.8.1. The curves are given for a sinusoidal supply feeding the motor with no attached load. The motor is initially at rest and is then supplied with full rated voltage and allowed to run up against its own inertia.

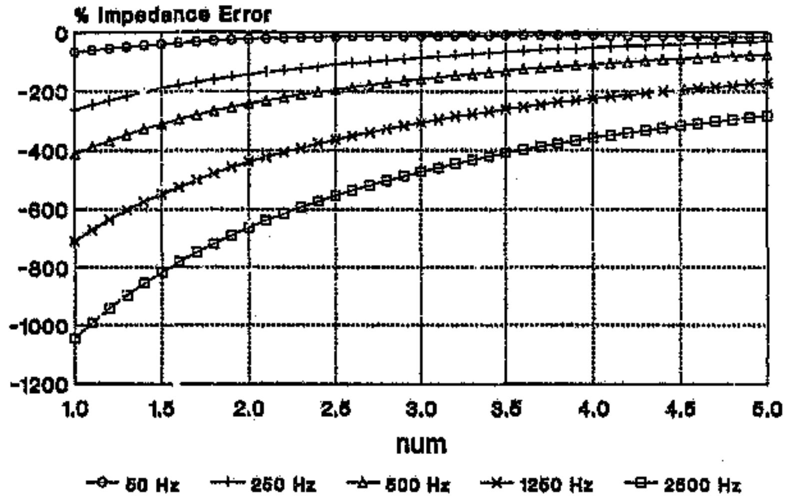

Figure D.1 : Variation Of Percentage Impedance Error With Value Of *num* At Different Frequencies For Two Sections Of The T Circuit

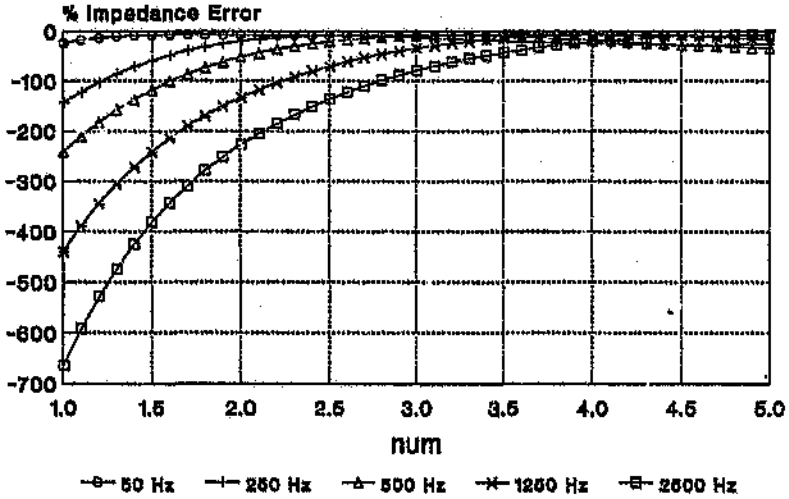

Figure D.2 : Variation Of Percentage Impedance Error With Value Of *num* At Different Frequencies For Three Sections Of The T Circuit

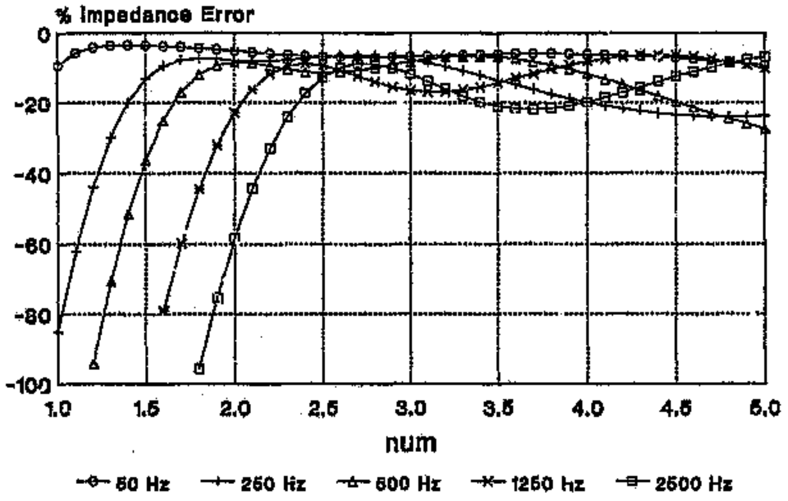

Figure D.3 : Variation Of Percentage Impedance Error With Value Of *num* At Different Frequencies For Four Sections Of The T Circuit

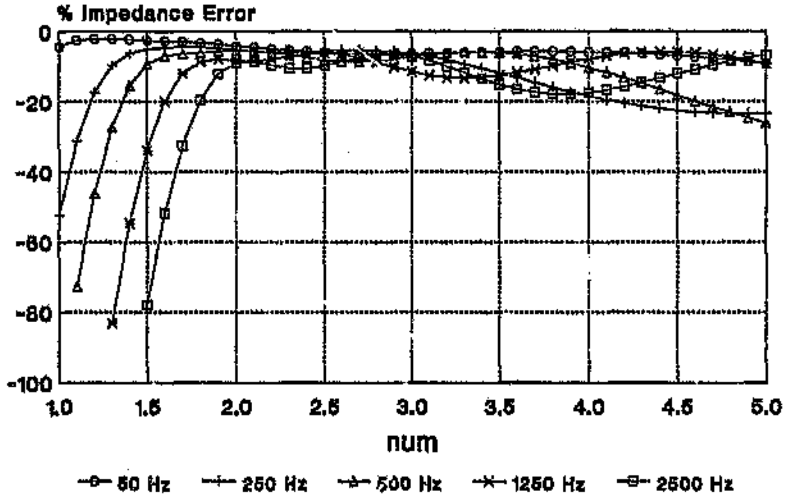

Figure D.4 : Variation Of Percentage Impedance Error With Value Of *num* At Different Frequencies For Five Sections Of The T Circuit

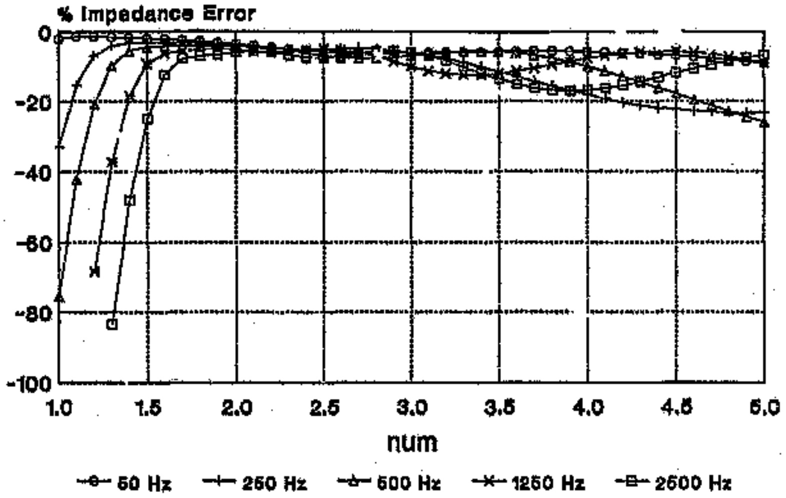

Figure D.5 : Variation Of Percentage Impedance Error With Value Of *num* At Different Frequencies For Six Sections Of The T Circuit

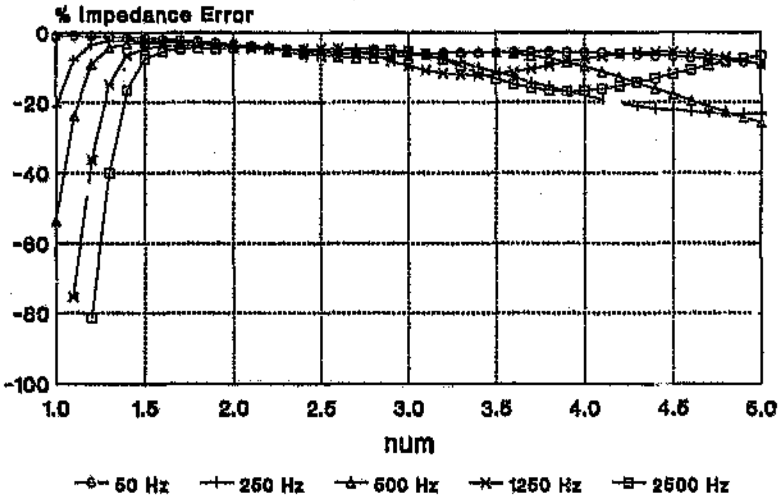

Figure D.6 : Variation Of Percentage Impedance Error With Value Of *num* At Different Frequencies For Seven Sections Of The T Circuit

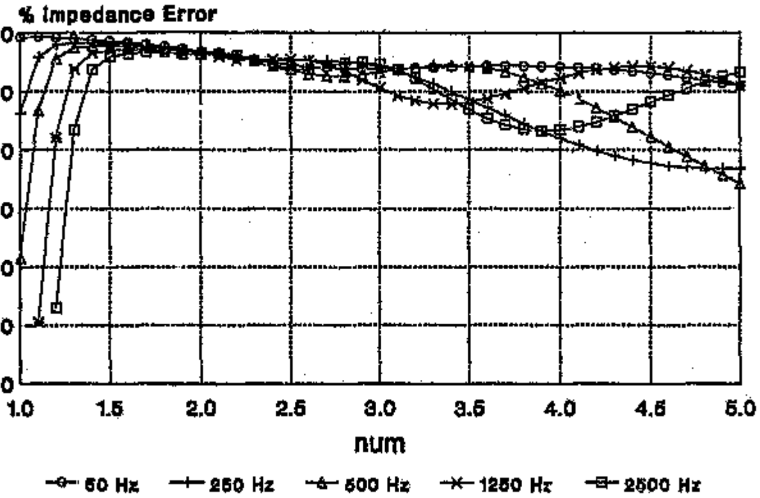

<u>Figure D.7</u> : Variation Of Percentage Impedance Error With Value Of *num* At Different Frequencies For Eight Sections Of The T Circuit

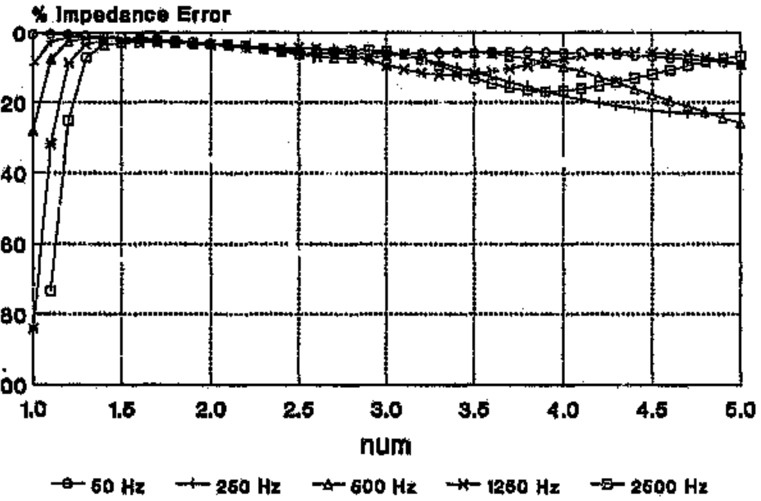

<u>Figure D.8</u> : Variation Of Percentage Impedance Error With Value Of *num* At Different Frequencies For Nine Sections Of The T Circuit

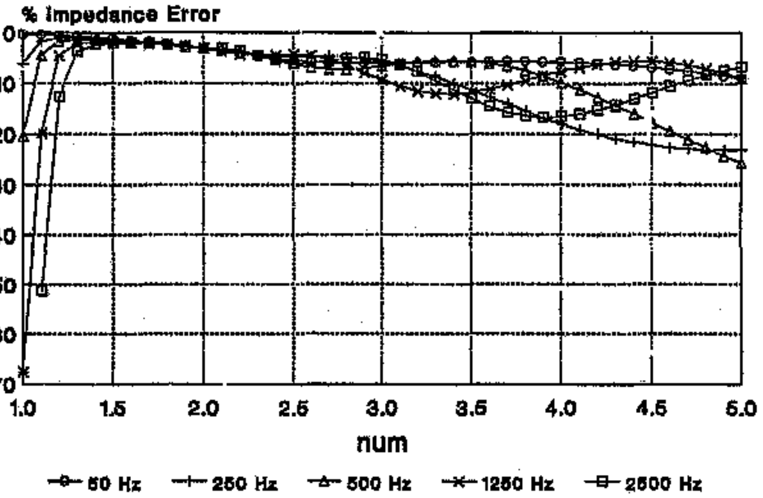

Figure D.9 : Variation Of Percentage Impedance Error With Value Of *num* At Different Frequencies For Ten Sections Of The T Circuit

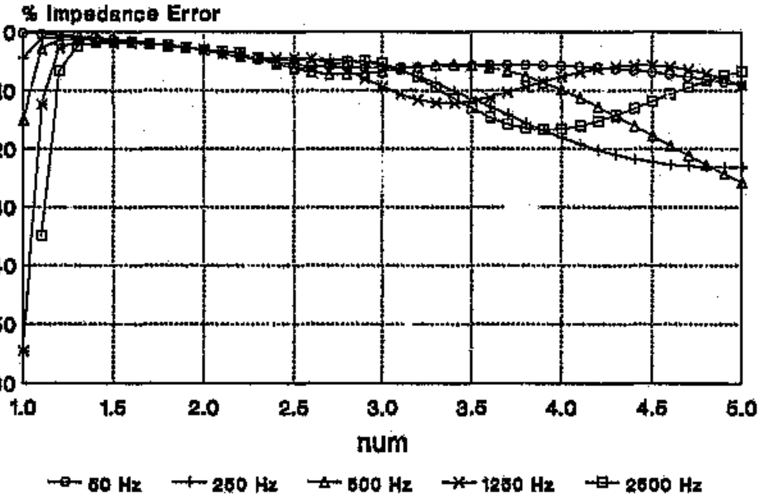

Figure D.10 : Variation Of Percentage Impedance Error With Value Of *num* At Different Frequencies For Eleven Sections Oı The T Circuit

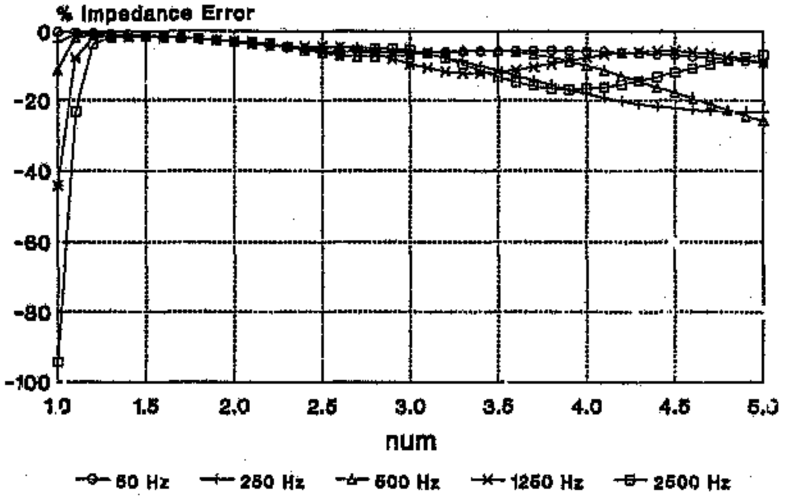

Figure D.11 : Variation Of Percentage Impedance Error With Value Of *num* At Different Frequencies For Twelve Sections Of The T Circuit

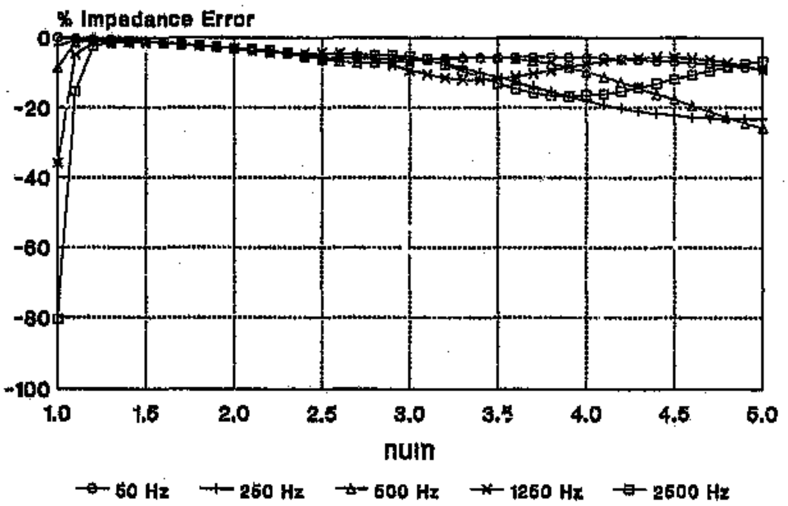

Figure D.12 : Variation Of Percentage Impedance Error With Value Of *num* At Different Frequencies For Thirteen Sections Of The T Circuit

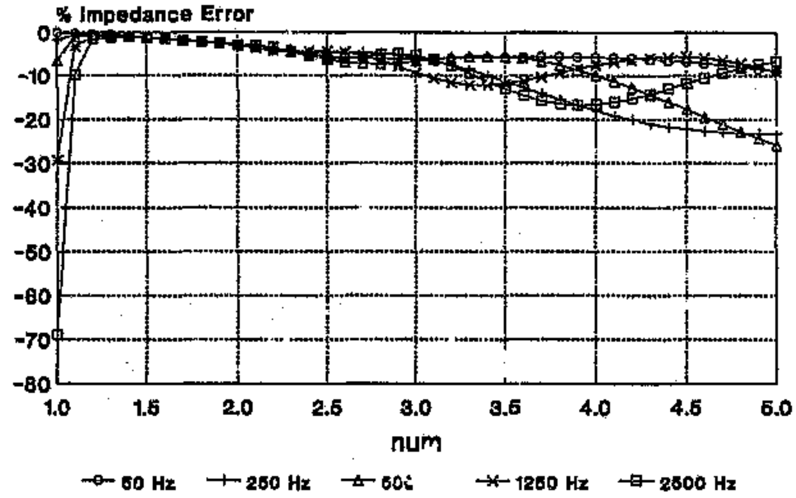

Figure D.13 : Variation Of Percentage Impedance Error With Value Of *num* At Different Frequencies For Fourteen Sections Of The T Circuit

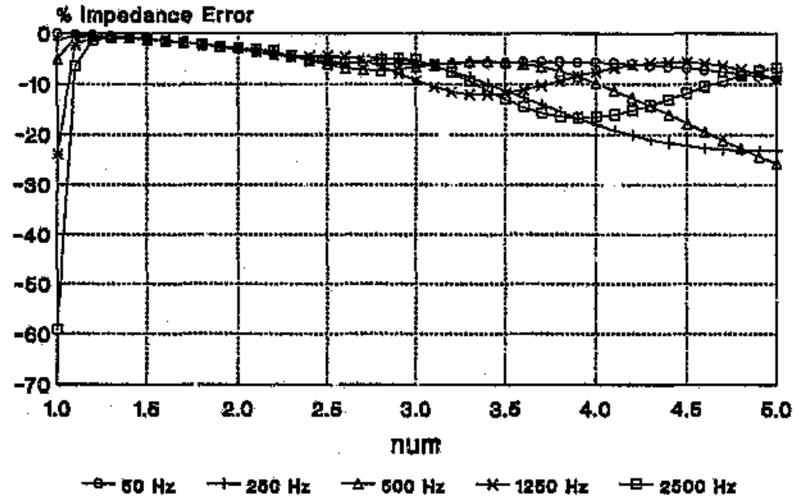

Figure D.14 : Variation Of Percentage Impedance Error With Value Of *num* At Different Frequencies For Fifteen Sections Of The T Circuit

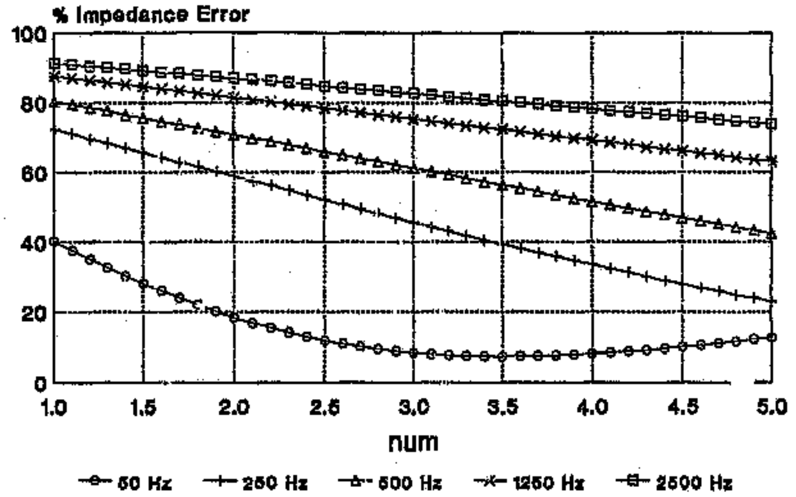

Figure D.15 : Variation Of Percentage Impedance Error With Value Of *num* At Different Frequencies For Two Sections Of The Pi Circuit

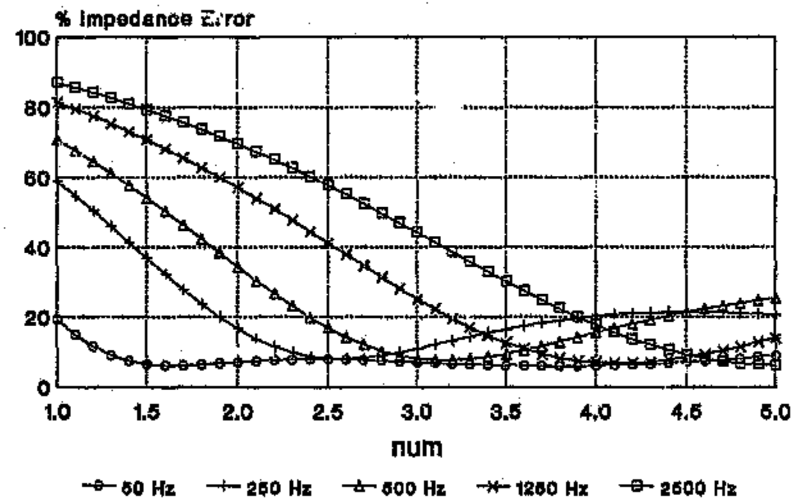

Figure D.16 : Variation Of Percentage Impedance Error With Value Of *num* At Different Frequencies For Three Sections Of The Pi Circuit

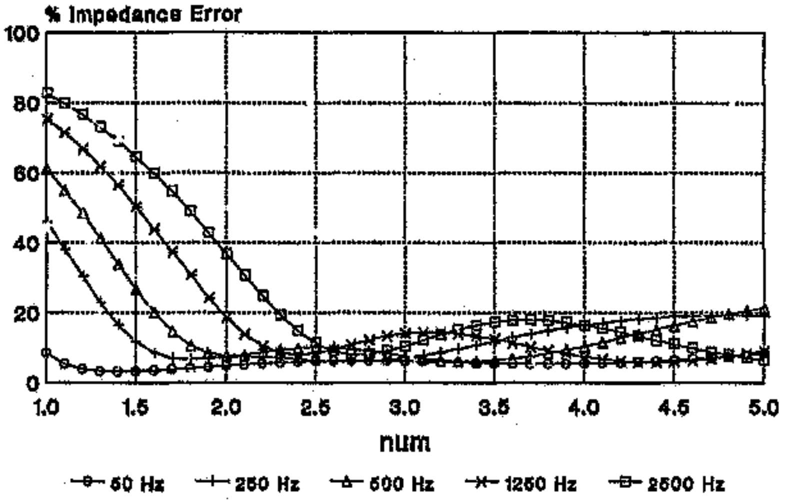

Figure D.17 : Variation Of Percentage Impedance Error With Value Of *num* At Different Frequencies For Four Sections Of The Pi Circuit

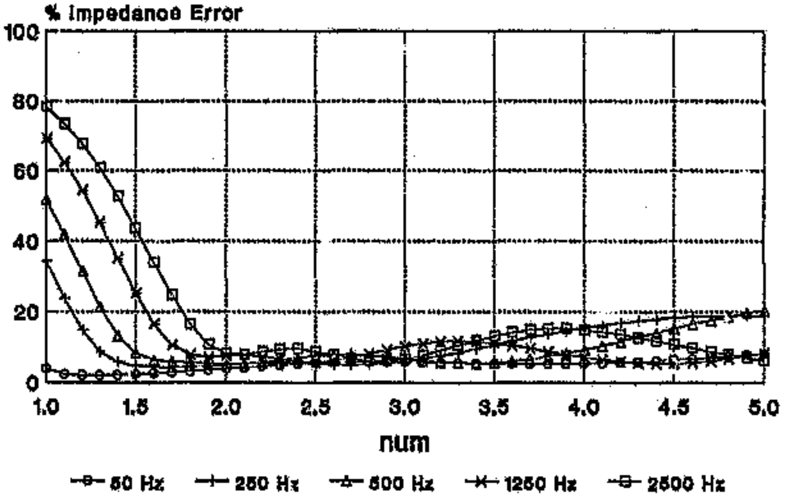

Figure D.18 : Variation Of Percentage Impedance Error With Value Of *num* At Different Frequencies For Five Sections Of The Pi Circuit

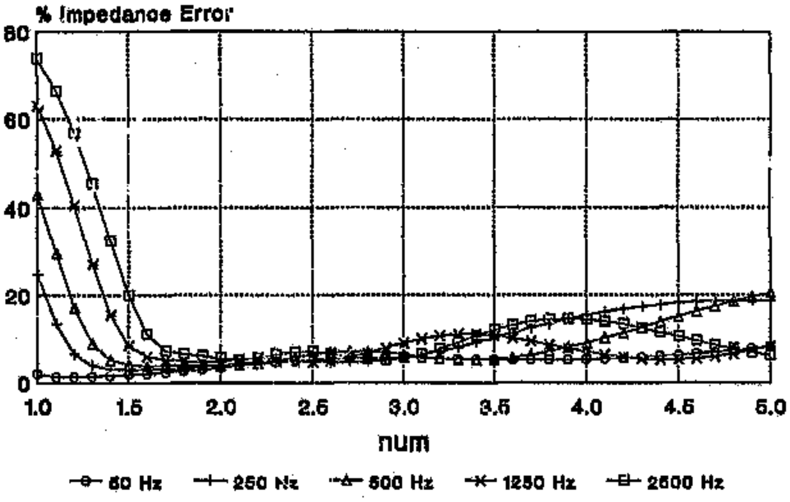

Figure D.19 : Variation Of Percentage Impedance Error With Value Of *num* At Different Frequencies For Six Sections Of The Pi Circuit

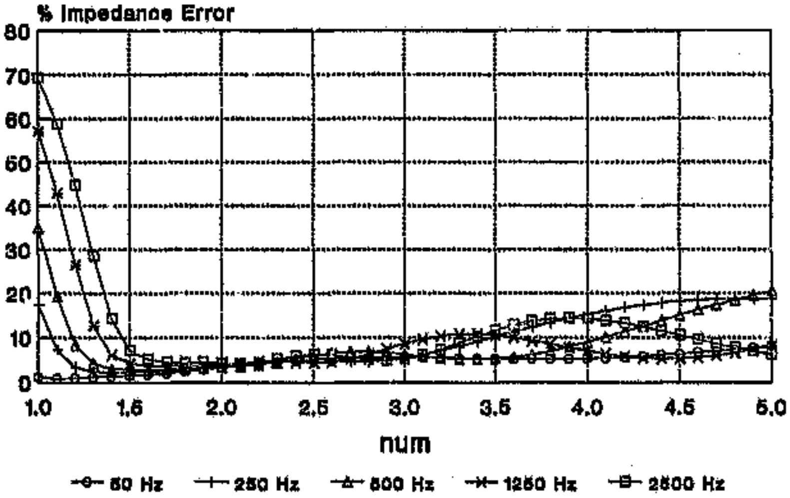

Figure D.20 : Variation Of Percentage Impedance Error With Value Of *num* At Different Frequencies For Seven Sections Of The Pi Circuit

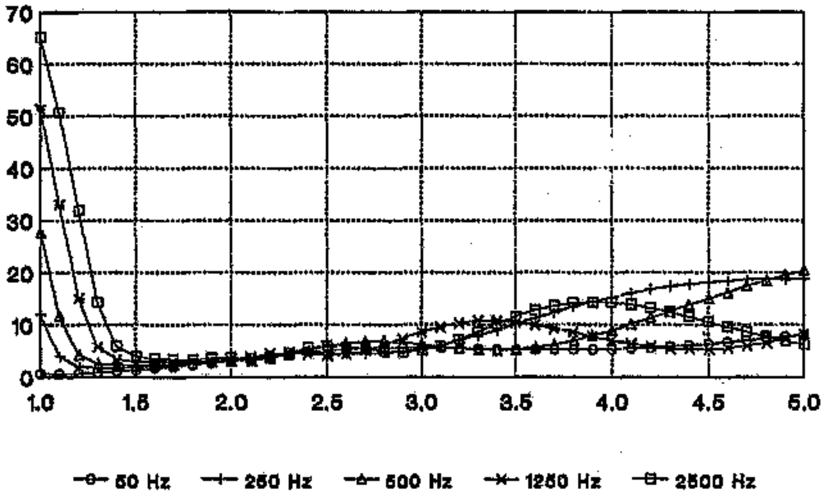

Figure D.21 : Variation Of Percentage Impedance Error With Value Of *num* At Different Frequencies For Eight Sections Of The Pi Circuit

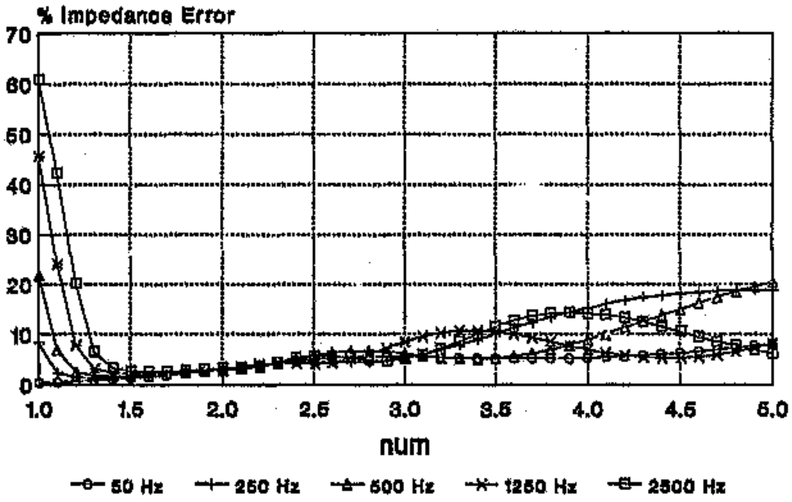

Figure D.22 : Variation Of Percentage Impedance Error With Value Of *num* At Different Frequencies For Nine Sections Of The Pi Circuit

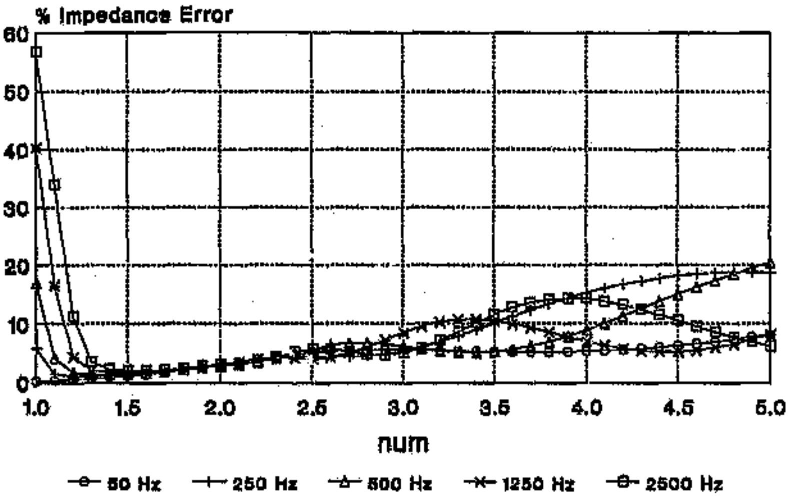

<u>Figure D.23</u> : Variation Of Percentage Impedance Error With Value Of *num* At Different Frequencies For Ten Sections Of The Pi Circuit

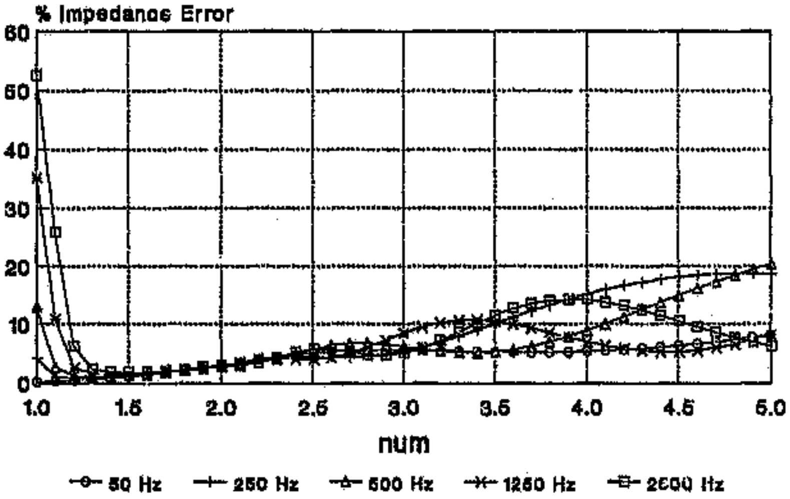

<u>Figure D.24</u> : Variation Of Percentage Impedance Error With Value Of *num* At Different Frequencies For Eleven Sections Of The Pi Circuit

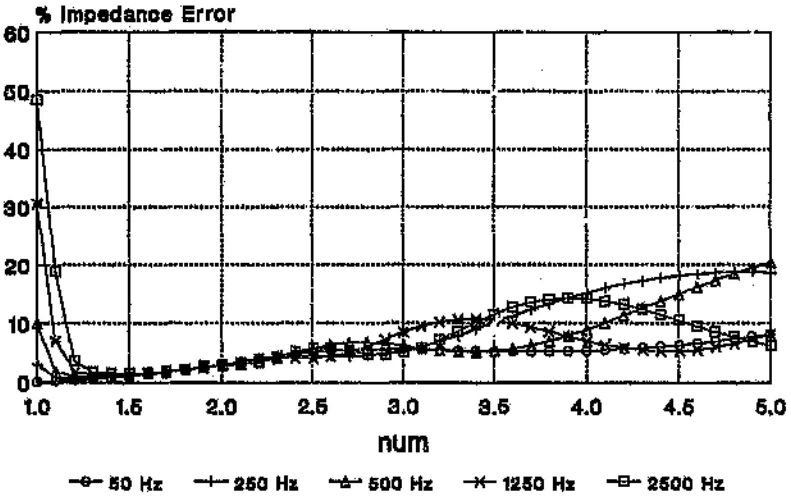

Figure D.25 : Variation Of Percentage Impedance Error With Value Of *num* At Different Frequencies For Twelve Sections Of The Pi Circuit

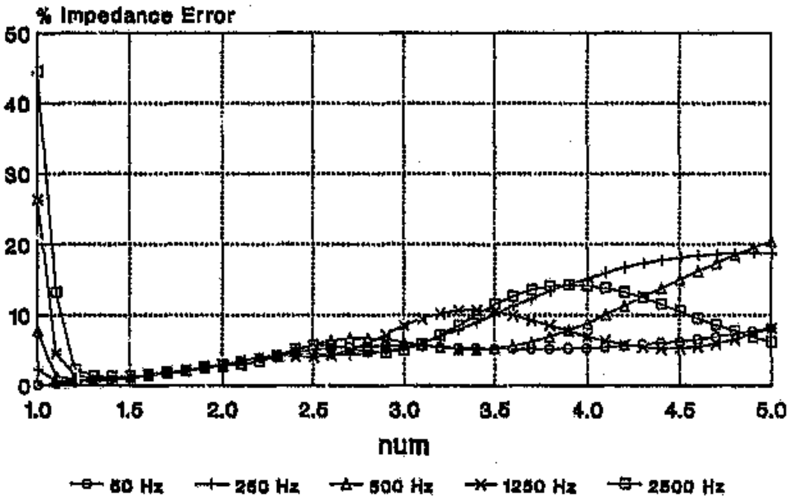

Figure D.26 : Variation Of Percentage Impedance Error With Value Of *num* At Different Frequencies For Thirteen Sections Of The Pi Circuit

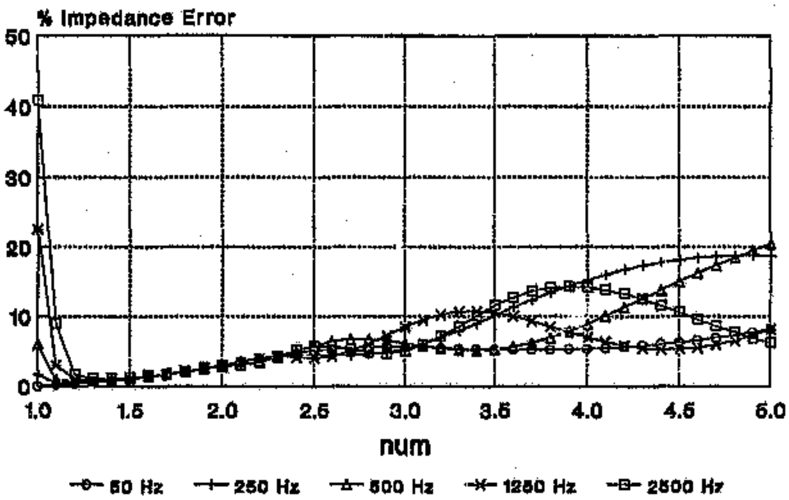

Figure D.27 : Variation Of Percentage Impedance Error With Value Of *num* At Different Frequencies For Fourteen Sections Of The Pi Circuit

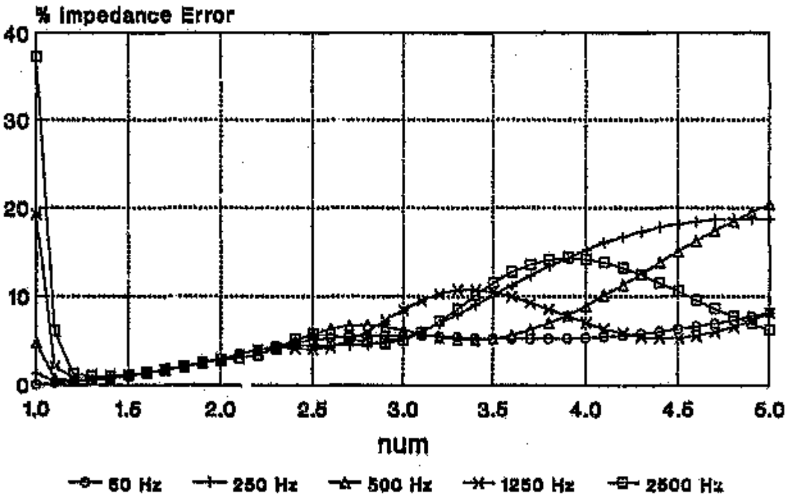

Figure D.28 : Variation Of Percentage Impedance Error With Value Of *num* At Different Frequencies For Fifteen Sections Of The Pi Circuit

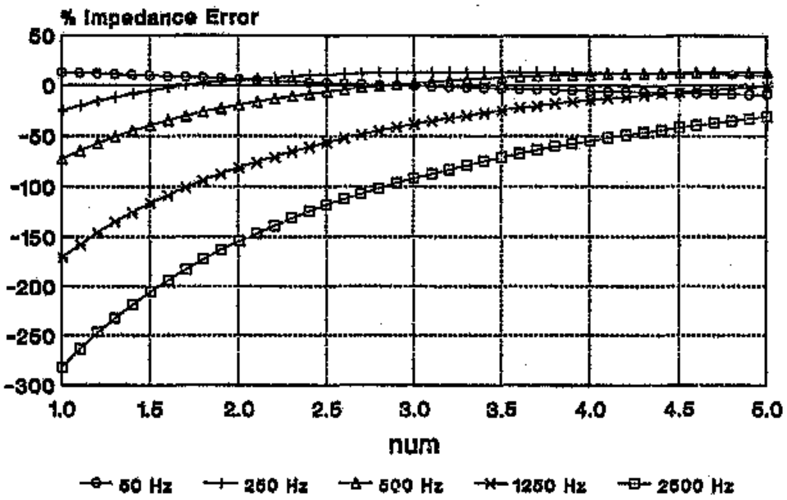

Figure D.29 : Variation Of Percentage Impedance Error With Value Of *num* At Different Frequencies For Two Sections Of The Improved Pi Circuit

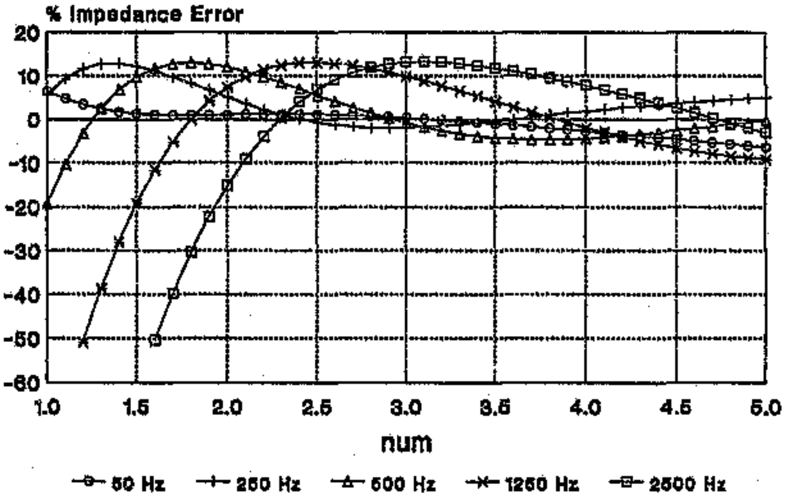

Figure D.30 : Variation Of Percentage Impedance Error With Value Of *num* At Different Frequencies For Three Sections Of The Improved Pi Circuit

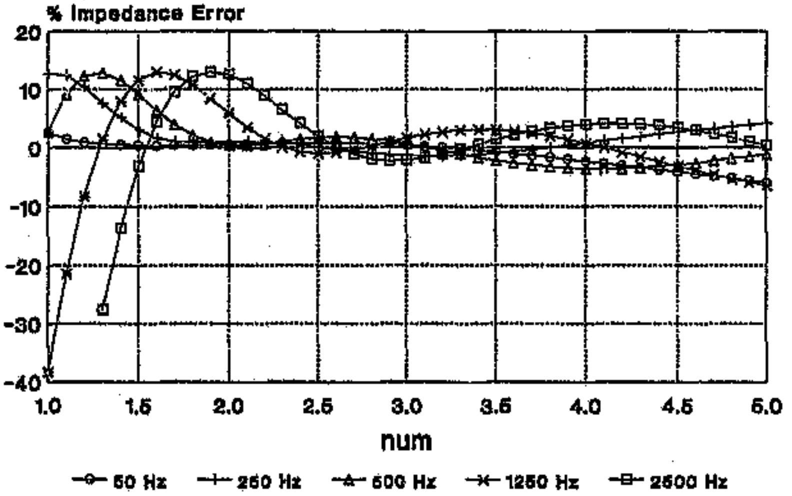

Figure D.31 : Variation Of Percentage Impedance Error With Value Of *num* At Different Frequencies For Four Sections Of The Improved Pi Circuit

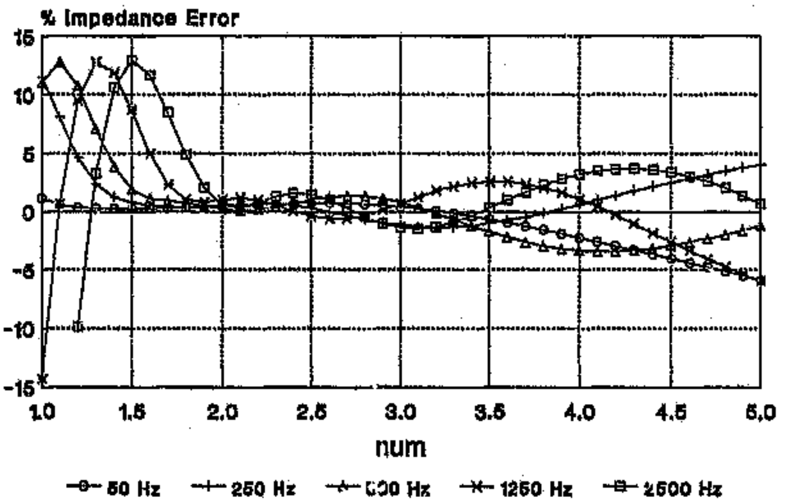

Figure D.32 : Variation Of Percentage Impedance Error With Value Of *num* At Different Frequencies For Five Sections Of The Improved Pi Circuit

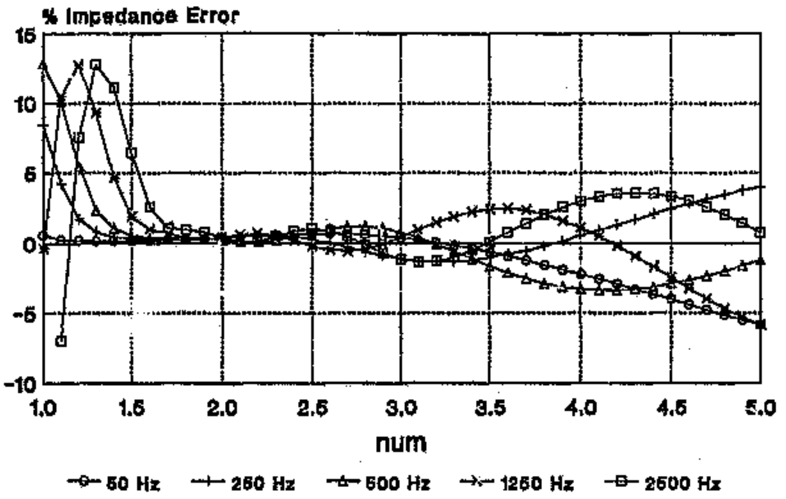

Figure D.33 : Variation Of Percentage Impedance Error With Value Of *num* At Different Frequencies For Six Sections Of The Improved Pi Circuit

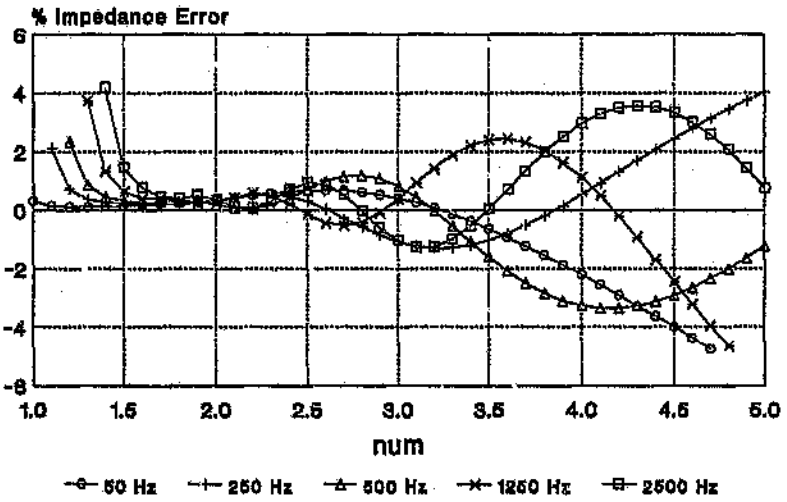

Figure D.34 : Variation Of Percentage Impedance Error With Value Of *num* At Different Frequencies For Seven Sections Of The Improved Pi Circuit

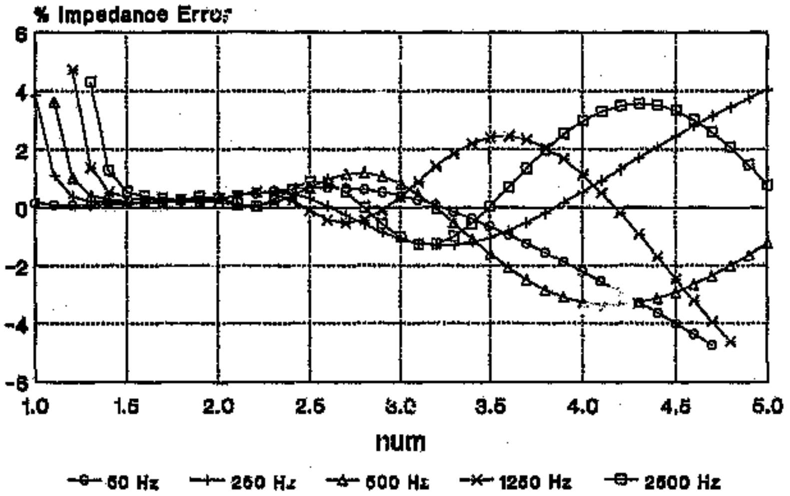

Figure D.35 : Variation Of Percentage Impedance Error With Value Of *num* At Different Frequencies For Eight Sections Of The Improved Pi Circuit

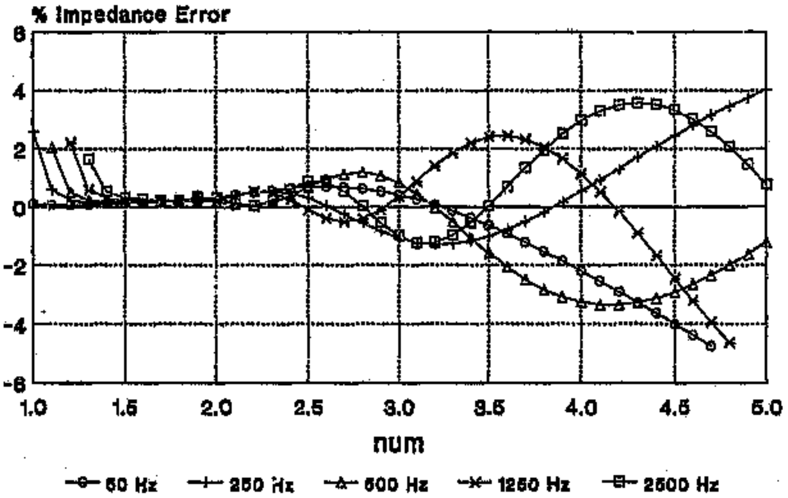

Figure D.36 : Variation Of Percentage Impedance Error With Value Of *num* At Different Frequencies For Nine Sections Of The Improved Pi Circuit

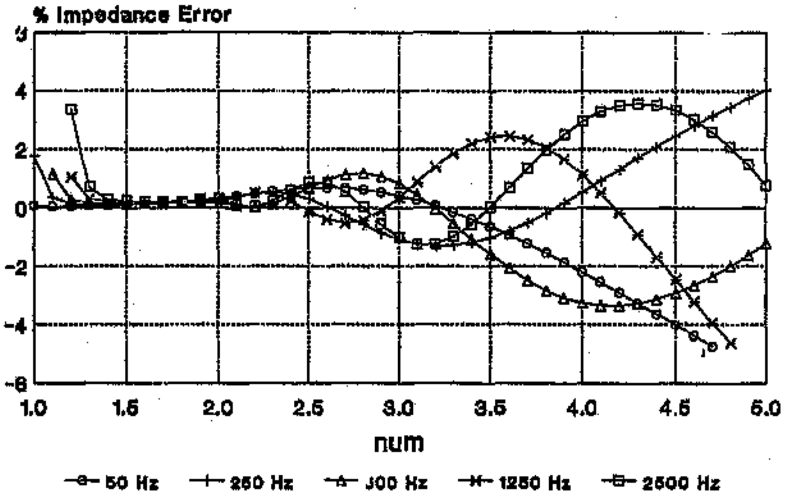

Figure D.37 : Variation Of Percentage Impedance Error With Value Of *num* At Different Frequencies For Ten Sections Of The Improved Pi Circuit

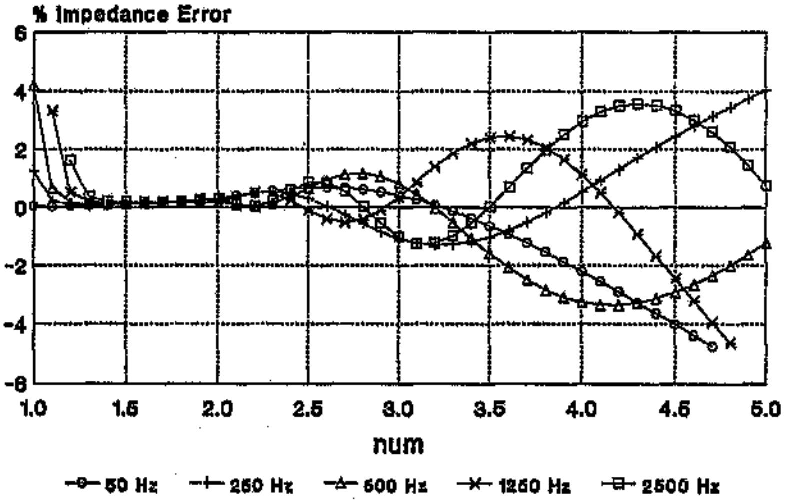

Figure D.38 : Variation Of Percentage Impedance Error With Value Of *num* At Different Frequencies For Eleven Sections Of The Improved Pi Circuit

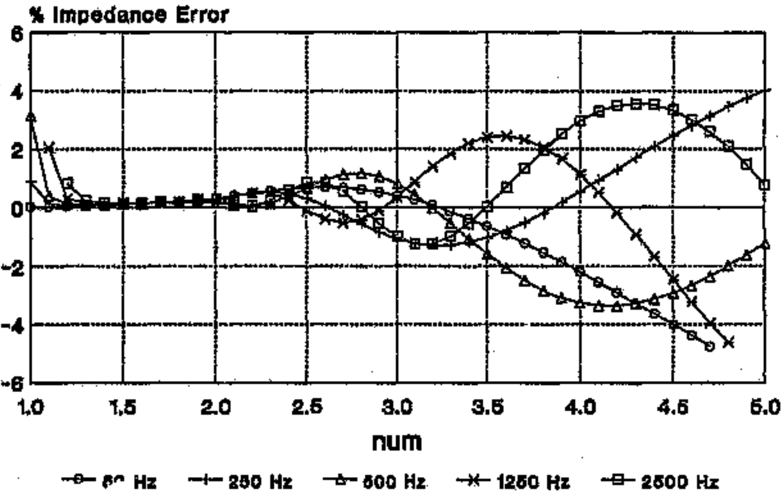

Figure D.39 : Variation Of Percentage Impedance Error With Value Of *num* At Different Frequencies For Twelve Sections Of The Improved Pi Circuit

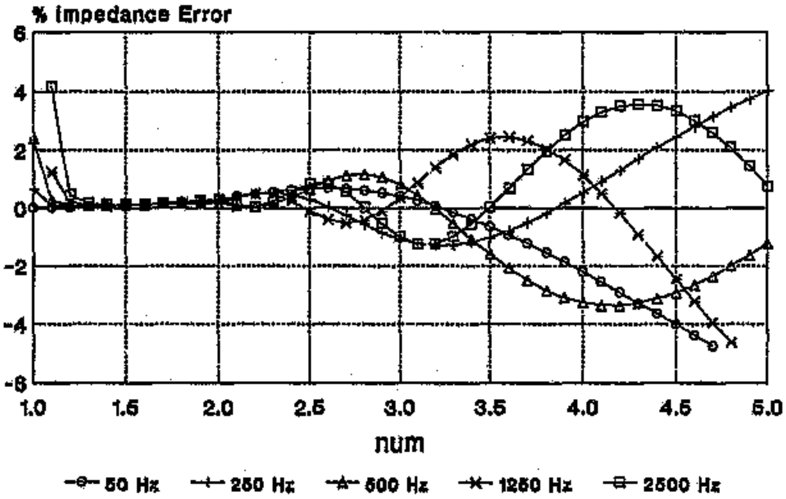

Figure D.40 : Variation Of Percentage Impedance Error With Value Of *num* At Different Frequencies For Thirteen Sections Of The Improved Pi Circuit

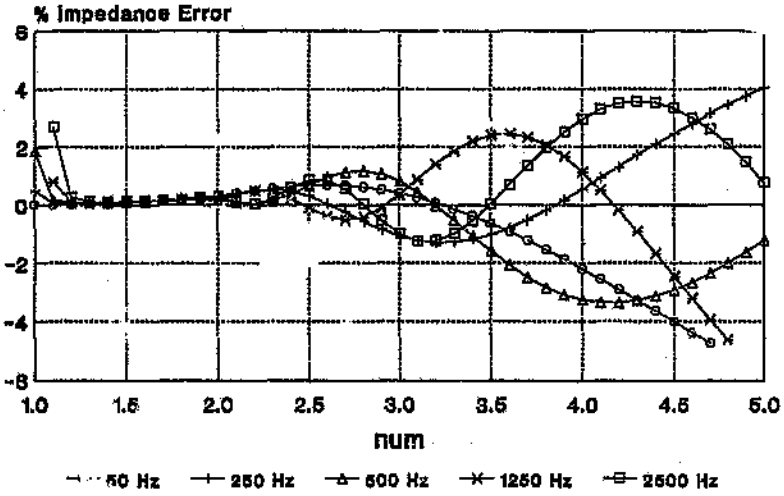

Figure D.41 : Variation Of Percentage Impedance Error With Value Of *num* At Different Frequencies For Fourteen Sections Of The Improved Pi Circuit

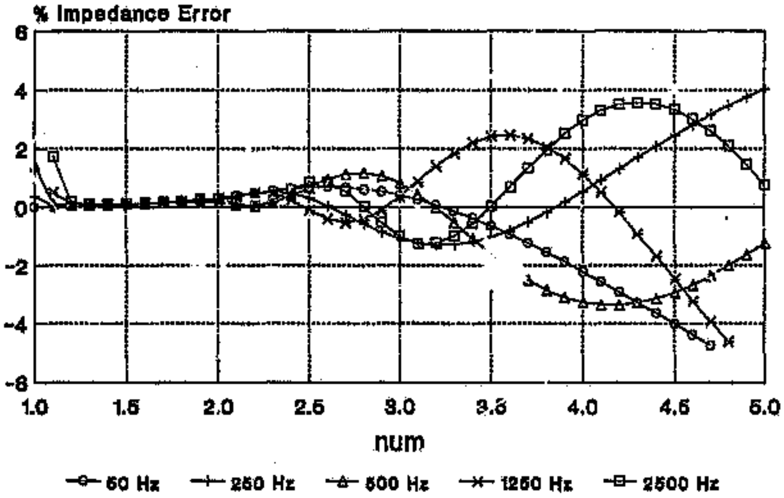

Figure D.42 : Variation Of Percentage Impedance Error With Value Of *num* At Different Frequencies For Fifteen Sections Of The Improved Pi Circuit

APPENDIX E

Predicted Currents

This Appendix gives the stator and rotor current waveforms for the deep bar model, for the traditional model using rotor values corrected for 50 Hz and for the traditional model using DC rotor values respectively. All simulations were run in a rotor fixed reference frame.

All results are given for the 254 kW, 3300 V, 3 phase, 50 Hz, 4 pole squirrel cage induction motor of Section 3.8.1. The graphs are given for the motor initially at rest. The motor is then supplied with full rated sinusoidal voltage and allowed to run up against its own inertia.

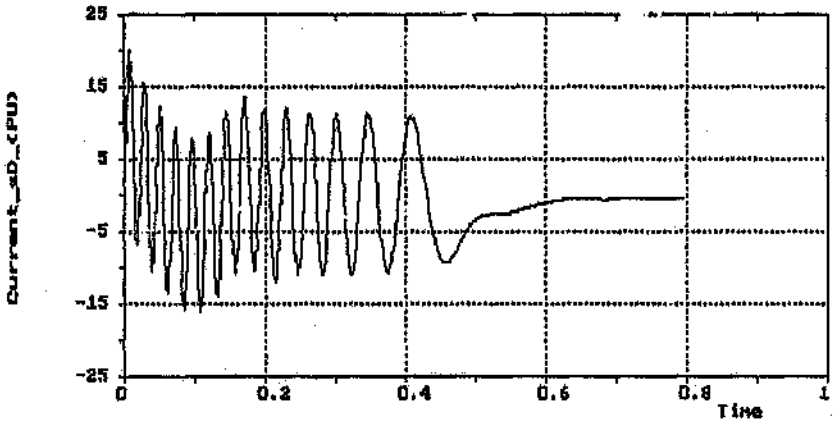

Figure E.1 : Stator d-axis Current - Deep Bar Model Of 254 kW, 3300 V, 4 Pole Induction Motor

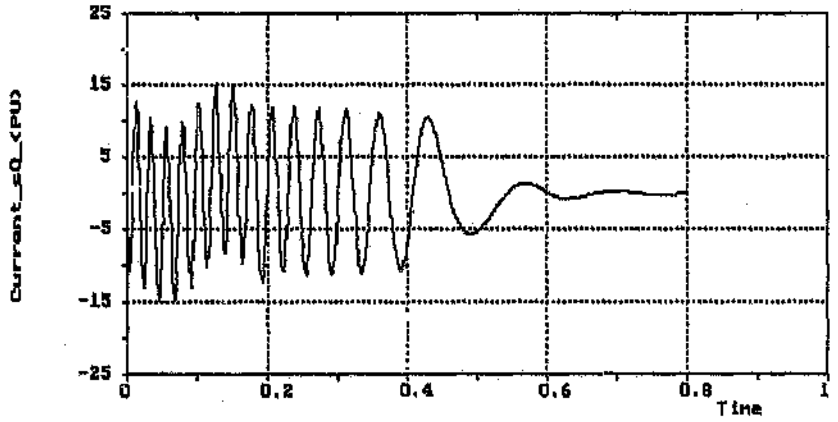

Figure E.2 : Stator q-axis Current - Deep Bar Model Of 254 kW, 3300 V, 4 Pole Induction Motor

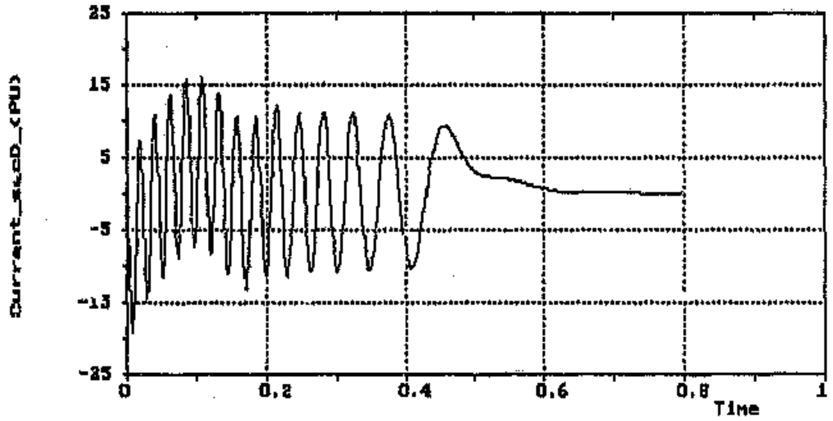

Figure E.3 : Rotor d-axis Current - Deep Bar Model Of 254 kW, 3300 V, 4 Pole Induction Motor

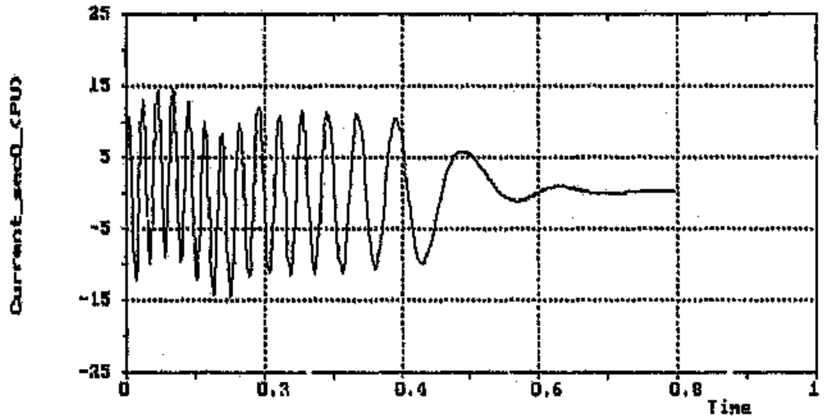

Figure E.4 : Rotor q-axis Current - Deep Bar Model Of 254 kW, 3300 V, 4 Pole Induction Motor

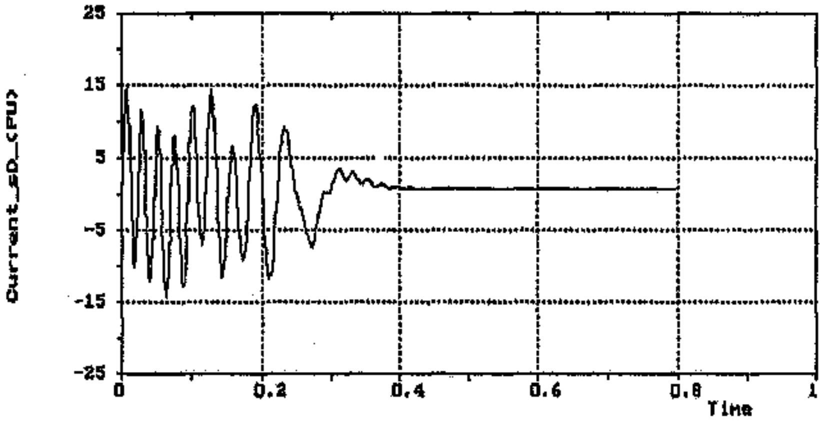

Figure E.5 : Stator d-axis Current - Traditional Model 50 Hz Values Of 254 kW, 3300 V, 4 Pole Induction Motor

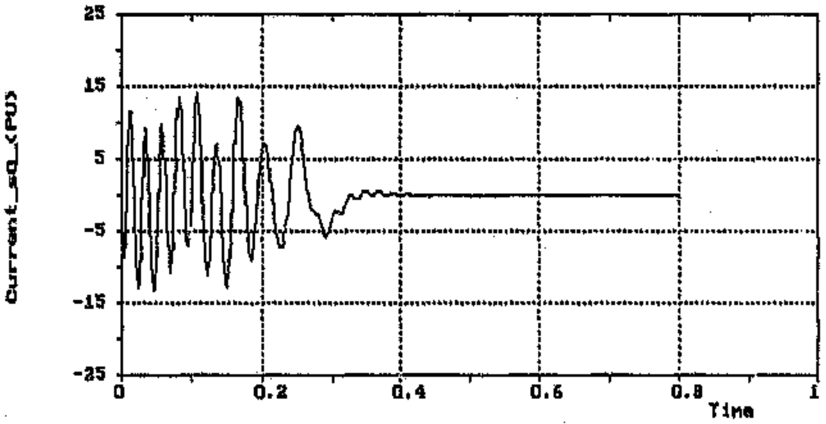

Figure E.6 : Stator q-axis Current - Traditional Model 50 Hz Rotor Values Of 254 kW, 3300 V, 4 Pole Induction Motor

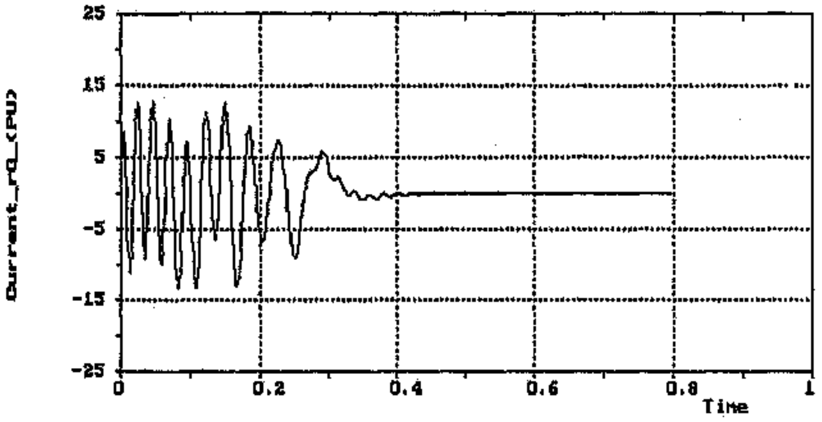

Figure E.7 : Rotor d-axis Current - Traditional Model 50 Hz Rotor Values Of 254 kW, 3300 V, 4 Pole Induction Motor

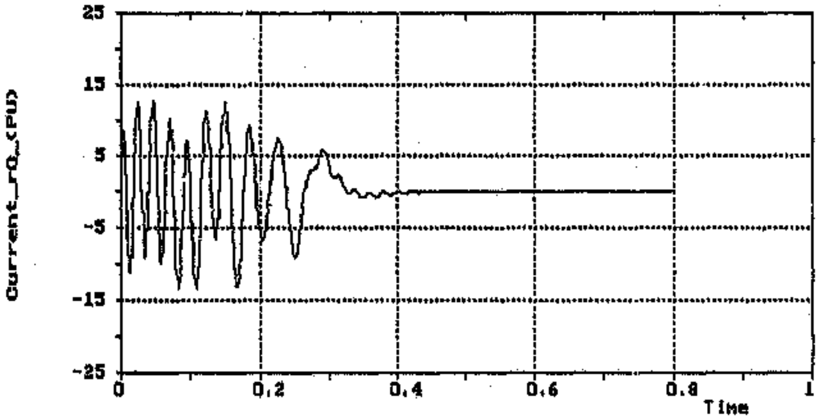

Figure E.8 : Rotor q-axis Current - Traditional Model 50 Hz Rotor Values Of 254 kW, 3300 V, 4 Pole Induction Motor

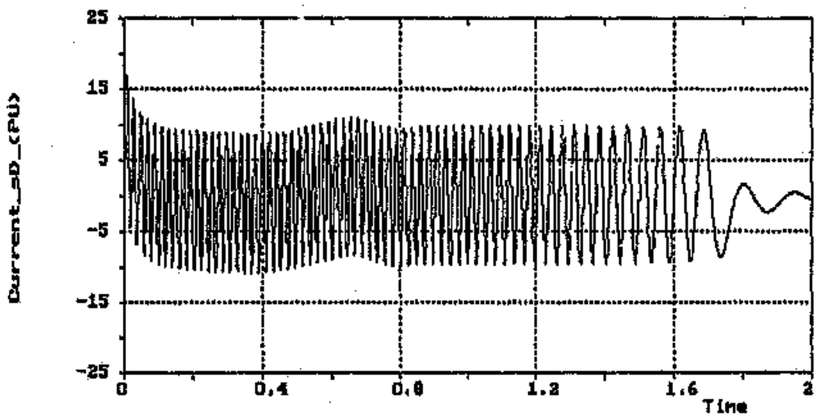

Figure E.9 : Stator d-axis Current - Traditional Model DC Rotor Values Of 254 kW, 3300 V, 4 Pole Induction Motor

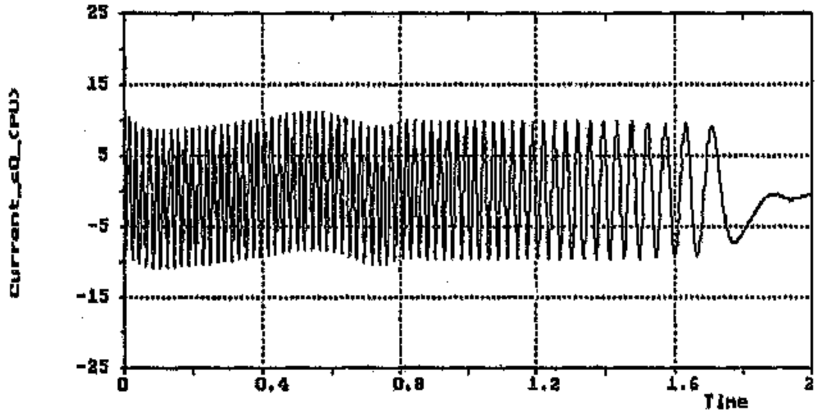

Figure E.10 : Stator q-axis Current - Traditional Model DC Rotor Values Of 254 kW, 3300 V, 4 Pole Induction Motor

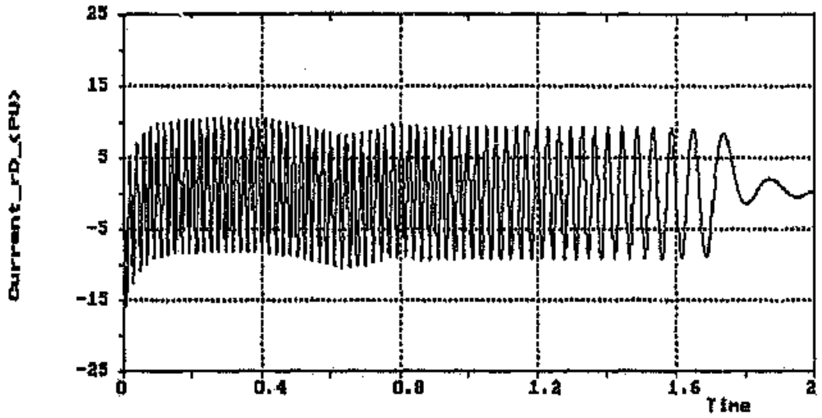

Figure E.11 : Rotor d-axis Current - Traditional Model DC Rotor Values Of 254 kW, 3300 V, 4 Pole Induction Motor

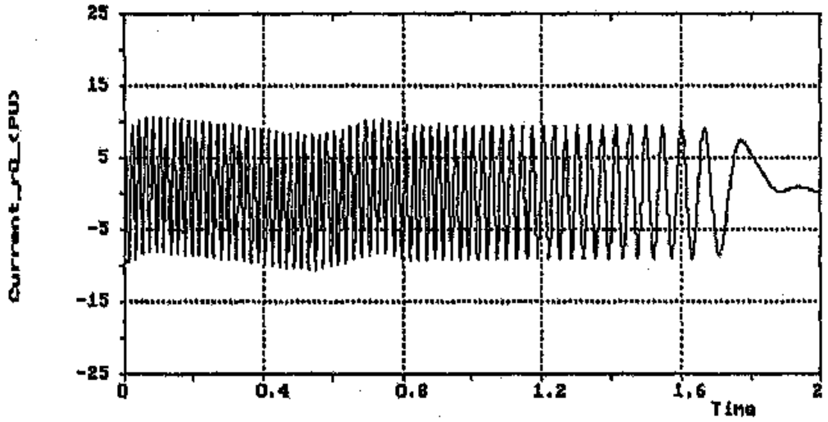

Figure E.12 : Rotor q-axis Current - Traditional Model DC Rotor Values Of 254 kW, 3300 V, 4 Pole Induction Motor

REFERENCES

1. Tesla N., "**A New System Of Alternate Current Motors And Transformers**", AIEE Trans, vol. 5, 1888, pp. 305-327.

2. Bruges W.E., "**Evaluation And Application Of Certain Ladder-Type Networks**", Proc Royal Society Of Edinburgh, vol. 62, num. 2, 1946, pp. 175-186.

3. Babb D.S. and Williams J.E., "**Circuit Analysis Method For Determination Of A-C Impedances Of Machine Conductors**", AIEE Trans, vol. 70, 1951, pp. 661-666.

4. Babb D.S. and Williams J.E., "**Network Analysis Of A-C Machine Conductors**", AIEE Trans, vol. 70, 1951, pp. 2001-2005.

5. Liwschitz-Garik M.M., "**Skin-Effect Bars Of Squirrel Cage Rotors**", AIEE Trans, vol. 73, 1954, 255-258.

6. Liwschitz-Garik M.M., "**Computation Of Skin Effect In Bars Of Squirrel-Cage Rotors**", AIEE Trans, vol. 74, 1955, pp. 768-771.

7. Agarwal P.D. and Alger P.L., "**Saturation Factors For Leakage Reactance Of Induction Motors**", AIEE Trans, vol. 80, 1961, pp. 1037-1042.

8. de Mello F.P. and Walsh G.W., "**Reclosing Transients In Induction Motors With Terminal Capacitors**", AIEE Trans, vol. 80, 1961, pp. 1206-1213.

9. Krause P.C. and Thomas C.H., "**Simulation Of Symmetrical Induction Machinery**", IEEE Trans Power Apparatus and Sytems, vol. 84, num. 11, 1965, pp. 1038-1053.

10. Chalmers B.J. and Sarkar B.R., "**Induction-Motor Losses Due To Nonsinusoidal Supply Waveforms**", IEE Proc, vol. 115, num. 12, 1968, pp. 1777-1782.

11. Klingshirn E.A. and Jordan H.E., **"Polyphase Induction Motor Performance And Losses On Nonsinusoidal Voltage Sources"**, IEEE Trans Power Apparatus and Systems, vol. 87, num. 3, 1968, pp. 624-631.

12. O'Kelly D. and Simmons S., **"Introduction To Generalized Electrical Machine Theory"**, McGraw-Hill Publishing Company, London, 1968.

13. Chalmers B.J. and Dodgson R., **"Saturated Leakage Reactances Of Cage Induction Motors"**, IEE Proc, vol. 116, num. 8, 1969, pp. 1395-1404.

14. Alger P.L., **"Induction Machines - Their Behavior And Uses"**, Gordon and Breach Science Publishers, New York, 1970.

15. de Sarkar A.K. and Berg G.J., **"Digital Simulation Of Three-Phase Induction Motors"**, IEEE Trans Power Apparatus and Systems", vol. 89, no. 6, 1970, pp. 1031-1037.

16. Klingshirn E.A. and Jordan H.E., **"Simulation Of Polyphase Induction Machines With Deep Rotor Bars"**, IEEE Trans Power Apparatus and Systems, vol. 89, num. 6, 1970, pp. 1038-1043.

17. Landy C.F., **"Reswitching Transients Produced In Induction Motors"**, MSc Thesis, University of the Witwatersrand, Johannesburg, 1970.

18. Enright W.H., Hull T.E. and Lindberg B., **"Comparing Numerical Methods For Stiff Systems Of O.D.E.'s"**, Bit, vol. 15, 1975, pp. 10-48.

19. Konrad A., **"The Numerical Solution Of Steady-State Skin Effect Problems - An Integrodifferential Approach"**, IEEE Trans Magnetics, vol. 17, no. 1, 1981, pp. 1148-1152.

20. Konrad A., "**Integrodifferential Finite Element Formulation Of Two-Dimensional Steady-State Skin Effect Problems**", IEEE Trans Magnetics, vol. 18, no. 1, 1982, pp. 284-292.

21. Melkebeek J.A.A., "**Magnetising-Field Saturation And Dynamic Behaviour Of Induction Machines Part 1 : Improved Calculation Method For Induction-Machine Dynamics**", IEE Proc, vol. 130, num. 1, 1983, pp. 1-9.

22. de Buck F.G.G., Gistelinck P. and de Backer D., "**A Simple But Reliable Loss Model For Inverter-Supplied Induction Motors**", IEEE Trans Industry Applications, vol. 20, num. 1, 1984, pp. 190-202.

23. Flores J.C., Buckley G.W. and McPherson G., "**The Effects Of Saturation On The Armature Leakage Reactance Of Large Synchronous Motors**", IEEE Trans Power Apparatus and Systems, vol. 103, no. 3, 1984, pp. 593-600.

24. Gomes A.A.D.F.P., "**The Effects Of Supply Time-Harmonics On The Torque Of Squirrel Cage Induction Motors**", Ph.D. Thesis TK 2785, University of the Witwatersrand, Johannesburg, 1984.

25. He Y.K. and Lipo T.A., "**Computer Simulation Of An Induction Machine With Spatially Dependent Saturation**", IEE Trans Power Apparatus and Systems, vol. 103, num. 4, 1984, pp. 707-714.

26. Lipo T.A. and Consoli A., "**Modeling And Simulation Of Induction Motors With Saturable Leakage Reactances**", IEEE Trans Industry Applications, vol. 20, num. 1, 1984, pp. 180-189.

27. Ramshaw R.S. and Xie G., "**Nonlinear Model Of Nonsalient Synchronous Machines**", Trans Power Apparatus and Systems, vol. 103, num. 7 , 1984, pp. 1809-1815.

28. Kerkman R.J., "**Steady-State And Transient Analyses Of An Induction Machine With Saturation Of The Magnetizing Branch**", Trans Industry Applications, vol. 21, num. 1, 1985, pp. 226-234.

29. Lavers J.D. and Cheung R.W.Y., "**A Software Package For The Steady State And Dynamic Simulation Of Induction Motor Drives**", IEEE Trans Power Systems, vol. 1, no. 2, 1986, pp. 167-173.

30. Mahmoud A.M.A. and Menzies R.W., "**A Complete Time Domain Model Of The Induction Motor For Efficiency Evaluation**", IEEE Trans Energy Conversion, vol. 1, num. 1, 1986, pp. 68-76.

31. Ostovic V., "**Computation Of Saturated Permanent-Magnet AC Motor Performance By Means Of Magnetic Circuits**", Trans Industry Applications, vol. 23, num. 5, 1987, pp. 836-841.

32. Boldea I. and Nasar S.A., "**A General Equivalent Circuit (GEC) Of Electric Machines Including Crosscoupling Saturation And Frequency Effects**", IEEE Trans Energy Conversion, vol. 3, num. 3, 1988, pp. 689-695.

33. Fuchs E.F., Poloujadoff M. and Neal G.W., "**Starting Performance Of Saturable Three-Phase Induction Motors**", IEEE Trans Energy Conversion, vol. 3, num. 3, 1988, pp. 624-635.

34. Ghani S.N., "**Digital Computer Simulation Of Three-Phase Induction Machine Dynamics - A Generalized Approach**", IEEE Trans Industry Applications, vol. 24, no. 1, 1988, pp. 106-114.

35. Ghani S.N., "**On Simulating Dynamic Behaviour Of Three Phase Induction Machines With Squirrel Cage Rotor**", Simulation, vol. 50, no. 5, 1988, pp. 182-193.

36. Keyhani A. and Tsai H., **"IGSPICE Simulation Of Induction Machines With Saturable Inductances"**, IEEE Trans Energy Conversion, vol. 4, no. 1, 1989, pp. 118-125.

37. McCulloch M.D., Landy C.F. and MacLeod I.M., **"Generalised Model Of Converters Containing Linear Elements And Switches Which Is Suitable For Simulation"**, SAIEE Trans, vol. 80, no. 1, 1989, pp. 20-28.

38. Mukherjee S., Adams G.E. and Hoft R., **"FEM Analysis Of Inverter-Induction Motor Rotor Conduction Losses"**, IEEE Trans Energy Conversion, vol. 4, no. 4, 1989, pp. 671-677.

39. Levy W., Landy C.F. and McCulloch M.D., **"Improved Models For The Simulation Of Deep Bar Induction Motors"**, IEEE Trans Energy Conversion, vol. 5, no. 2, 1990, pp. 393-400.

40. McCulloch M.D., Landy C.F., Levy W. and MacLeod I.M., **"CASED : A Simulation Package Designed For Variable Speed Drives"**, Submitted to Simulation.

EXTRA REFERENCES

These references were not specifically referred to in the text but were consulted and are relevant to the subject.

1. Carr L.H.A., "**Induction Motor Leakage**", Metropolitan-Vickers Gazette, 1937, pp. 426-431.
2. Wood W.S., Flynn F. and Shanmugasundaram A., "**Transient Torques In Induction Motors, Due To Switching Of The Supply**", IEE Proc, vol. 112, num. 7, 1965, pp. 1348-1354.
3. Kalsi S.S., Stephen D.D. and Adkins B., "**Calculation Of System-Fault Currents Due To Induction Motors**", IEE Proc, vol. 118, num. 1, 1971, pp. 201-215.
4. Rajan S.D., Jacovides L.J. and Lewis W.A., "**Digital Simulation Of A High Performance AC Drive System - Parts I & II**", IEEE Trans Industry Applications, vol. 10, num. 3, 1974, pp. 391-402.
5. Bowes S.R. and Clements R.R., "**Digital Computer Simulation Of Variable-Speed PWM Inverter-Machine Drives**", IEE Proc, vol. 130, num. 3, 1983, pp. 149-160.
6. Betz R. and Evans R., "**Torque, Speed, And Position Control Of Induction Machines Using The DQ Model**", IEEE Trans Aerospace and Electronic Systems, vol. 21, num. 5, 1985, pp. 698-710.
7. Richards G.G., "**Reduced Order Model For Single And Double Cage Induction Motors During Startup**", IEEE Trans Energy Conversion, vol. 3, num. 2, 1988, pp. 335-341.

Author: Levy Warren.
Name of thesis: Modelling And Simulation Of Induction Motors For Variable Speed Drives, With Special Reference To Deep Bar And Saturation Effects.

PUBLISHER:
University of the Witwatersrand, Johannesburg
©2015